Microfabrication and characterization of a new box-shaped high frequency (7.5 MHz) low aperture 2D phased ultrasound transducer array

by

Ikra Iftekhar Shuvo

B.Sc., Bangladesh University of Textiles (2014)
S.M., University of Manitoba (2018)
S.M., University of Alberta (2021)

Submitted to the Program in Media Arts and Sciences, School of Architecture and Planning, in partial fulfillment of the requirements for the degree of

Master of Science

at the
Massachusetts Institute of Technology (MIT)
September 2023

Authored by:	Ikra Iftekhar Shuvo Program in Media Arts and Sciences Aug/15/2023
Certified by:	Canan Dagdeviren Associate Professor
Accepted by:	Joseph Paradiso Academic Head, Program in Media Arts and Sciences

Microfabrication and characterization of a new box-shaped high frequency (7.5 MHz) low aperture 2D phased ultrasound transducer array

by

Ikra Iftekhar Shuvo

Submitted to the Program in Media Arts and Sciences, School of Architecture and Planning, on Aug/15/2023 in partial fulfillment of the requirements for the degree of

Master of Science

Abstract

Mini electronics in wearables inspired this study. Thus, this work offers a new box-shaped high frequency (7.5 MHz) low aperture 2D phased sparse array ultrasonic transducer developed, built, and characterized. The capacity of matrix or 2D phased arrays to generate ultrasound beams without requiring any form of motion or mechanical steering holds potential value in the biomedical sonographic domain. However, these systems need a large number of piezoelectric elements to sample the active aperture, which is smaller than $\lambda/2$ wavelength between them, necessitating the need for a sizable or large transducer. To the best of knowledge, this is the first endeavor to design and microfabricate a 7.5 MHz transducer array, based on commercial PZT-5H polycrystalline materials, as tiny as 70x70 µm per transducer with a pitch of 102 µm to maintain an inter-element separation below 50% of the lambda. The study employs a square box-shaped structure that houses the transmitters and receivers perpendicular to each other, resulting in a reduced aperture and compact design compared to different commercial designs. This transducer not only provides satisfactory longitudinal k_{33} coefficient (0.45-0.5), acoustic pressure (2.1 kPa), sound pressure level (180 dB), low Q-factor (1.19), thermal stability, and high bandwidth (5.6 MHz, 73.41%), while minimizing cross-talk (<-50 dB), but also reduces the overall transducer area due to its unique sparse array configuration, resulting in a diminutive size (3.3 mm x 3.3 mm).

Thesis advisor:
Canan Dagdeviren
Associate Professor

Microfabrication and characterization of a new box-shaped high frequency (7.5 MHz) low aperture 2D phased ultrasound transducer array

by

Ikra Iftekhar Shuvo

This dissertation/thesis has been reviewed and approved by the following committee members

Canan Dagdeviren, Ph.D.

Associate Professor, MIT Media Laboratory
Massachusetts Institute of Technology

Mitchel Resnick, Ph.D.

Professor, MIT Media Laboratory
Massachusetts Institute of Technology

Jelena Notaros, Ph.D.

Assistant Professor, Department of Electrical Engineering and Computer Science
Massachusetts Institute of Technology

Table of contents

Acknowledgement

The famous scientist Isaac Newton once said, "*If I have seen further, it is by standing upon the shoulders of giants*." Consequently, I would like to start by conveying my gratitude to all the exceptional academics whose previous scholarly works, experiments, and fabrication methodologies helped me complete this project. I express my sincere gratitude to the Media Lab at the Massachusetts Institute of Technology (MIT) and the Center for Nanoscale Systems (CNS) at Harvard University for providing an enriching educational experience encompassing diverse subject matter and practical competencies. I acknowledge the advisory role of Dr. Canan Dagdeviren in fostering a research-oriented mindset and assigning a demanding and consequential project during the pursuit of my Master's degree. Also, I am thankful to Dr. Resnick and Dr. Notaros for their valuable suggestions. I would like to extend my profound gratitude to Dr. Neil Gershenfeld for affording me the privilege of learning about digital fabrication and embedded programming for sensors and actuators. The study material provided by David Mejorado played a crucial role in facilitating my understanding and research on transducer fabrication and their piezoelectric and acoustic characterization. I appreciate the kind support I received from Dr. Lin Zhang, Dr. Hyunsu Park, and David Sadat for their significant contributions in facilitating the acquisition of knowledge on microfabrication techniques and the fundamentals of ultrasound transducers. I want to specially thank Jason-Tresback (Senior Metrology Engineer, CNS, Harvard University), and Timothy-Cavanaugh (Imaging Engineer, CNS, Harvard University) for their valuable assistance and resources to facilitate my research endeavors.

It would be highly unjust if I were to fail to acknowledge that the theory and design for the box-shaped array, including the specific arrangement of transmit and receive elements, was contributed by Colin Marcus. I greatly appreciate the regular accessibility he demonstrated in addressing my scientific inquiries and providing prompt responses, which were non-trivial in enhancing my comprehension of ultrasound physics. I would also like to thank him for helping me execute the acoustic and cross-talk experiments My supportive colleagues, especially Debbie Yu, Ahmad Mujtaba Jebran, Sara Fernandez, Aastha Shah, Jason Hou, Dr. Jin-Hoon Kim, and Dr. Osman Goni Nayeem deserve my sincere gratitude for making my time at Media Lab enjoyable.

List of figures

Contents **Page #**

List of tables

Contents **Page #**

Chapter 1

1. Introduction

1.1. Ultrasound transducer for biomedical applications

The field of ultrasonic imaging has achieved a significant level of development, leading to its widespread recognition and utilization in clinical practice. This fact is apparent due to its significant impact, accounting for approximately 25% of all imaging procedures performed worldwide **(Wells 2006)**. The transducer is considered to be the most crucial component in ultrasonic biomedical imaging systems due to its remarkable effectiveness as a transmitter, significant sensitivity as a receiver, wide dynamic range, and extensive bandwidth. Despite the current maturity of the field of constructing ultrasonic imaging transducers, it is crucial to underscore that this should not be misconstrued as a stagnation in the pace of advancements or novel developments pertaining to techniques and equipment. Contrary to the commonly held belief, the opposite is actually the case.

The efficacy of conventional hand-held ultrasonic (HHUS) transducers with rigid housings (**Figure 1.1a)** is constrained when it comes to accurately detecting muscle activity during mobility of the target muscle, such as in the upper or lower limbs. Also, any ultrasonic transducer instrument that is pressed against the surface of the body has the potential to inhibit the function of the underlying musculature. Additionally, the precision of measurement is often operator dependent and can be substantially affected due to inadequate adherence of the conventional transducer surface to the skin. In particular, it is not feasible for current handheld transducers to acquire imagery across curvilinear body surfaces like cranial region, abdomen or breasts (as depicted in **Figure 1.1b-c)**. In contrast, the flexible and wearable miniaturized transducers possess the ability to affix itself to the specific body region of interest without impeding the mobility of the underlying tissue due to their compact footprint and conformability and, consequently, averting any displacement of the transducer. The advancements in materials science and fabrication techniques have led to the emergence of wearable miniaturized ultrasound devices as a highly promising field within medical applications, especially due to their non-invasive and unobtrusive nature. A

few illustrative cases include fetal heart monitoring **(Hamelmann et al. 2019),** blood pressure waveform monitoring **(Peng et al. 2021; Chonghe Wang et al. 2018),** and muscle activity monitoring for assistive robotics applications **(Xue et al. 2023). Table 1** showcases a selection of recent studies pertaining to the development and utilization of flexible and conformable ultrasound devices within the realm of biomedical applications.

Table 1: Recent work on flexible and conformable ultrasound devices for biomedical applications.

Research work	Array type	Active channels	Freq. (MHz)	Bandwidth	Resolution, penetration depth, field of view (FOV)	Fabrication and application
(Wang et al. 2022)	Linear, phased	80 (2 by 40)	3, 7, 10	68%, 75%, 78%	Axial (0.77mm at 3 MHz, 0.225mm at 7 MHz, 0.193mm at 10 MHz); lateral (1.79mm at 3 MHz with focal depth of 6 cm, 0.38mm at 7 MHz and 3 cm, 0.38mm at 10 MHz and 2 cm)	A bio-adhesive hydrogel-elastomer gel acts as a couplant, allowing a rigid array to adhere to the skin and continuously image carotid artery, lung, and abdomen
(Wang et al. 2021)	Phased	12x12	2	Narrow band	14cm penetration depth with an axial resolution of 2.5mm	Island-bridge configuration using Ecoflex/PMMA for recording cardiac tissue Doppler and blood flow spectrum using color flow image
(Liu et al. 2022)	-	Single	6.7	86.3%	Lateral (0.4mm), depth (36mm), and FOV (20mm x 20mm)	3D photoacoustic imaging using a highly flexible transparent (PVDF) ultrasound device based on sandwich structure with indium tin oxide (ITO)

(Qu et al. 2022)	Ring shaped pMUT	23x26	5	40%	Lateral (1.23mm), axial (0.20 mm) and depth (40mm)	B-mode imaging for muscle disorder diagnosis based on thin-film aluminum nitride pMUT array fabricated by cavity silicon-on-insulator process
(Chen et al. 2022)	--	8x8	2	n/a	< 1mm	Island-bridge configuration to house serpentine interconnection between PZT-8 elements sealed with silicon-based film
(Elloian et al. 2022)	2D linear array	16x16	1.4	41%	Axial (≈ 2 mm) and FOV (12 cm × 12 cm × 7 cm)	PZT pillars directly bonded to a flex cable using ACF tape/film for 3D B-mode imaging of the human humerus
(Wei et al. 2022)	2D sparse spiral array	256	5	32%	Axial (0.74 mm), lateral (0.04 rad), depth (65mm), and opening angle of 81^{o}	3D volumetric imaging using sparse 2-D PZT-on-PCB arrays
(Chen et al. 2022)	Linear array	10	2	8.8%	Depth (130mm)	Laser micromachining technique to create island-bridge structure in polyimide file for multi-mode (A-, B-, and E-scan) positioning imaging over curvilinear surface

The integration of ultra-miniaturized electronic processors and sensors that establish interaction with the human body, encapsulated within compact, organic forms, is imperative for the development of wearable technology, as exemplified by Apple's Air Pods Pro (40.5 mm x 16.5 mm x 18 mm) (excluding the charging case) **(Apple Inc. 2023)** or Google's Pixel Buds Pro (22.33

mm x 22.03 mm x 23.72 mm) (excluding the charging case) **(Google 2023).** Hence, device miniaturization is a crucial factor in the development of wearable or conformable ultrasound devices. These devices have the ability to conform to various surfaces, including both developable (e.g., cylindrical surfaces) and nondevelopable surfaces (e.g., spherical surfaces), thereby, augmenting the user experience. One of the motivations for this research stems from the integration of mini electronics within wearables. Consequently, this study introduces a novel box-shaped low aperture two-dimensional (2D) phased array ultrasound transducer, designed, fabricated, and characterized.

The compact and diminutive size of the transducer array makes it suitable for implementation in a range of wearable applications. One notable advantage of matrix or 2D arrays is their ability to generate three-dimensional images without the need for physical movement of the arrays **(Camacho, Svilainis, and Álvarez-Arenas 2022).** The aforementioned capability arises from their aptitude to manipulate the generated wave field and effectively incorporate transmitted and received signals from any given spatial location. Nevertheless, one practical constraint of these systems is their dependence on a larger number of elements in order to effectively sample the active aperture, which is smaller than half the wavelength between the elements. The current production capacity of matrix arrays and front-end electronics is typically insufficient to meet this demand. The technique of subsampling the aperture, which involves reducing the number of elements, is commonly utilized in order to decrease the complexity of the system while still preserving the lateral resolution. If the half-lambda criterion is not satisfied, it leads to an elevation in the magnitude of sidelobe radiation, consequently imposing a constraint on the dynamic range of the image. To overcome these challenges, the present study developed a phased array, aiming to uphold an inter-element spacing that is below fifty percent of the wavelength. Instead of using a linear arrangement of transmitters (Tx) and receivers (Rx), which would require a large aperture, the study proposed the use of a square box-shaped structure. The current arrangement situates the transmitters (Tx) and receivers (Rx) perpendicular to each other, resulting in a compact design characterized by a diminutive aperture size of 3.3 mm x 3.3 mm, much smaller than a regular commercial transducer S8-3 (bandwidth: 3-8 MHz) that demonstrates a 2 cm aperture as depicted in **Figure 1.1.**

Typically, the frequency range used for diagnostic radiology in clinical ultrasound ranges from 2 to 12 and/or 15 MHz **(J. Li et al. 2022; Lucas et al. 2014)**. Higher ultrasound frequencies are associated with shorter wavelengths, resulting in improved spatial resolution. However, shorter wavelengths are observed to be more susceptible to absorption or attenuation. Consequently, higher frequencies have diminished penetrating capabilities. This explains why high frequencies are used to examine and image superficial body structures and low frequencies for deeper body structures. Therefore, for the purpose of this investigation, a frequency of 7.5 MHz was selected, representing a midpoint within the aforementioned range.

Importantly, transducers with 7.5 MHz operating frequency have been used and exemplified in multiple medical ultrasound or sonographic applications (**Figure 1.2.)**: lung ultrasound for diagnosis of COVID-19 **(Denina et al. 2020)** or pneumonia in children **(Reali et al. 2014)** and interstitial syndrome or pneumothorax (collapsed lung) in adults **(Soldati, Copetti, and Sher 2009; Targhetta et al. 1993);** detecting prostate cancer (PCa) **(Salomon et al. 2008)**; pediatric ultrasound for pancreatic tissue and surrounding structures **(Hohl et al. 2007)**, volume of thyroid gland to differentiate between extrathyroidal and intrinsic lesions **(Ueda 1990)**, and abnormalities in biliary tract and gastrointestinal cystic fibrosis manifestations **(Haber 2007)**; evaluating chronic liver diseases or monitoring large variegated liver (laparoscopic category 300) **(Nagata et al. 2003)**; cranial sonography to detect neonatal meningitis **(Gupta et al. 2017)** and arterial cerebral infarction in term neonates **(Cowan 2005)**; diagnosis of wrist injury, especially scaphoid fractures **(Munk et al. 2000)**; assessing long bone fractures of the upper/lower limbs of the body, e.g., forearm, femoral or humeral diaphyseal fractures **(Hübner et al. 2000)**; traumatic splenic injury and lesions to collect information on splenic parenchyma **(Stengel et al. 2001)**; and characterizing breast tissue and cancerous biomass **(Jaeyoung Son et al. 2014)**.

The integration of multiple two-dimensional transducers of this nature within clothing, wearable or flexible polymer patches also holds the potential to enable tailored measurements that account for the specific characteristics of the tissue under examination, including its location, depth, and shape or morphology. A group of students at the École Polytechnique Fédérale de Lausanne (EPFL) in Switzerland, have previously showcased a similar collaborative effort with a startup named IcosaMed, and created SmartBra, which incorporated a collection of miniaturized

ultrasound transducers capable of producing intricate three dimensional images **(Ueberschlag 2020)**. These images are then analyzed using artificial intelligence-based picture recognition algorithms. The ultimate aim of this innovative clothing system is to detect the presence of breast cancer at its earliest stages. Hence, the potential for adaptability in the context of this current study could facilitate the non-invasive biomedical application of entire anatomical regions, even those that require covering extensive surface areas, such as the neonatal cranial region, breast, lung, abdomen, and long bones in upper/lower limbs, through a singular scanning procedure.

It is imperative to acknowledge that this newly introduced box-shaped design has the capacity to be utilized in the fabrication of transducers, functioning across a broad spectrum of frequencies for ultrasound examination, both high and low, rather than being limited solely to 7.5 MHz, which can be accomplished by adjusting the transducer design parameters: 2.5-3.5 MHz (deep abdomen, obstetric, gynecological), 5 MHz (vascular, breast, pelvic), 7.5 MHz (breast, thyroid), 10 MHz (breast, thyroid, superficial veins, superficial masses, musculoskeletal), and 15 MHz (superficial structures, musculoskeletal) **(Murphy and Nadrljanski 2010)**. As a result, a vast array of potential biological applications may be enabled, including the ability to characterize any individual organ of the body, such as human breast tissue, using a variety of frequencies **(Table 2)**. Also, due to the incorporation of microfabrication techniques and the use of commercially available dice-fill micromachining instruments, the methodology employed in this study is highly adaptable.

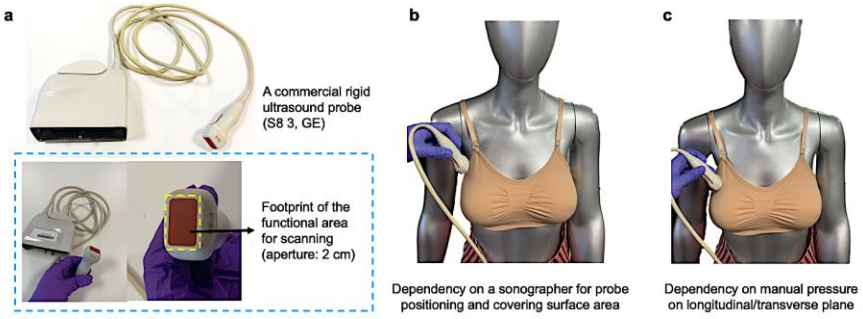

Figure 1.1: Digital photo of a **(a)** rigid hand-held ultrasound (HHUS) transducer imaging probe S8-3 (bandwidth: 3-8 MHz) (General Electronics, USA) with a total aperture of 2 cm and **(b-c)** the resemblance of the operating procedure on a female mannequin.

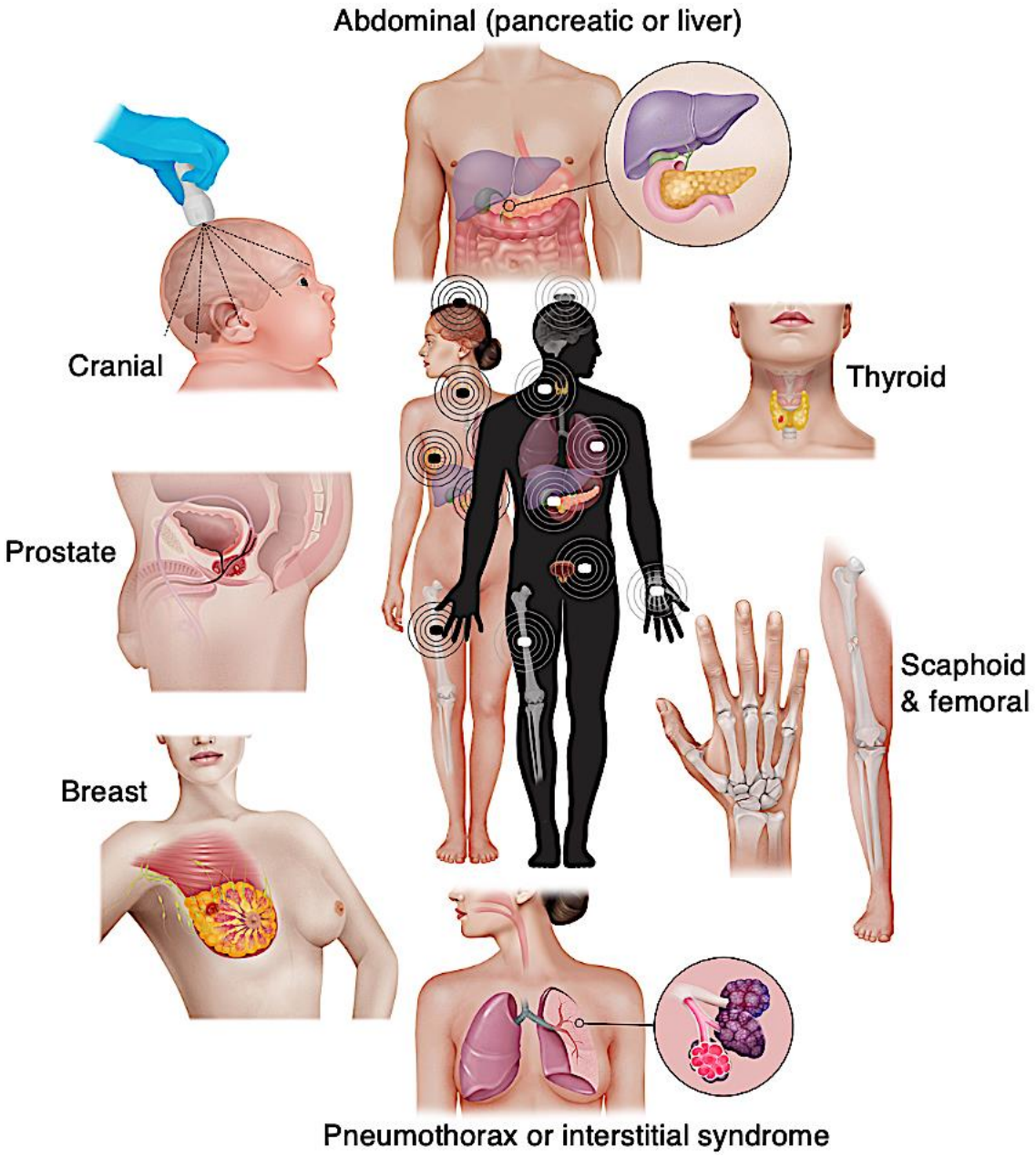

Figure 1.2: A diverse range of sonographic and medical applications, involving the use of 7.5 MHz ultrasound transducer.

Table 2: Different high-frequency ultrasound transducers employed for breast tissue characterization and detecting carcinoma, tumors or similar biomarkers.

Study	Frequency (MHz)	Imaging focus/depth (cm) & Bandwidth	Array type	Aperture size (mm) & no of channels	Pitch (mm)	Scanning time (s) (and patient position)	Form-factor	Compression requirement	Subject freely moving	Wearability	In-vitro tests	In-vivo lesion detection			Type of image
												Cysts (Size range)	Solid mass (Size range)	Calcifications (Size range)	
(Jackson et al. 1986)	4MHz (ceramic) and 7.5MHz (PVDF)	6cm (N.R.)	N.R.	N.R.	N.R.	N.R. (supine position)	Soft (Water bag with indwelling transducer)	Yes (via water-filled plastic bag)	No	No	N.C.	11 (0.5-2.5cm)	28 (0.6-6.5 cm)	8 (0.5-18 mm)	2D B-mode
(Wu et al. 2022)	3MHz	6cm (60%)	Ring	100 (radius) (256)	2.45	N.R. (supine position)	Rigid	No (the breast is immersed in a water tank)	No	No	Breast model &. nylon rope	N.C.	N.C.	N.C.	2D B-mode
(Liu et al. 2008)	9MHz	2cm (N.R.)	2D CMUT	>(30x30) (N.R.)	N.R.	N.R.	Rigid	Yes (by operator)	No	No	Oil-in-gel phantom	N.C.	N.C.	N.C.	2D B-mode
(Jaeyoung et al. 2014)	7.5 MHz	8cm (74%)	Dual linear	200 (1024)	0.19	20s (sitting)	Rigid	Yes	No	No	Raw meat	N.C.	N.C.	N.C.	2D B-mode (3D image N.R.)

(Rouyer et al. 2012)	3MHz	5cm (2.25 MHz)	Half-ring array	100 (radius) (1024)	0.34	8s (prone position)	Rigid	No (the breast is immersed in a water tank)	No	No	Different phantoms, separate 2D breast phantom with cyst-like inclusions and steel wires	N.C.	N.C.	N.C.	2D B-mode
(Hossain, Saharkhiz, and Konofagou 2020)	4MHz	1.1-1.5 cm (N.R.)	Philips L7-4 linear probe (4-7 MHz)	N.R. (128)^	N.R.	N.R.	Rigid	Yes	No	No	Phantoms	4TI breast cancer female mice model for preclinical study and a clinical study on a 54-year-old female patient with invasive ductal carcinoma identifying 4mm tumor			2D harmonic motion imaging (HMI)

N.R. = not reported; N.C. = not conducted; U.R. =Under research

^ **(Gouwy 2018)**

1.2. Objective of the thesis work

This thesis work makes the following contributions: (i) micro-machining a high frequency (7.5 MHz) low aperture 2D phased ultrasound transducer array and (ii) micro-fabricating electrical circuit on the individual piezoelectric elements/pixels of the 2D array to connect with the electrical port, and ensuring the developed transducer array will be guaranteed to maintain its piezoelectric property throughout the micromachining and microfabrication processes without going through a depolarization phase, and display adequate piezoelectric and ultrasonic performance.

1.3. Outline of the thesis

This thesis covers the background of piezoelectric ultrasound transducer, the essential factors for building a transducer, various architectures of transducer arrays, as well as the fabrication and performance evaluation of biomedical transducers. The framework of the thesis is as follows:

In Chapter 2, the background of the piezoelectric ultrasonic transducer is described. An overview of the propagation of waves by a transducer, an explanation of critical piezoelectric material properties for selecting ultrasonic transducers, and the fundamental building blocks of an ultrasound transducer are presented. Also, the transducer architectures based on various vibration modes and array geometries are described. Finally, different modeling techniques to simulate transducer performance are presented.

Chapter 3 illustrates how to make and test a 2D high-frequency phased array transducer. For the imaging application, a 2D sparse array of 128 piezoelectric pixels with a resonance frequency of 7.5 MHz and a pitch of 102 μm was built. Out of the 128 pixels, 64 were split between the two transmitter (T_X-1 and T_X-2) arrays, and the other 64 were used for the two receiver (R_X-1 and R_X-2) arrays. Further, the chapter covers the necessary criteria for matching and backing layer designs. In addition, the techniques of micromachining and microfabrication are discussed. 1D KLM (Krimholtz, Leedom, and Matthaei) and FEA (finite element analysis) models were implemented to simulate the electrical and acoustic characteristics of the constructed transducer.

Chapter 4 illustrates the functionality of the 2D sparse array. The chapter begins by describing the surface morphology and topography of the array. The impedance-phase angle spectrum, coupling coefficient (aka k_{33}-factor), resultant bandwidth, acoustic pressure, and Q-factor of the transducer array are listed next. Finally, the chapter ends with cross-talk and thermal stability analysis.

The results of this dissertation are summed up in Chapter 5. Future research directions are also discussed.

Chapter 2

2. Theoretical background

In this chapter, the theoretical background of piezoelectric ultrasound transducer will be discussed. Also, the critical material parameters for piezoelectric material, the significance and selection of resonance geometries, different types of transducer architectures, requirements for designing acoustic matching and backing layers, and the techniques of modelling or simulating transducer performance will be briefly explained.

2.1. Piezoelectricity

"Piezo" is a Greek term that means "to press". Hence, the term piezoelectricity simply refers to the propagated macroscopic polarization and, thereby, the electricity from mechanical stresses. In 1880, Curie brother discovered such piezoelectricity phenomenon (i.e., generated electric charge from applied mechanical stress) while investigating different materials such as quartz, zincblende, and topaz **(Li 2021).** Interestingly, the converse-piezoelectric effect (i.e., generated strain as a function of applied electric field) was predicted in 1881 by Lippmann, i.e., the generation of mechanical deformity from the applied voltage on a piezoelectric material. Piezoelectric materials are employed in different man-made devices, including hydrophones, sonars, accelerometers, proximity sensors, and haptic actuators for robotics. Recent additions to the piezo-product portfolio include conformable ultrasound devices for soft tissue imaging, piezoelectric micromachined ultrasonic transducers (PMUT) for neurostimulation, piezoelectric oxide semiconductor field effect transistors (POSFET), and so on.

2.1.1. The piezoelectric constitutive equations for sensor and actuator

For piezoelectric materials, two equations are used to describe the basic interactions between their electrical and mechanical properties and the conditions they are in **(Li 2017)**. These two equations

are called the piezoelectric constitutive equations, and they represent strain and electric displacement. In their general forms, they are called the actuator and sensor equations **(Shekhani 2016) (Eqn. 1). Fig. 2.1** illustrates the piezoelectric and converse piezoelectric effects for sensing and actuation **(Rödel and Li 2018).**

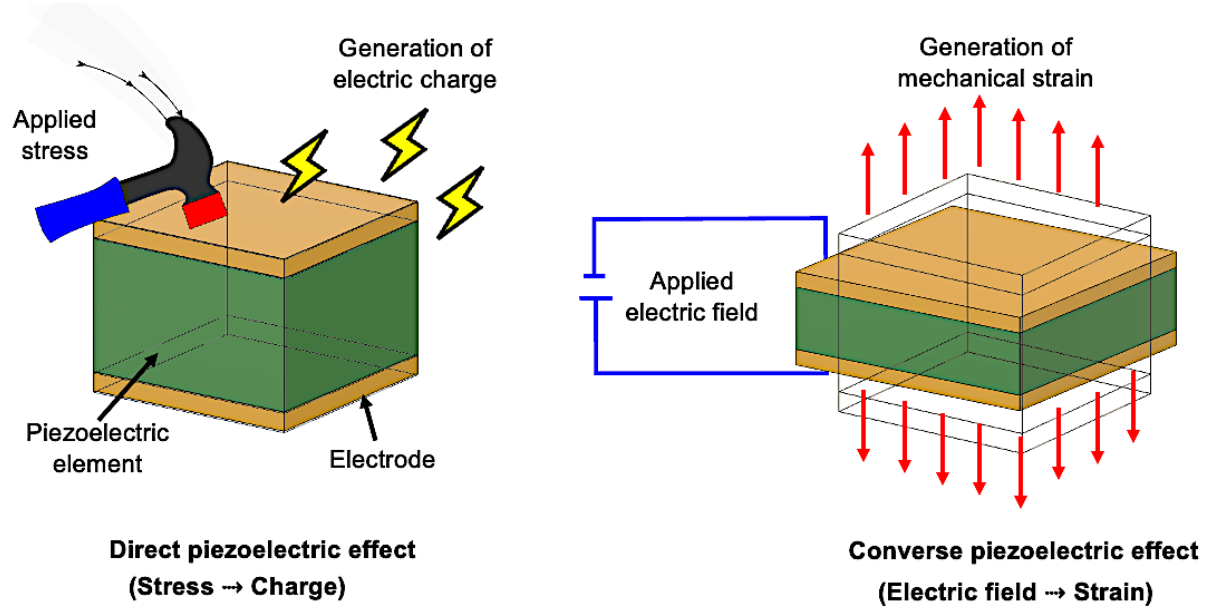

Fig. 2.1: Direct and converse-piezoelectric phenomenon for sensors and actuators**.**

$$\begin{bmatrix}\text{Converse}\\ \text{Direct}\end{bmatrix} = \begin{bmatrix}S\\ D\end{bmatrix} = \begin{bmatrix}s^E & d\\ d & \varepsilon\end{bmatrix}\begin{bmatrix}T\\ E\end{bmatrix} \quad (\textbf{Eqn. 1})$$

or

[Actuator equation]:

$$\partial u/\partial x = S = s^E T + dE$$

[Sensor equation]:

$$D = dT + \varepsilon E$$

Here,

D = dielectric (or charge density) displacement

S = ∂u/∂x = induced strain

E = electrical field E

s^E = elastic compliance under constant E

T = stress

ε = dielectric permittivity under a constant T

d = piezoelectric strain constant

2.2. Wave equation, ultrasound propagation and interaction with soft tissue

The most common method used in modern medical ultrasound exams is the pulse-echo method to show a brightness-mode (B-mode) image. This is accomplished by sending small pulses of ultrasound waves into the body through a piezoelectric transducer **(Figure 2.2a).**

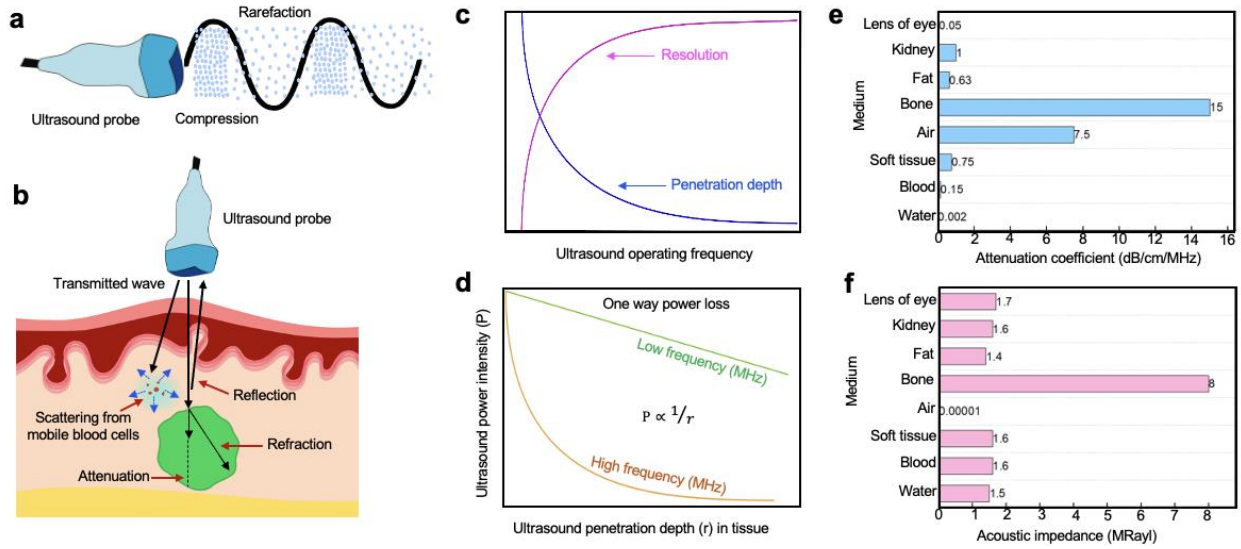

Figure 2.2: Ultrasound physics and its applications. **(a)** Schematic representation of ultrasound pulse generation by piezoelectric transducer. **(b)** Ultrasound propagation and its interaction with tissue. **(c)** A summary of ultrasound frequency and associated penetration depth and resolution. **(d)** 1/r penetration and resultant decreasing planewave ultrasound intensity in soft tissue **(based on data from (Stauffer and Paulides 2014)). (e-f)** A comparison between acoustic attenuation coefficient ($dB.cm^{-1}.MHz^{-1}$) and acoustic impedance of different medium and tissues **(based on data from (Shankar, Pagel, and Warner 2011)).**

When the transducer is electrically excited, the piezoelectric component vibrates and creates ultrasound, i.e., a mechanical pressure wave (via the direct piezoelectric effect), with alternating compressions and rarefactions at a frequency higher than the human hearing range (20 Hz- 20 kHz). Hence, the wave equation is able to be used to describe the propagation of ultrasonic waves since ultrasound is an acoustic wave with accompanying space- (x, y, z) and time-dependent (t) pressure fluctuations. The equation that describes the relationship between spatial and temporal changes of the sound wave pressure is called the wave equation.

There are four equations (i.e., equations of continuity, motion, state, and force) that underlie the sound propagation, which are used to describe the acoustical wave equation in 3D space with the following differential equation (**Eqn. 2)**, where P, c, K, ρ_o, and ∇^2 (= $\nabla.\nabla$ or sometimes $\nabla^2 = \Delta$, where, ∇ is called the del operator) are sound pressure, velocity of sound, bulk modulus of the fluid, ambient density of the fluid, and Laplace operator of the fluid medium **(Kuttruff 2007; Urick 1979):**

$$\frac{\partial^2 \mathrm{P}}{\partial \mathrm{t}^2} = \frac{\mathrm{K}}{\rho_0}\left(\frac{\partial^2 \mathrm{P}}{\partial \mathrm{x}^2} + \frac{\partial^2 \mathrm{P}}{\partial \mathrm{y}^2} + \frac{\partial^2 \mathrm{P}}{\partial \mathrm{z}^2}\right) \textbf{(Eqn. 2)}$$

$$\Rightarrow \frac{\partial^2 \mathrm{P}}{\partial \mathrm{t}^2} = \mathrm{c}^2\left(\frac{\partial^2 \mathrm{P}}{\partial \mathrm{x}^2} + \frac{\partial^2 \mathrm{P}}{\partial \mathrm{y}^2} + \frac{\partial^2 \mathrm{P}}{\partial \mathrm{z}^2}\right) \left(\text{where}, \mathrm{c}^2 = \frac{\mathrm{K}}{\rho_0}\right)$$

$$\Rightarrow \frac{\partial^2 \mathrm{P}}{\partial \mathrm{t}^2}.\frac{1}{\mathrm{c}^2} = \nabla^2 P \left(\text{where}, \nabla^2 = \Delta = \frac{\partial^2}{\partial \mathrm{x}^2} + \frac{\partial^2}{\partial \mathrm{y}^2} + \frac{\partial^2}{\partial \mathrm{z}^2}\right)$$

In 1D space, the wave equation (**Eqn. 3)** is as follows:

$$\frac{\partial^2 \mathrm{P}}{\partial \mathrm{t}^2} = \mathrm{c}^2 \frac{\partial^2 \mathrm{P}}{\partial \mathrm{x}^2} \textbf{(Eqn. 3)}$$

$$\Rightarrow \frac{\partial^2 \mathrm{P}}{\partial \mathrm{t}^2} - \mathrm{c}^2 \frac{\partial^2 \mathrm{P}}{\partial \mathrm{x}^2} = 0$$

As the wave penetrates through the human tissues along the line of transmission, it is reflected back to the transducer in the form of echoes owing to the varying acoustic impedances of the human tissues. In order to form an ultrasound image, the echo signals that are returned from a large number of successive coplanar pulses are received by the piezoelectric scanner to be analyzed and merged. The scanner measures the distance between the transducer and the tissue boundary by using the speed of sound and the time delay of each echo **(Gururaja 1992)**. This data is then used to construct two-dimensional images of tissues and organs. In actuality, the ultrasonic pulse is just a few milliseconds long (with a sub-mm wavelength for high-frequency transducers like >7 MHz). Nonetheless, because it travels in a linear fashion, it is sometimes referred to as an ultrasound beam. The resolution of an ultrasound image is frequency and imaging depth dependent, i.e., higher the frequency, the higher the resolution but the lower the penetration depth **(Figure 2.2c-d)**. Imaging resolution is often defined by its axial and lateral characteristics. Axial resolution is the capacity to differentiate between two points along the propagation path direction of an ultrasonic beam, whereas the lateral (Azimuthal) resolution is the capacity to distinguish between two points perpendicular to the beam.

The acoustic impedance of a tissue determines the ultrasound transmission. The ultrasound waves interact with the organs and tissues through reflection, scattering, refraction, and attenuation **(Otto 2019) (Figure 2.2b)**. Reflection is the return (i.e., echo) of an ultrasonic signal from a smooth tissue border to the transducer due to variations in the acoustic impedance **(Figure 2.2f)** of the tissue. This reflection is the basis of ultrasound 2D and 3D images. When the ultrasonic beam is perpendicular to the contact surface of tissue, reflection is at its maximum. Scattering is the multidirectional emission or radiation of ultrasound from a tiny structure (e.g., blood cells). Doppler ultrasonography is based on this frequency shift phenomenon of scattered signals from moving blood cells. The strength of a scattered signal could be 100-1000 times weaker than that of reflected signals. The magnitude of scattering depends on particle size (red blood cells), number of particles (hematocrit), frequency of transducer, and compressibility of blood cells and plasma. On the other hand, refraction of ultrasound waves is caused by their deviation from a straight path as a result of variations in acoustic impedances. Consequently, double-image artifacts are caused by refraction. Attenuation is the ultrasound signal intensity loss caused by tissue absorption

(Figure 2.2e). Attenuation depends on frequency. High levels of attenuation (less penetration) take place at higher frequencies. According to the equation (**Eqn. 4)**, the attenuation coefficient (α) for each tissue is equal to the drop in ultrasonic intensity (in dB) from point one (I_1) point two (I_2) that is separated by a distance (L). Compared to soft tissue, the air has a relatively high attenuation coefficient. As a result, there would be a significant attenuation of the ultrasound signal if there was any air gap between the transducer and tissue. To preclude this, a water-soluble ultrasonic gel is employed to ensure airless contact with the skin tissue.

$$I_2 = I_1 . e^{-2.\alpha.L} \quad (\mathbf{Eqn.4})$$

The major commercial applications of piezoelectric ultrasound in biomedical industries lie in imaging and Doppler. In addition, ultrasound could also be used for neural activity monitoring, retinal stimulation, drug delivery, heart rate monitoring, and therapeutics like joint mobility, fracture healing, or bone rehabilitation. Nowadays, ultrasonic transducers have shown promising results for energy harvesting to wirelessly power implants **(Turner et al. 2021)**. **Figure 2.3** illustrates a visual summary of different applications of ultrasound transducers in the biomedical industry.

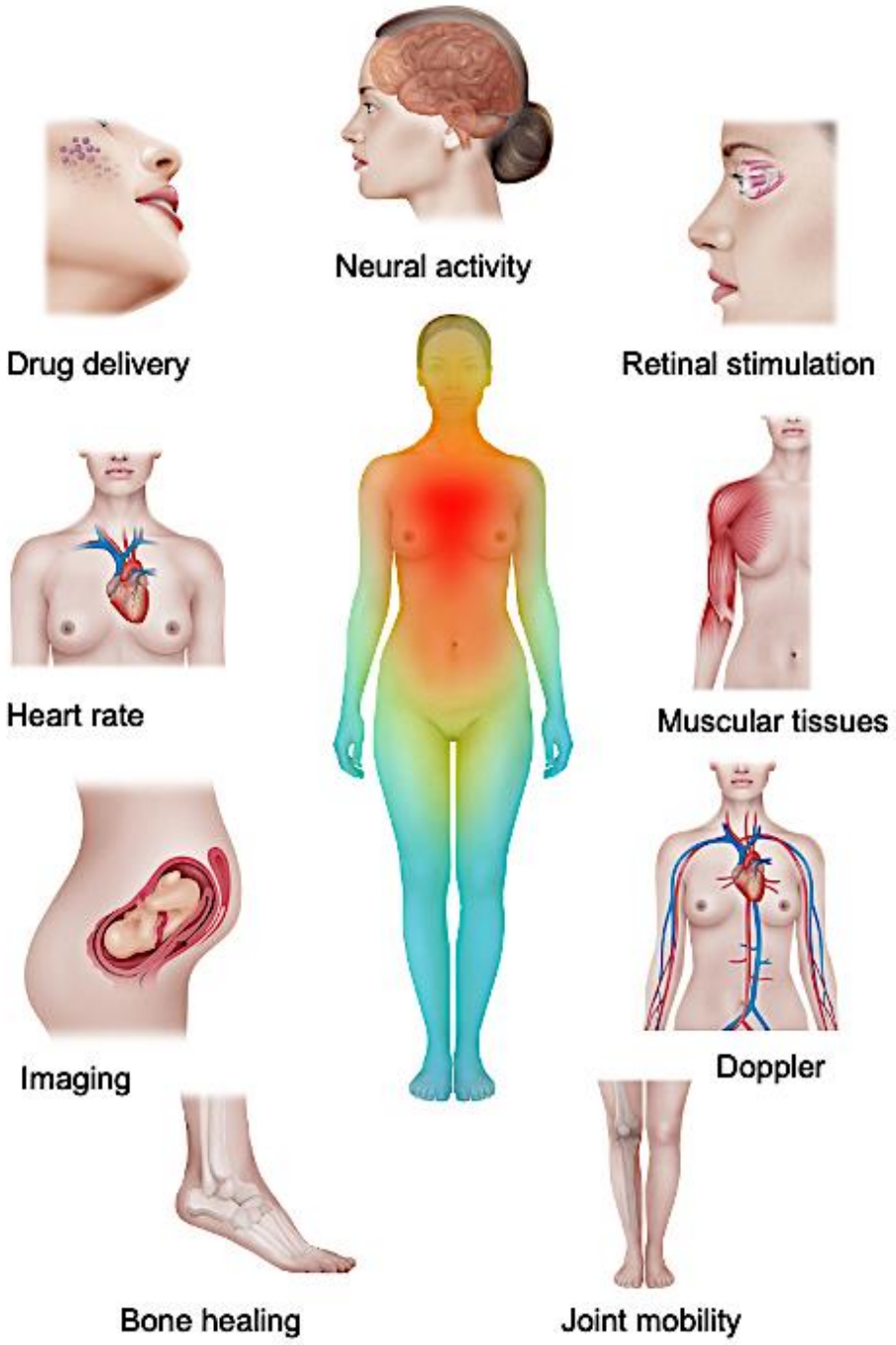

Figure 2.3: A visual summary demonstrating diverse applications of ultrasound transducer for biomedical and healthcare applications.

2.3. Critical material parameters of piezoelectric component in ultrasound transducers

The piezoelectric material used in medical transducers must satisfy a variety of requirements **(Smith and Auld 1991)**. The relevant properties are: (i) high electromechanical coupling coefficient or factor (k), (ii) low acoustic impedance ($Z_{acoustic}$) closer to skin, (iii) large dielectric constant (ϵ) or relative free/clamped permittivity ($\epsilon^T = \varepsilon^T/\varepsilon_0$ or $\epsilon^S = \varepsilon^S/\varepsilon_0$, where, ε^T= free dielectric permittivity, ε^S = clamped permittivity, ε_0, = vacuum permittivity = 8.854×10^{-12} F/m). The influence of losses in piezoelectric materials is also critical for modelling sensitive transduces. Specifically, two loss parameters are considered non-trivial**:** (i) low dielectric (or electrical) loss (tanδ) and (ii) low mechanical loss (Q_{loss}). Hence, these five piezoelectric parameters must be taken into consideration for selecting piezoelectric materials to fabricate medical transducers. A brief summary on each of these five parameters are illustrated below:

2.3.1. Electromechanical coupling factor or coefficient (k)

First, a piezoelectric material with a high electromechanical coupling coefficient ($k \rightarrow 1$) is generally selected to construct a sensitive transducer for ideal transducer applications **(Smith and Auld 1991)**. Because, a high coupling constant (k) ensures increased sensitivity and bandwidth (%) **(Ritter et al. 1999)**. The coefficient, k, is defined as the efficiency of piezoelectric material to convert one form of energy into another (**Eqn. 5) (J.-F. Li 2021):**

$$k = \sqrt{\frac{\text{Mechanical energy stored}}{\text{Electrical energy applied}}} = \sqrt{\frac{\text{Electrical energy stored}}{\text{Mechanical energy applied}}} \quad (\mathbf{Eqn.\,5})$$

Hence, a higher k value indicates higher sensitivity or conversion efficiency of the piezoelectric material **(Ou-Yang et al. 2015)**. In ultrasound transducer, a high k value for any piezoelectric component corresponds to a greater overall round-trip (i.e., pulse-echo) efficiency of ultrasound wave in the loading medium and superior insertion loss (IL, dB) (i.e., ratio of returned echo and transmitted signal voltage), which is often used to characterize the sensitivity of a transducer (**Eqn.**

6). A low insertion loss refers to high sensitivity for a transducer **(Chen et al. 2019; Ramadas, O'Leary, and Gachagan 2009; Wang et al. 2020).** Besides the transducer sensitivity, such IL values could be also used in characterizing tissue properties or detect cervical ripening in pregnant test subjects **(McFarlin et al. 2005)**.

$$IL = 20 \log {}^{V_{pp\ (output)}}\Big/_{V_{pp\ (transmit)}} \quad (\mathbf{Eqn.\ 6})$$

2.3.1.1. Coupling constants and resonance geometries

Since piezoelectrics are anisotropic, their properties vary along different angle. Hence, depending on their geometry and direction of poling vector **(Figure 2.3)** the k values of a piezoelectric material also change. Thus, different mathematical formulas are used to calculate their values. Among the coupling factors, k_{33} and k_p are the most used ones. Also, the formula for k_{33} and k_t are same. The formulas for the coupling factors for different geometries are given below **(Eqns. 7-11),** where d, h, ε, s, and c components depict the piezoelectric strain (m/V or C/N), and piezoelectric stiffness (V/m or N/C), permittivity (F/m), elastic compliance (m^2/N), and elastic stiffness (N/m^2) constants, respectively. The σ, f_r, and f_a represent Poisson ratio (i.e., ratio of lateral strain and linear strain), resonance frequency (Ω), and anti-resonance frequency (Ω). The superscripts T, S, E, and D refer to constant stress, constant strain, constant electric field, and constant electric displacement. More details on the operating modes are discussed in the following section.

$$k_p = \sqrt{\frac{2d_{31}^2}{\varepsilon_{33}^T\,(s_{11}^E + s_{12}^E)}} \quad (\mathbf{Eqn.\ 7})$$

$$k_{33} = \sqrt{\frac{\pi}{2}.\frac{f_r}{f_a}.\tan\left(\frac{\pi}{2}.\frac{f_a - f_r}{f_a}\right)} \quad (\mathbf{Eqn.\ 8})$$

$$k_{15} = \sqrt{\frac{d_{15}^2}{\varepsilon_{11}^T.s_{55}^E}} \quad (\mathbf{Eqn.\ 9})$$

$$k_{31} = \sqrt{\left(\frac{1-\sigma^{E}}{2}\right).k_{p}^{2}} \quad (\mathbf{Eqn.10})$$

$$k_{t}(\text{similar to } k_{33}) = \sqrt{\frac{\pi}{2}.\frac{f_{r}}{f_{a}}.\tan\left(\frac{\pi}{2}.\frac{f_{a}-f_{r}}{f_{a}}\right) = \left(h_{33}^{2}.\varepsilon_{33}^{S}\right)/c_{33}^{D}} \quad (\mathbf{Eqn.11})$$

For a complete device with the piezoelectric material clamped between matching and backing layer, the effective electromechanical coupling coefficient (k_{eff}) are calculated with the following formula **(Eqn. 12) (Hu et al. 2018):**

$$k_{eff} = \sqrt{\left(\frac{f_{a}^{2}-f_{r}^{2}}{f_{a}^{2}}\right)} \quad (\mathbf{Eqn.12})$$

2.3.2. Acoustic impedance ($Z_{acoustic}$)

Second, there must be optimal acoustic coupling ($Z_{acoustic} \rightarrow 1.5$ MRayls) between the piezoelectric material (e.g., 30 MRayls for PZT) and the target tissue (e.g., usually 1.5 MRayls for skin) such that the acoustic waves in the transducer and tissue couple efficiently during transmission and reception. $Z_{acoustic}$ of a material is the product of its density (ρ) and speed of sound (c) in that material **(Eqn. 13)**:

$$Z_{acoustic} = \rho.c \quad (\mathbf{Eqn.13})$$

2.3.3. Dielectric constant (ϵ) or relative free ($\varepsilon^{s}/\varepsilon_{0}$) /clamped ($\varepsilon^{s}/\varepsilon_{0}$) permittivity

Third, the electric characteristics ($\varepsilon^{S}/\varepsilon_{o} \geq 100$), of the piezoelectric material must be compatible with the electronic or associated circuitries that drives and receives the signal. A high relative permittivity allows for effective matching of the electrical impedance ($Z_{electrical}$) of tiny piezoelectric components to the image electronics **(Ritter et al. 1999)**. For example, the combination of high coupling constant and large clamped dielectric permittivity (830-1470) are popular choice for ultrasound imaging transducers **(Szabo and Lewin 2007).** A comparative study

among five different piezoelectric materials is provided in **Figure 2.4**. Also, materials with high free relative permittivity ($\varepsilon^T/\varepsilon_o$ > 6000) provides electrical impedance that could match the electrical impedance ($Z_{electrical} \approx 50\ \Omega$) of imaging system, Verasonics Vantage, for instance **(Ritter et al. 1999)**. However, transformers could theoretically be used for small elements that displays several hundreds of ohms. Alternatively, clamped permittivity (ε^S) could also be used for needle transducers or specific transducer designs like that are clamped between matching and backing layers to match between piezoelectric materials and electrical terminations as a high ε^S or clamped capacitance (C^S) would lower the $Z_{electrical}$ as shown in **Eqns. 14-15,** where, t, A, and f are material thickness, area, and angular frequency, respectively **(Cannata et al. 2003; Zhang et al. 2018)**. Hence, for tiny piezoelectric surface area that would result in high $Z_{electrical}$, developing novel piezoelectric materials with large ε^S is non-trivial. Otherwise, the electronic system will need to add matching circuitries with pre-amplifiers to the tiny piezoelectric elements.

$$Z_{electrical} = \frac{t}{\omega A \varepsilon^S} = \frac{t}{2\pi f A \varepsilon^S} \quad (\mathbf{Eqn.\ 14})$$

$$Z_{electrical} \propto \frac{t}{C^S} = \frac{t}{\varepsilon^S A} \quad (\mathbf{Eqn.\ 15})$$

2.3.4. Dielectric loss (tanδ)

Fourth, the dielectric loss of the piezoelectric material should be low for optimum energy conversion. Electroded piezoelectric dielectrics are often considered as acoustic resonator or singing capacitors as they not only resonate in fundamental resonance frequency (f_0) but also resonate in odd harmonics ($3f_0$, $5f_0$, etc.) **(Szabo and Lewin 2007)**. As they behave as capacitors, facilitating the mobility of charges (Q, C) under an external electric field (E), there capacitance (C, F) could be calculated from the physical dimension of electrode (length, l; width, w; area, A) and thickness (d) of the dielectric based on the equation below **(Eqns. 16-17) (Morel et al. 2018)**:

$$\begin{cases} \oiint E.\,dS = E.\,(l.\,w) = E.\,A = {}^{Q}\!/_{\varepsilon_0 \varepsilon^T} \quad (\mathbf{Eqn.\,16}) \\ C = {}^{Q}\!/_{\left[\int_0^d E.\,dz\right]} = {}^{\varepsilon_0 \varepsilon^T A}\!/_{d} \quad (\mathbf{Eqn.\,17}) \end{cases}$$

As the dielectric is not completely perfect and has finite resistivity (ρ), it will cause power loss during the movement of the charge due to its some intrinsic resistance ($R_{intrinsic}$, Ω) **(Eqn. 18) (Morel et al. 2018)**. Such an electric power loss is termed as dielectric loss, which is obvious in the phase lag between electric field applied to it and the resultant dielectric displacement **(Cain et al. 2002)**. This dielectric loss is measured from the tangent of phase angle, tanδ, and the resultant power loss in the capacitor (P_{loss},W) is measured using the dielectric loss (tanδ), capacitance (C), applied voltage (V), and angular frequency (ω) **(Eqn. 19)**.

$$R_{intrinscic} = \frac{\rho d}{A} \quad (\mathbf{Eqn.\,18})$$

$$P_{loss} = \omega C V^2 \tan\delta \quad (\mathbf{Eqn.\,19})$$

2.3.5. Mechanical loss is (Q_{loss})

Finally, as piezoelectric material does not behave like a perfect elastic material, there will be a mechanical loss in form of heat or sound in the material during the transduction and this loss needs to be minimum **(Cain et al. 2002)**. Since, a piezoelectric material deforms under electric field, its behavior could be considered as a passive elastic material based on Hooke's law (stress ∝ strain), where the piezoelectric stress constant (e, N/V-m) could be calculated from the product of its piezoelectric strain constant (d, C/N) and elastic stiffness constant (c^E) **(Eqn. 20) (Shung and Zippuro 1996)**. The notation used for this mechanical loss is (Q_{loss}), which is inverse of mechanical quality factor (Q_m).

$$e = c^E d \quad (\mathbf{Eqn.\,20})$$

For sensitive transducers, piezoelectric materials with low tanδ (≤ 0.05) and low Q_{Loss} (≥ 10) are taken into consideration **(Smith and Auld 1991)**. Structural strength, shapeability, thermal stability, etc., are few of the other technological pre-requisites that are often taken into account for transducer application.

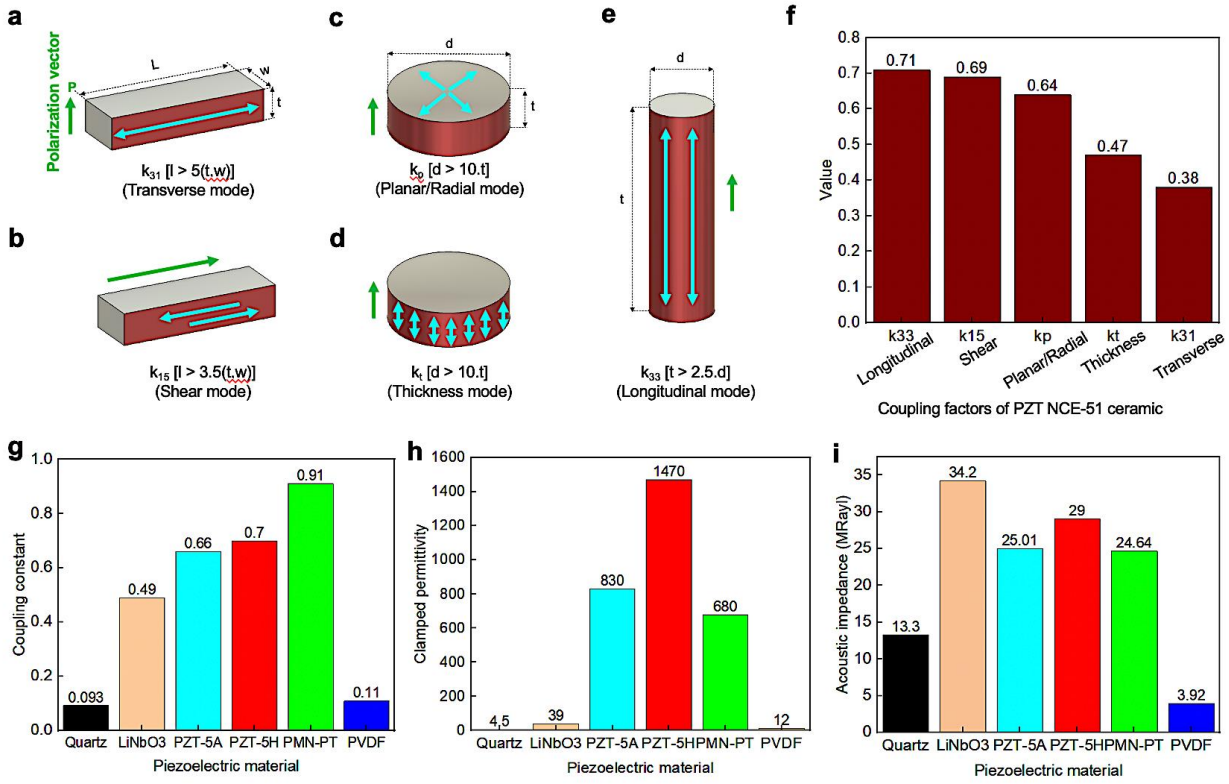

Figure 2.4: Critical parameters of piezoelectric materials for transducer applications. **(a-e)** Five resonance geometries of piezoelectric materials: a thin plate employed for transverse (or transverse length) and the shear (or thickness shear) mode, a thin disc for radial (or planar) and thickness (or thickness extension), and a cylinder for the longitudinal length mode. **(f)** Values of electromechanical coupling factors of soft piezoelectric material PZT NCE-51 based on its different geometries and resultant vibration modes. **(g-i)** Comparative study of coupling constants, clamped permittivity, and acoustic impedance among five different piezoelectric materials **(based on data from (Szabo and Lewin 2007)).**

2.4. Structure and configurations of ultrasound transducers

2.4.1. Backing layer

An ideal medical ultrasound transducer meets all the required piezoelectric properties as mentioned in the segment above and is made of four components as shown in **Figure 2.5(a-b):** piezoelectric element (functional active layer), matching layer, backing layer, and acoustic lens. As depicted in the **Figure 2.5b**, an ultrasound transducer comprises two acoustic (or mechanical) ports (housed at the front (matching layer) and rear (backing layer) side of the piezoelectric material) and one electrical port connected to the driving/receiving circuits.

Alongside the active element, the passive layers (i.e., matching and backing layers) play important roles in maximizing the performance of the transducer. When a piezoelectric ceramic is activated, for example, it rings (or vibrates) at its resonance frequency. A backing layer with a high inherent attenuation factor is often used to attenuate the ringing effect of the oscillated ceramic and limit the back propagation of the electromechanical force, ensuring that energy is only irradiated forward. **(Persson and Hertz 1985)**. It is desirable for pulse-echo applications, as lowering the ringing effect lowers the pulse length or duration and increases the bandwidth. Beside attenuation, acoustic impedance of backing layer is also a critical parameter **(Persson and Hertz 1985)**. It was found that, a backing layer with 5 MRayl has lower damping (i.e., short pulse length) compared to a backing layer of 24 MRayl (i.e., shorter pulse length). However, the sensitivity of the transducer is higher for the former one compared to the latter because the latter one absorbs more energy. Consequently, a compromise between sensitivity and pulse duration is frequently employed to maximize sensitivity of a transducer by adjusting the backing layer impedance. Tungsten-loaded epoxy are quite popular for backing material **(Sayers and Tait 1984; K. K. Shung and Zippuro 1996).** It was found that a mixture ratio of 1:4 (epoxy: tungsten) provides an acoustic impedance of ~5 MRayl and increases the bandwidth of high-frequency (2MHz) PZT transduces by 16% **(Abas et al. 2010)**. Another work reported a comparable impedance of 5.92 MRayl that demonstrated an ultrasound velocity of around 2300 m/s **(Zhou et al. 2014).** Although the impedance could be further increased to ~7.5 MRayl by increasing the mixture ratio to the

saturation point, i.e., 1:8, the bandwidth gain was not significant, which only hikes by 1.5% **(Abas et al. 2010)**. Interestingly, the attenuation factor was ~1 dB/mm (10dB/cm) stable for the mixture ratio between 1:1 and 1:8. Hence, from an economic point of view, 1:4 would be an optimum mixture ratio. It must be noted that, the overall thickness of the backing layer is often kept between $7\lambda_{backing}$ and $10\lambda_{backing}$ for conformable or wearable ultrasound transducer. In such a case, the particle size or volume fraction of tungsten fillers (1, 3, 5, and 50 μm) could be adjusted with spurr resin to ensure the required thickness is obtained at a target impedance (7, 9.7, 10.8, and 14.6 MRayl) and attenuation factor (40, 39, 42, and 178 dB/cm) **(Grewe et al. 1990)**. The absorbed energy fraction (T) entering into the backing layer could be calculated **(Eqn. 21) (Sayers and Tait 1984):**

$$T = \frac{4.Z_{piezo}.Z_{Backing}}{\left(Z_{piezo} + Z_{Backing}\right)^2}$$

$$= \frac{4.\left(\rho_{piezo.}\ c_{piezo}\right).\left(\rho_{Backing.}\ c_{Backing}\right)}{\left[\left(\rho_{piezo.}\ c_{piezo}\right) + \left(\rho_{Backing.}\ c_{Backing}\right)\right]^2} \quad \textbf{(Eqn. 21)}$$

2.4.2. Matching layer and acoustic lens

Sensitivity of a heavily backed ceramic could be increased by the order of 10dB by introducing a quarter-wave (1/4λ) thick acoustic matching layer between the ceramic and loading medium or tissue factor; however, the pulse length is also increased **(Persson and Hertz 1985)**. In addition, the matching layer will allow a smooth transmission of the propagated ultrasound wave into the tissue by having a low acoustic impedance comparable to that of the tissue **(Hunt, Arditi, and Foster 1983)**. Theoretically, with this quarter-wave thick ($t_{matching}$) matching layer and a matching layer material acoustic impedance of $Z_{matching}$, approximately a 100% sinusoidal acoustic wave transmission is proved theoretically **(Zhou et al. 2014)**. Hence, precluding impedance mismatch among piezoelectric element (e.g., 30-35 MRayl for PZT), matching layer, and loading medium (e.g., 1.5 MRayl for tissue) is significant. Epotek 301 (Z_E = 3.05 MRayl, c_E = 2650 m/s), 301-2 alumina-loaded epoxy 301 (Z_A = 3-5.5 MRayl, c_A = 2650-2800 m/s), silver-loaded epoxy 301 (Z_S = 7.3 MRayl, c_S = 1900 m/s), parylene 301 (Z_P = 2.6 MRayl, c_P = 2200 m/s), and zirconia-loaded

epoxy (4:1) (Z_Z = 8.1 MRayl, c_Z = 2750 m/s) are few of the matching layers that are used in transducer design **(Zhang et al. 2018; Zhou et al. 2014).** Impedance for a single quarter-wave length thick matching layer and its thickness are calculated by the following equation (**Eqns. 22-23) (Hunt, Arditi, and Foster 1983)**.

$$Z_{\text{matching}} = \sqrt{Z_{\text{piezo}} . Z_{\text{Tissue}}} \ (\mathbf{Eqn.\ 22})$$

$$t_{\text{matching}} = {\lambda_m}/{4} \ (\mathbf{Eqn.\ 23})$$

However, to create a highly sensitive and broadband transducer, two quarter wavelength matching layers might be employed. The ideal acoustic impedances of the first (inner) matching layer (Z_{m1}) and the second (outer) matching layer (Z_{m2}) could be computed using **Eqns. (24-25)**. Once the acoustic velocities for the matching layers are measured their thicknesses are calculated using **Eqns. (26-27)** for use in the transducer. A group of researchers implemented a similar approach utilizing eco-friendly high frequency (50 MHz) imaging transducer that demonstrated an efficient coupling (or k) factor of 0.45 with two acoustic matching components (Z_{m1} = 8.07 MRayl and Z_{m2}= 2.28 MRayl) (R. Chen et al. 2019)**.**

$$Z_{m1} = (Z_{\text{piezo}}^4 . \ Z_{\text{Tissue}}^3)^{\frac{1}{7}} \ldots . (\mathbf{Eqn.\ 24})$$

$$Z_{m2} = (\ Z_{\text{piezo}} . \ Z_{\text{Tissue}}^6)^{\frac{1}{7}} \ldots . (\mathbf{Eqn.\ 25})$$

$$t_{m1} = {\lambda_{m1}}/{4} \ldots . (\mathbf{Eqn.\ 26})$$

$$t_{m2} = {\lambda_{m2}}/{4} \ldots . (\mathbf{Eqn.\ 27})$$

On the other hand, the acoustic lens not only safeguards the acoustic matching layers but also focuses the ultrasound beam at a certain distance. The elastic, piezoelectric, and electrical characteristics of the piezoelectric material significantly influence the sensitivity of a transducer and the image quality.

2.4.3. Operating modes of piezoelectrics and structure of transducer

The active piezoelectric layer is the backbone of a medical transducer **(Szabo 2014)**. Selection of the piezoelectric operating modes for end-use application is one of the key factors for designing ultrasound transducers. The most common modes are d_{33} **(Figure 2.5d)** and d_{31} **(Fig. 2.5g),** which are defined in regards to the direction of polarization **(Figure 2.5c).** In d_{33} mode, the polarization and strain are in same direction, causing a large coupling factor, whereas they are perpendicular to each other in d_{31} mode, resulting in a lower coupling factor. The plate **(Figure 2.5e)**, composite **(Figures 2.5f),** and diaphragm **(Figure 2.5h)** architectures are the three major basic transducer configurations, which utilize these two operating modes. In medical industries, the end-use application requirements are met by pairing the device design architecture with a piezoelectric operating mode. For instance, single element plate and composite array transducers are efficient in high-frequency medical imaging applications **(Cannata et al. 2003; Zipparo, Shung, and Shrout 1997)**. Since, the device architecture employs the d_{33} mode, its anti-resonance frequency and longitudinal velocity (or acoustic impedance) depends on the thickness of the piezoelectric material **(Kim et al. 2020; Qiu et al. 2015).** As a result, the transducer geometry is constrained due to the dependence of its operating frequency on the thickness, which limits its structure-specific applications.

The bulk piezoelectric arrays employing the d_{33} mode has two more major drawbacks: (i) the pitch (=width of piezo-pixel + width of kerf) of the device is limited by the blade width when a dice-fill fabrication technology is used and (ii) accessibility to the diced piezo pixel could be extremely difficult for wire bonding, which could restrict them to flip-chip-bonding to the CMOS chip to access the pixels individually **(Sadeghpour et al. 2021)**. In such a case, pMUTs could be employed, utilizing their d_{31} mode for sensing, actuation and even imaging **(Qiu et al. 2015)**. However, pMUTs suffer from some fundamental challenges. For instance, the piezoelectric constant (d, pC/N) of the piezoelectric thin film polymer is smaller than the bulk PZT (lead zirconate titanate), ZnO (zinc oxide) and AIN (aluminum nitride) used in MEMS (Katherine Marie Smyth 2012). Another major setback is its low effective electro-mechanical coupling coefficient (k_{eff}). The maximum theoretical value for pMUT, for instance is ($k^2_{31} \approx$) 20%, although the reported value is ($k_{eff}{}^2 \approx$) 9% so far **(Krishnan, and Arora 2023; Smyth, Sodini, and Kim 2017).**

One of the major drawbacks of conventional bulk piezoelectric material is their high acoustic impedance ($Z_{acoustic}$ ≈ 20-30 MRayls), although they meet the other four major criteria: high k-coefficient (≈0.5), large ϵ (≈100-2400), low tanδ ($\leq$ 0.02), and low Q_{loss} (≈10-1000) **(Smith and Auld 1991)**. Hence, they require the integration of acoustic matching technology to match the impedance of the skin, which is close to 1.5 MRayls. On the other hand, piezoelectric polymers like PVDF (polyvinylidene difluoride) offer low acoustic impedance ($Z_{acoustic}$ ≈ 4 MRayls), but they suffer from poor k-coefficient ($\leq$ 0.3). As a result, they perform poor as transmitting transducers. Contrarily, they are good suit for receiver transducer due to their wide bandwidth. As a result they are often used in hydrophones **(Szabo and Lewin 2007).** Also, their sensitivity is significantly degraded due to high dielectric loss (tanδ ≈ 0.15) **(Smith and Auld 1991).**. Further, their comparatively smaller dielectric constant (ϵ ≈10) puts high pressure on the demands of the transmitter/receiver electronic circuitry. To solve the tradeoffs between piezopolymers and piezoceramics, composite piezoelectrics, operating in d_{33} mode are used in the industry, which meets all the five criteria: (i) high k-coefficient (≈0.6-0.75), (ii) low $Z_{acoustic}$ (<10 MRayls) – almost reaching the range of piezopolymer, (iii) large ϵ (≈10-1000), (iv) low tanδ, and (v) low Q_{loss}. As a result, 1-3 composite transducers are popular for both imaging **(Sun et al. 2010)** and energy harvesting bioelectronics **(Jiang et al. 2022)**. A comparative synopsis of these three configurations is provided in **Fig. 2.5(i) (Turner et al. 2021)).**

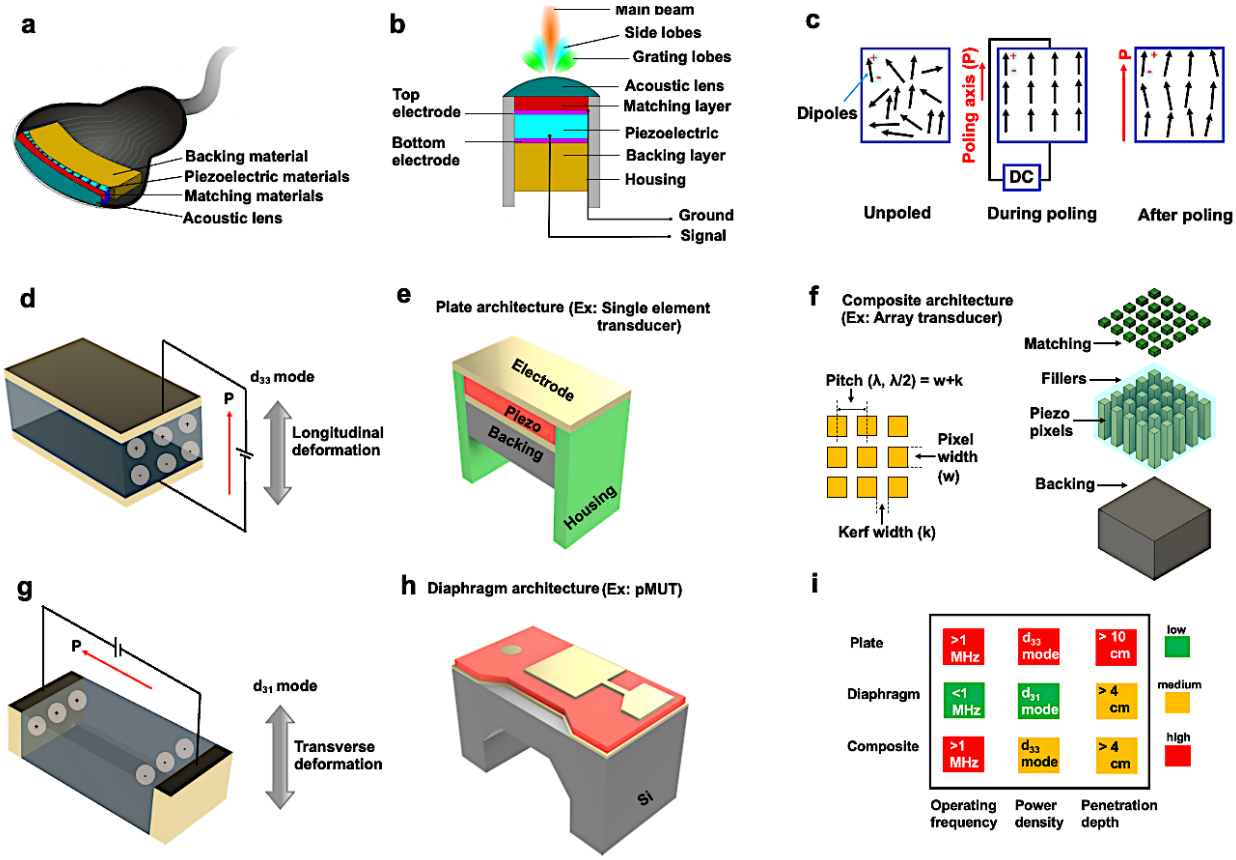

Figure 2.5: Architecture of a medical ultrasound transducer. **(a)** Schematic of a commercial hand-held ultrasound transducer and the **(b)** cross-section illustrating the building blocks of the transducer. **(c)** The polarization process of piezoelectric materials to strongly align the dipoles for optimum piezoelectric effect. **(d)** A schematic diagram outlining the piezoelectric d_{33} operating mode and its application in **(e)** plate and **(f)** composite architectures. **(g)** d_{31} operating mode, which are typically used in **(h)** pMUT or thin film architecture. **(i)** Comparison among three conventional transducer architectures (based on data from **(Turner et al. 2021)).**

2.5. Different types of array geometries

When compared to conventional monolithic or single-element transducers, transducer arrays have three significant benefits. First, as opposed to a single element transducer, a specific array may perform a variety of various inspections without moving from one spot to another, making it more versatile than the latter. Second, it is possible to acquire images at each test position using different array geometries (excluding the annular arrays). Consequently, the internal structure of any test

component may be quickly visualized with a wide view of angle. Third, the phased array transducer allows electrical steering instead of mechanical steering that is employed by single-element transducer.

In addition, an array has the potential to produce ultrasonic wave fields of an almost limitless variety; examples include, rectangular or plane wave, cylindrical wave, 3D spherical wave. Yet, the most typical use for them is to generate fields that are analogous to those generated by conventional single-element transducers, namely plane, focused, and steered beams. Szabo and Lewin has illustrated the 9 possible imaging formats (2D rectangular, 2D sector, 2D convex, 2D trapezoidal, 3D parallelepiped, 3D fan shape, 3D truncated prism, 2D donut, and 3d tube) with 8 different transducer arrays (linear array, phased array, convex array, endo-array, 2D-array, mechanically scanned linear and convex array, and IVUS transducer arrays) for proper medical ultrasound imaging **(Szabo and Lewin 2013)**.

The major geometric difference between linear and linear phased array (aka phased array) configuration lies in their pitch, i.e., distance between centers of two piezo-elements) **(Shung 2002)**. If the pitch is greater than half wave-length but less than one wave-length, then the array is called a linear array; whereas, a phased array is designed with a pitch less than half wave-length. Due to this smaller pitch length, phased arrays allow beam steering without inducing any grating lobes. The number of side lobes grows as the element spacing is raised to one wavelength. The side lobes and grating lobes of an ultrasonic beam are undesirable as they are produced off-axis and generate image artifacts due to an inaccuracy in locating the returning echo **(Paul et al. 1997).** Hence, phased array is non-trivial for biomedical imaging for lowering the lobes.

Figure 2.6 illustrates different types of array geometries. In 1D arrays, the piezo-components are laid out along the x-direction, and they are often rather long in the y-direction. As a result, they behave like sources of long strips. Hence, the ultrasound image that is formed is a flat, 2D representation sitting on the x–z plane. In 1.5D arrays, the main image plane is still the x-axis, which runs along the rows of elements. However, the additional rows lower their beam steering capability. Unlike 1D linear arrays, which are restricted to a single steering plane and the scanning

of 2D slices, 2D linear matrix array transducers are used to focus the beam over a 3D slice. The linear geometry of this 2D matrix array could be converted to a phased geometry to enable beam steering. Annular arrays are slightly distinct from other types of arrays due to the fact that their sole purpose is to offer a changing focal depth and they do not permit beam steering in any circumstance. Interestingly, a 2D segmented annular array is capable of 3D volumetric imaging analogous to its equivalent 2D squared matrix array but at a reduced grating lobes, augmenting the image contrast **(Martínez 2003)**. It must be noted that both circular phased array and 2D segmented annular arrays have the capability to demonstrate comparable imaging performance as a fully populated array of the same size **(Drinkwater and Wilcox 2006).**

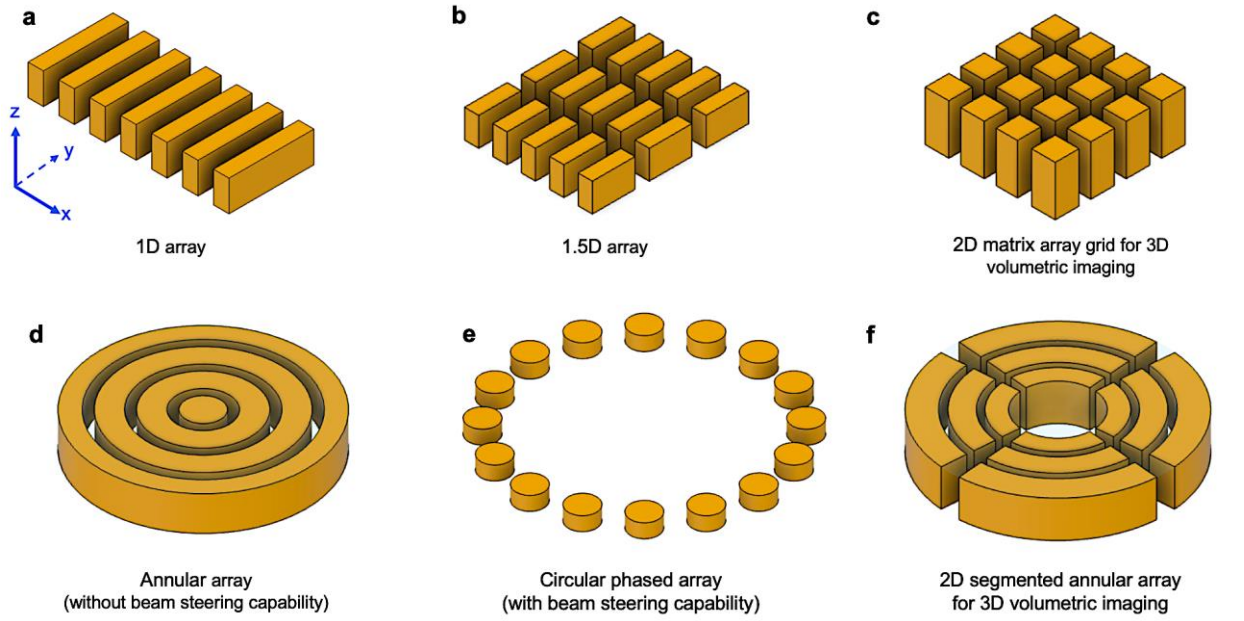

Figure 2.6: Different types of array geometries: **(a)** 1D array, **(b)** 1.5D array, **(c)** 2D array, **(d)** annular array, **(e)** circular phased array, and **(f)** a 2D segmented annular array capable of medical imaging similar to a fully populated array.

2.6. Modelling of transducer

2.6.1. One dimensional KLM model

A 1D equivalent circuit model is frequently adequate to represent the thickness vibrations mode that is employed in ultrasound imaging. Although, there are numerous models, but the most commonly utilized ones are Krimholtz, Leedom, and Matthaei (KLM), Mason, and Redwood models. The KLM model could be used to model the thickness mode resonance of the piezoelectric transducer for this research **(Krimholtz, Leedom, and Matthaei 1970)**. A piezoelectric transducer could be considered as a 3-port acoustic and electrical network system as illustrated in **Figure 2.7a,** similar to a piezoelectric resonator. The equivalent KLM circuit model is displayed in **Figure 2.7b (Szabo 2014),** where the k_t (electromechanical coupling constant) is used for the thickness expander mode**.** The port #3 (electrical port) signifies the electrical connectivity between the piezoelectric clamped transducer and the driving/receiving circuits. The driving voltage is applied to the piezoelectric transducer through this port that produces the acoustic force (F) at the respective face of the piezoelectric material. To dampen the back propagation of the electromechanical force, a backing load with high attenuation factor is used. For smooth transmission of the transmitted ultrasound wave into the tissue, matching layers with substantially lower impedances are employed, closer to the impedance of the human tissue. These matching and backing loads are mechanically connected to the acoustic ports #1 and #2.

In the KLM model, the acoustic center is artificially developed by segmenting the thickness of (d_0), piezoelectric material into two halves ($d_0/2$). The right side (R) port #1 (equivalent load, $Z_R = Z_W$) is considered for transmitting the acoustic energy into the tissue (or water) (Z_W), while the left side (L) port #2 (equivalent load, $Z_L = Z_B$) radiates the energy into the backing layer (Z_B). Z_{rlay} is the acoustic impedance of the matching layers in series. Finally, the model includes a capacitor C_o, impedance jX_1, and a transformer with the ratio ($1:\phi$) for converting an electrical signal into acoustical counterparts.

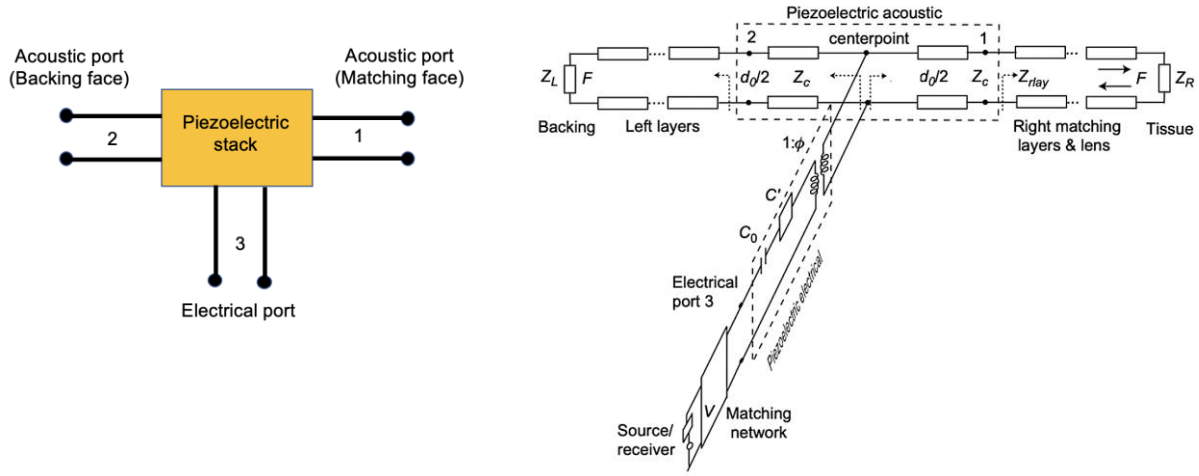

(a) **(b)**

Figure 2.7: KLM model for simulating the performance of ultrasound transducer. **(a)** The three-port network system of a piezoelectric transducer used in this research work. **(b)** Equivalent circuit transducer model to mimic a single clamped pixel of the array **(Szabo 2014).**

Krimholtz et al. gave the values for these parameters **(Eqns. 28-31)** (Krimholtz, Leedom, and Matthaei 1970)**:**

$$Z_c = \rho c A \quad (\mathbf{Eqn.\,28})$$

$$C_0 = {\varepsilon^S A}/{d_0} \quad (\mathbf{Eqn.\,29})$$

$$X_1 = \frac{h^2}{\omega^2 Z_0}\sin\left(\frac{\omega d_0}{c}\right) \quad (\mathbf{Eqn.\,30})$$

$$\phi = \frac{\omega Z_0}{2h}\,\mathrm{cosec}\left(\frac{\omega d_0}{2c}\right) \quad (\mathbf{Eqn.\,31})$$

Here,

Z_o = acoustic impedance

C_0, ε^S = clamped capacitance and permittivity of piezoelectric

ε^S = clamped permittivity of piezoelectric under zero voltage,

h = piezoelectric pressure constant for the crystal/ceramic,

r = density

c = speed of longitudinal sound waves in the crystal/ceramic

The piezoelectric parameters that are critical for this model are the: (i) thickness (d_0), (ii) relative permittivity ($\varepsilon^T/\ \varepsilon_0$), (iii) relative clamped permittivity ($\varepsilon^S/\ \varepsilon_0$), (iv) k_t, (v) area (A=l x w), (vi) Z_C, (vii) r (viii), and (ix) c. Also, using similar material properties, the KLM model could be used to define the geometry of matching ($\lambda/4$) and backing loads (5-10λ) to amplify bandwidth (typically >50%) and prevent the mismatch of acoustic impedance gradient between the body tissue and the

PZT pixels and, thereby, maximizing the transmission of the acoustic wave to the propagation medium.

2.6.2. Finite element model (FEM)

1D models have some limitations. For example, 1D models do not account for the acoustical attenuation coefficient of backing material **(Assaad et al. 1996).** The 1D models assume that the acoustic waves transmitted to the backing layer are not reflected. In practice, however, backing layers with a lower attenuation factor will reflect waves, which might interfere with the front-side echo. Also, most 1D models can only model vibration/oscillation in one-dimension **(Chaudhary 2007).** Consequently, 1D model does not model acoustic rays going at angles, which would result in different frequency responses due to the different path lengths through the various layers **(Medina 2005).** While FEM-based software like COMSOL could be used for designing transducers and address such issues, the KLM model remains the most used technique due to its ease of use and accuracy **(Li 2017).** Nonetheless, when frequency rises, FEM simulation time will grow dramatically.

Chapter 3

3. Fabrication and Characterization

In this chapter, the process of designing the 2D ultrasound transducer from bulk piezoelectric material will be discussed. Also, it will provide the techniques for characterizing the transducers that were constructed.

3.1.Materials

Commercial PZT-5H ceramics (Hongsheng Electronic Equipment Co. Ltd, Baoding, China) (**Figure 3.1)** and EPO-TEK 301epoxy resin (Epoxy Technology, MA, USA) were used in the current study as the active piezoelectric material and polymer matrix, respectively. **Table 3** exhibits the properties of PZT-5H material. For matching layer and backing layer epoxy-loaded zirconium oxide (5 μm) (Sigma-Aldrich, USA) and tungsten (1-5 μm) (Thermo Scientific, USA) were used based on the literatures as discussed in **Sections 2.4.1-2.4.2 (Chapter 2)**. For dicing purpose, different blades were used made by DISCO Corp. (Japan).

Figure 3.1: Materials used for transducer fabrication: **(a)** PZT bulk material diced into smaller pieces; **(b)** epoxy resin; **(c)** zirconium oxide and tungsten; **(d)** zirconium-load matching (top), tungsten-loaded backing layer (bottom); and **(d)** blade for dicing.

Table 3: Properties of PZT-5H piezoelectric ceramics (based on the specification sheet provided by Hongsheng Electronic Equipment Co. Ltd, Baoding, China).

Category	**Property**	**Unit**
Piezoelectric strain constant (d_{ij})	Piezoelectric strain constant d_{33}	670 C/N
	Piezoelectric strain constant d_{31}	186 C/N
	Piezoelectric strain constant d_{15}	660 C/N
Dielectric constant	Relative permittivity $\varepsilon^T/\varepsilon_0$	4200
	Relative clamped permittivity $\varepsilon^S/\varepsilon_0$	1300
Electromechanical coupling constant (k_{ij})	Thickness coupling constant k_t	0.50
	Planar coupling constant k_p	0.60
	Longitudinal coupling constant k_{33}	0.68
	Transverse coupling constant k_{31}	0.38
	Shear coupling constant k_{15}	0.65
Acoustic parameter	Acoustic impedance Z_{33}	30.8 MRayl
Other parameters	Density ρ	7450 kg/m^3
	Curie temperature T_c	200 ^{o}C
	Dielectric loss tangent tan δ	2.3%
	Mechanical quality factor Q_m	70
	Grain size	7 – 10 μm

3.2.Impedance spectrum and frequency constant of PZT-5H

A KEYSIGHT E4990A impedance analyzer (KEYSIGHT Technologies, USA) and Kelvin/Alligator clip leads KEYSIGHT 16089B ((KEYSIGHT Technologies, USA) were used (**Figure 3.2)** to analyze the impedance-phase spectrum of a bulk piezoelectric ceramics to characterize the frequency constant (N or 2ft). A 50-ohm resistor was utilized for calibration of the impedance analyzer. A digital thickness meter (Neoteck) was used to measure the dimensions of the ceramic that had a length, width, and thickness of 57.2 mm, 35 mm, and 2 mm, respectively. The meter had a resolution up to 0.001 mm/ (0.00005") with a measuring range of 0 ~ 0.5 inch/ (0 ~ 12.7 mm). These tools allowed to measure the phase-impedance spectrum of different PZT-5H ceramic specimens.

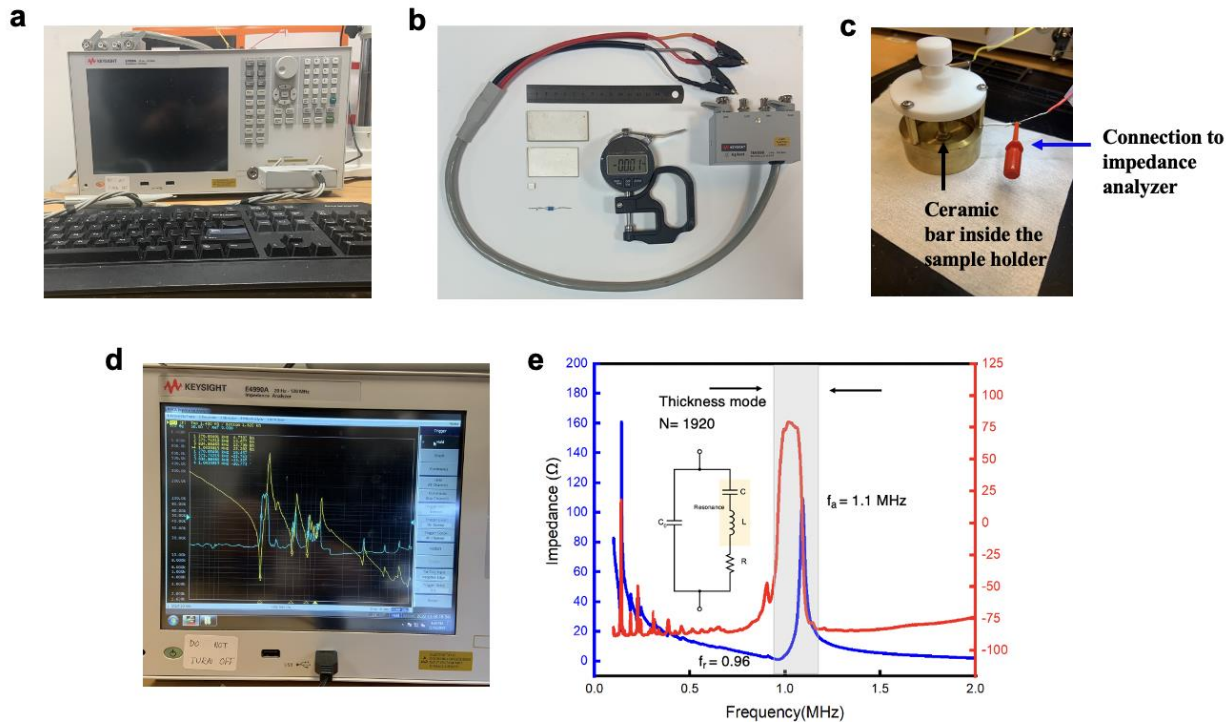

Figure 3.2: Impedance-phase spectrum measurement tools. **(a)** KEYSIGHT E4990A impedance analyzer; **(b)** PZT-5H piezoelectric ceramics, KEYSIGHT 16089B Kelvin clip leads, 50-ohm resistor, Neoteck digital thickness gauge, ruler; **(c)** a probe to measure impedance-phase spectrum of the smaller 2mm bulk ceramic pieces; **(d-e)** phase-impedance spectrum of different modes of different specimens.

3.3.Selection of the transducer design: 2D phased array transducer

The configuration of the 2D phased array transducer is shown in **Figure 3.3**. The device is a composite of 32x32 PZT matrix structure and a resin polymer system, which would form the expected spherical beam required. Since piezoelectric ceramics are brittle, they are difficult to process; however, polymers are flexible and, that is why, they are added with piezo ceramics to produce composites of different geometries **(Yao et al. 2009).**

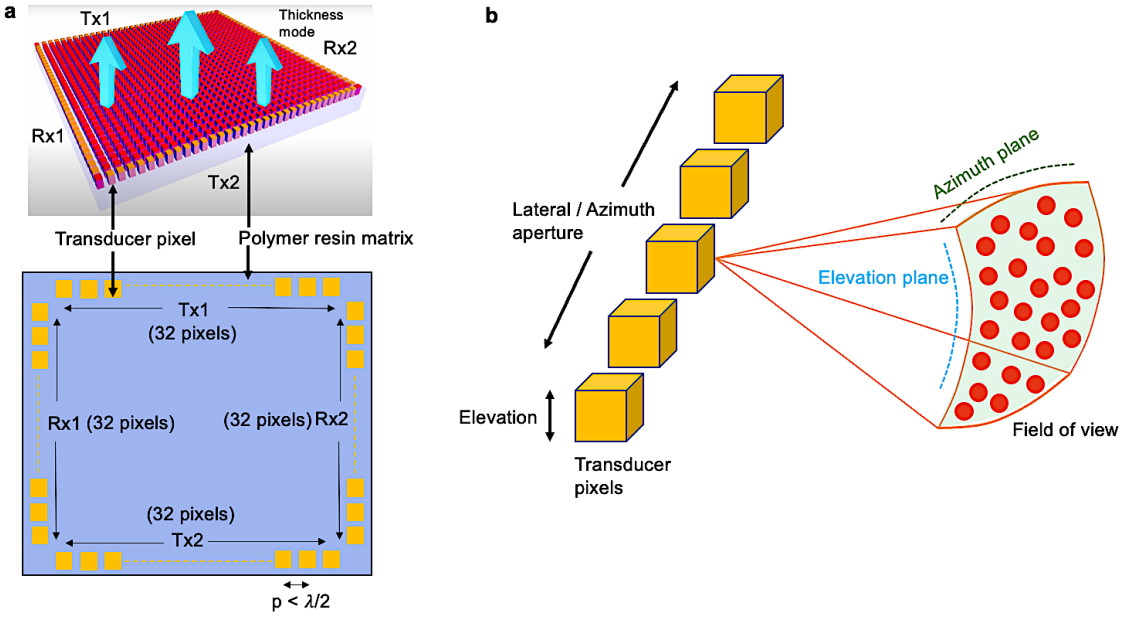

Figure 3.3: Schematic of the 2D PZT-5H composite transducer array. **(a)** Configuration the 32x32 sparse phased array. **(b)** Expected wave profile for beam formation using the square-shaped PZT pixels of the 2D sparse arrays.

The functional 2D transducer area is designed with a four-sided box shape rather than a fully populated 2D array, as well as transmit (T_X) and receive (R_X) elements that are perpetually assigned. Although there are 32x32 (=1024) pixels available in the fabricated 2D transducer design, the current work will only employ 128 (=4x32) functional pixels. In addition to cutting down on price, power usage, and active piezoelectric channels, this architecture also allows for a significant drop in the number of R_X channels and related electronics from 4096 (=64x64) to

64(=32+32) channels. Consequently, there is no information redundancy in the T_X/R_X signal matrix due to optimal minimization of the 2D array elements.

Hence, there will be 64 (=2x32) pixels in total to be employed for the two transmitters (T_X-1, T_X-2) and the rest 64 (=128-64) pixels for two receivers (R_X-1, R_X-2) to ensure a sparse array configuration (**Figure 3.3)**. As we can see in literatures, the standard ultrasound array is fully populated in 2D and 1D configuration space, utilizing all the elements of an array. In contrast, the array pixels for the current work have all zeros except the edges, making it sparse as it turns out that the actual image information in sparse is exactly the same way that a fully populated 2D array would produce. Hence, it is possible to actually obtain all the image information using the sparse array, except now using the optimal number of physical elements. **Section 2.5 (Chapter 2)** has also introduced literatures with similar array architectures, including phased and segmented arrays capable of display imaging performance on par with a fully populated array.

There are two major challenges that needs to be addressed while fabricating this sparse array architecture: (i) difficulty to physical fabricate the sparse transducer array due to its smaller pitch ($p < \lambda/2 = 102$ μm) size, and (ii) connecting each piezoelectric pixel with the electrical port to ensure minimal dead elements. To address the first challenge, the current research has developed a recipe for the dicing tool with a new custom-made dicing blade (in collaboration with DISCO, Japan) for micromachining the phased transducer array to ensure the transducer can electrically steer the beam instead of mechanical or manual steering that is used with the conventional linear arrays. As mechanical steering will not be necessary, such technology of the current work could also allow to fix and embed them in a flexible patch to conform with the curvilinear surface of the human body and image the full organ. Also, the work will explore avenues to develop a simulation model using KLM theory to optimize the performance of the device and compare its bandwidth with different matching and backing loads for the acoustic port of the transducer. The scope of the KLM model for the k_{33} mode piezoelectric transducers is discussed later. Finally, to address the second challenge, a microfabrication recipe has been developed to draw and pattern a robust electrical circuit on the array that will ensure each element is independently connected. Details about the micromachining and photolithography protocol are discussed later.

3.4.Fabrication of 2D phased array transducer

The parameters used in the 2D transducer array design are presented in the **Table 4**. The width of the kerf and piezo-pixel was determined by the blade thickness and the vibration. DISCO DAD 321 (DISCO, Japan) was employed with a 15 μm-thick synthetic diamond micromachining blade to fabricate the 32x32 2D transducer array. I designed the required parameters of the 15 μm-thick ultra-thin dicing blade compliant with the DISCO DAD, especially considering the blade aspect ratio (diameter: 51.1mm; thickness: 0.015mm) and the blade exposure (= (51.1-49.4)/2= 0.85mm) that relies on the flange diameter (49.4mm), to maximize the piezoelectric footprint by reducing the kerf width that would arise from mechanical vibration compared to the available commercial ones, 0.25 μm-thick blade (with similar blade diameter of 51.1 mm) for example. The utilization of a meticulously chosen aspect ratio serves to prevent the blade from experiencing deformation or generating irregular cutting patterns like wavy cuts. In addition to the selection of an appropriate blade aspect ratio for this given machining application, the choice of blade exposure was a crucial factor in blade design process, particularly in the context of designing high-frequency transducers. In the blade design process, the exposure duration was carefully maintained to satisfy three essential requirements: (i) effectively sever the PZT-5H material during dicing, (ii) partial penetration into the mounting substrate, and (iii) inclusion of a safety margin to prevent any potential damage to the chuck. In addition to these three factors, it was crucial to minimize blade exposure to prevent subpar cutting quality or, in more severe cases, blade breakage. Multiple iterations were conducted during dicing, employing varying feed speeds and spindle revolutions per minute (rpm), while utilizing blades with distinct thicknesses. In contrast, the blade that was developed for this work, with a thickness of 15 μm, demonstrated optimal dicing yield and effectively mitigated the risk of fracturing the PZT ceramics. This was observed specifically when the blade was operated at a feed speed of 0.15 mm/s and a rotation rate of 30000 rpm, surpassing the performance of alternative dicing parameters. To protect the piezo-pixels from mechanical damage, the depth was set to 350 μm. The additional depth allows for easier lapping. The design parameters were then sent to DISCO to be physically manufactured. The commercial serial number of this new blade is Z09-SD3000-Y1-60 (51.1x0.015x40). After the dicing, the array was bridged with the conductive epoxy strip (E-SOLDER 3022, Von Roll USA, Inc.) embedded for a ground

electrode, printed with top electrodes via the photolithography process and encased between the matching layers and backing layers using a thin layer of epoxy resin.

Table 4: Design parameters for the 7.5 MHz high frequency ultrasound phased array transducer.

Parameters	**Value**	**Explanation**
Frequency (f)	7.5 MHz	Based on literature
Wavelength (λ)	205.3 μm	$\lambda = c/f = 1540/7.5$
Pitch (p)	102 μm	Based on phased array design requirement (i.e., $p < \lambda/2$)
Piezo-pixel width (l)	65-70 μm	Determined by the blade thickness and vibration
Kerf	37-32 μm	Determined by the blade thickness and vibration
Piezo-pixel height (t)	250 μm	Based on resonance geometry or frequency constant

3.4.1. Transparent photomask desgin for photolithography

First step of photolithography process involves designing a mask to print the required circuit pattern. Since the current transducer design will utilize the independent pixels at the four edges of the PZT sparse arrays (i.e., transmitter and receiver arrays), it would make the microfabrication even more challenging as a single defect or short-circuit on the photo-lithographically patterned Au electrode surface may cause single or multiple dead elements, and cause catastrophic failure of the device. Consequently, an AUTOCAD software was utilized to generate a computer-aided design (CAD) model. This model was subsequently printed to produce a photolithography mask using a transparent photomask writer (Screen Plate Rite, FX870II, Japan). It is worth noting that each printed line within this mask corresponds to an individual piezo pixel. To prevent any overlap with adjacent printed patterns, meticulous attention was given to maintaining a pitch of 102 μm with a kerf of 32 μm on one end (so that it corresponds to the same pitch used in the array), which connects to the PZT pixels of the transducer array. On the other end, which would be linked to the flexible PCB cable, a pitch of 250 μm (with a kerf of 100 μm) was maintained similar to the pitch of the cable (**Figure 3.4)**. The maintenance of the same pitch ensures the prevention of short-circuiting between adjacent electrodes. Also, proper bonding between the solid-state PZT pixel and the thin-film circuit electrode is critical and challenging because of the difference in modulus of rigidity. Therefore, a standard microfabrication recipe was developed to optimize the adhesion between Au electrodes and the small-scale PZT pixels for this particular transducer design to ensure strong adhesion, which is discussed later in this chapter (detailed in **3.4.3**.).

A set of challenges appeared during the fabrication process, particularly during the photolithography process. Because of the mismatch of thermal coefficient between polymer matrix and the transducer pixel structure – contributed by its low thickness – the matrix may bend around the transducer during soft and hard baking. As a result of which, patterning the electrical circuit on individual PZT element or pixel became challenging during the mask alignment step during the photolithography process. Such a bending creates microcracks on the PZT surfaces and may break the array. Hence, maintaining Au pattern integrity is challenging as chemical etchants will penetrate through the PZT cracks and damage the underlying Au electrodes. As part of the microfabrication process, a miniaturized hot-pressing technique was developed. This technique

involves placing a device under 0.5 lb between two glass plates, each measuring 50 mm x 50 mm x 4.5 mm. The purpose of this technique is to maintain the structural integrity of the device during a controlled thermal treatment at 55ºC.

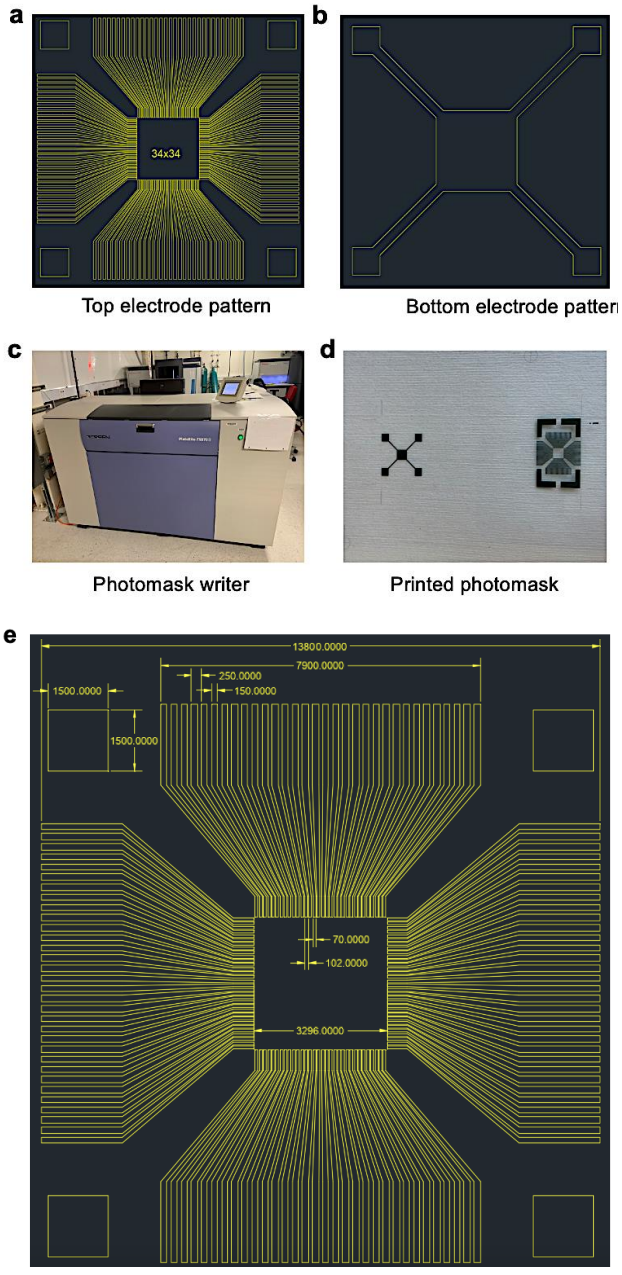

Figure 3.4: Specifications of the photolithography mask for patterning the electric circuit on top of the 2D phased array**: (a-b)** designed pattern for the top and bottom electrode, along with the **(d)** photo of the printed transparent mask using a **(c)** photomask writer; **(e)** specification of the mask (units in μm).

3.4.2. Micromachining a piezoelectric PZT-5H block into a 2D array and connecting with E-solder for ground electrodes

The first step of fabricating a 2D transducer array involves cutting out a small (10 mm x10 mm) square block from a large piezoelectric ceramic wafer employing a coarse blade (thickness: 150μm) and then dicing it into a 36x36 array of independent piezo-pixels using a fine blade (thickness: 15μm). A DAD321 (DAD, Japan) machine (**Figure 3.5)** was employed to complete the dicing after experimenting with different dicing parameters. The optimum dicing yield was obtained when the dicing parameters were set with the new 15μm blade operating at a feed speed of 0.15 mm/s and a rotation rate of 30000 rpm, surpassing the performance of alternative dicing parameters. The dicing steps involved in dicing are shown in the (**Figure 3.6).** The provided diagram demonstrates the initial dicing of the PZT-5H block material along the x-axis, followed by a subsequent dicing in the perpendicular y-axis direction. The goal is to fabricate PZT pixels that possess a square cross-sectional shape to ensure uniform ultrasound beam profile. In order to safeguard the piezo-pixels from potential mechanical damage, a depth of 350 μm was established that facilitated convenience of lapping. Following the process of dicing, the diced material is subsequently filled with a polymer resin (EPO-TEK 301, Epoxy Technologies Inc., USA). This solidified resin serves the purpose of limiting transverse vibration within the PZT array when it is subjected to electrical stimulation. The ratio of mixture for the two-part epoxy resin (EPO-TEK 301) was 20 parts of the viscous resin component to 5 parts of the hardener component. The composite structure was then degassed and cured for 2 hours at 65^{o}C. Similarly, conductive epoxy blocks (E-SOLDER 3022, Von Roll USA, Inc.) for ground electrode were diced into the required specifications (1.5 mm x 1.5 mm) and aligned with the PZT-5H array based on the required architecture to be manually epoxified with EPO-TEK 301 so that they are connected to the array through the matrix system. Once, the array was manually filled with epoxy, it was lapped to the required geometry and was prepared for the next step, i.e., photolithography.

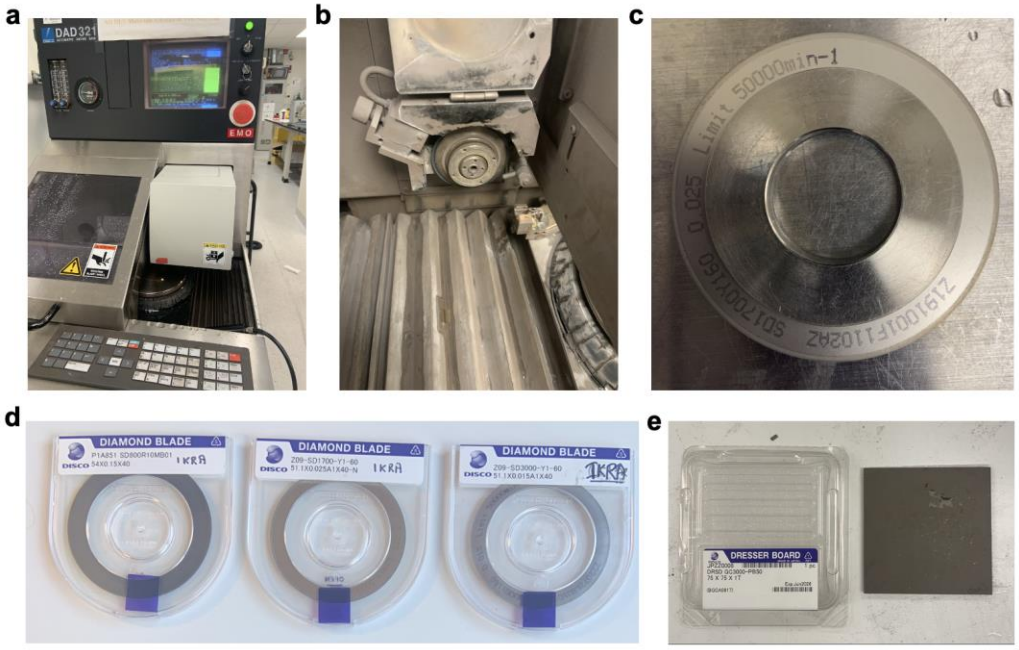

Figure 3.5: Micromachining the PZT-5H: **(a)** DAD321 dicing saw, **(b)** dicing spindle supporting the **(c)** flange and dicing blade, **(d)** different kinds of diamond blade (thickness: 150 μm, 25 μm, and 15 μm), and **(e)** blade dresser.

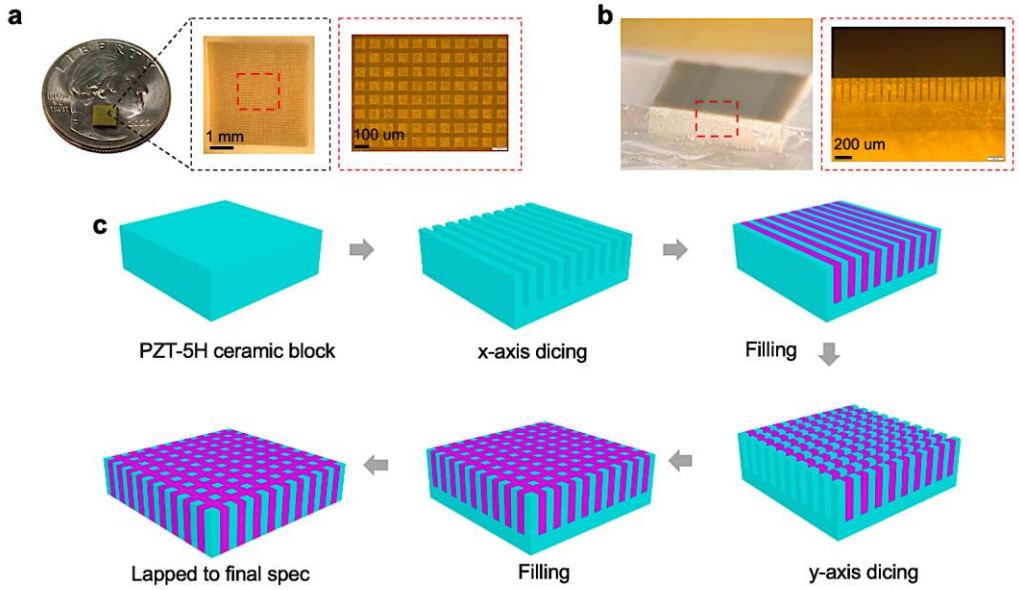

Figure 3.6: An enlarged (a) top view of the diced array, (b) its cross-section, and (c) micro-machining (i.e., dicing) steps to fabricate the fully-populated 2D phased transducer array.

In order to produce an array of 32x32 pixels, a matrix of 34x34 pixels is required to prevent TX/RX pixel overlap at the four edges of the array. Therefore, a 34x34 array must be manufactured for the transducer. In the ideal scenario, the perimeter of the array would appear as depicted in **Figure 3.7a,** but this is not attainable in practice. After the fabrication of the 34x34 matrix, fragments of pixels appear at the perimeter as depicted in **Figures 3.7(b-c).** Therefore, during the electrode patterning phase of the photolithography procedure, these undesirable fragments must be patterned with Au traces **(Figure 3.7d).** Although this is not required, it cannot be avoided. Also during regular operation, the blade loses its volume and geometrical shape **(Lim, Zamri, and Yusoff 2022)**. Consequently, during ceramic dicing the blade may experience chipping due to friction with the ceramic as well as thermal damage or mechanical cracking during high-speed machining, which not only reduces the durability of the blade but also damages and breaks the ceramic due to its brittle nature. Such ceramic damage was frequently observed at borders during machining (**Figures 3.7 (e-f))**. In order to maintain the structural integrity of the 34x34 2D array at the four perimeters, the current work included additional ceramic pixels outside the 34x34 functional area with a length of 195 μm/pixel, which is three times the length of each square pixel (64 μm x 64 μm) of the 34x34 array (as shown in **Figure 3.10**).

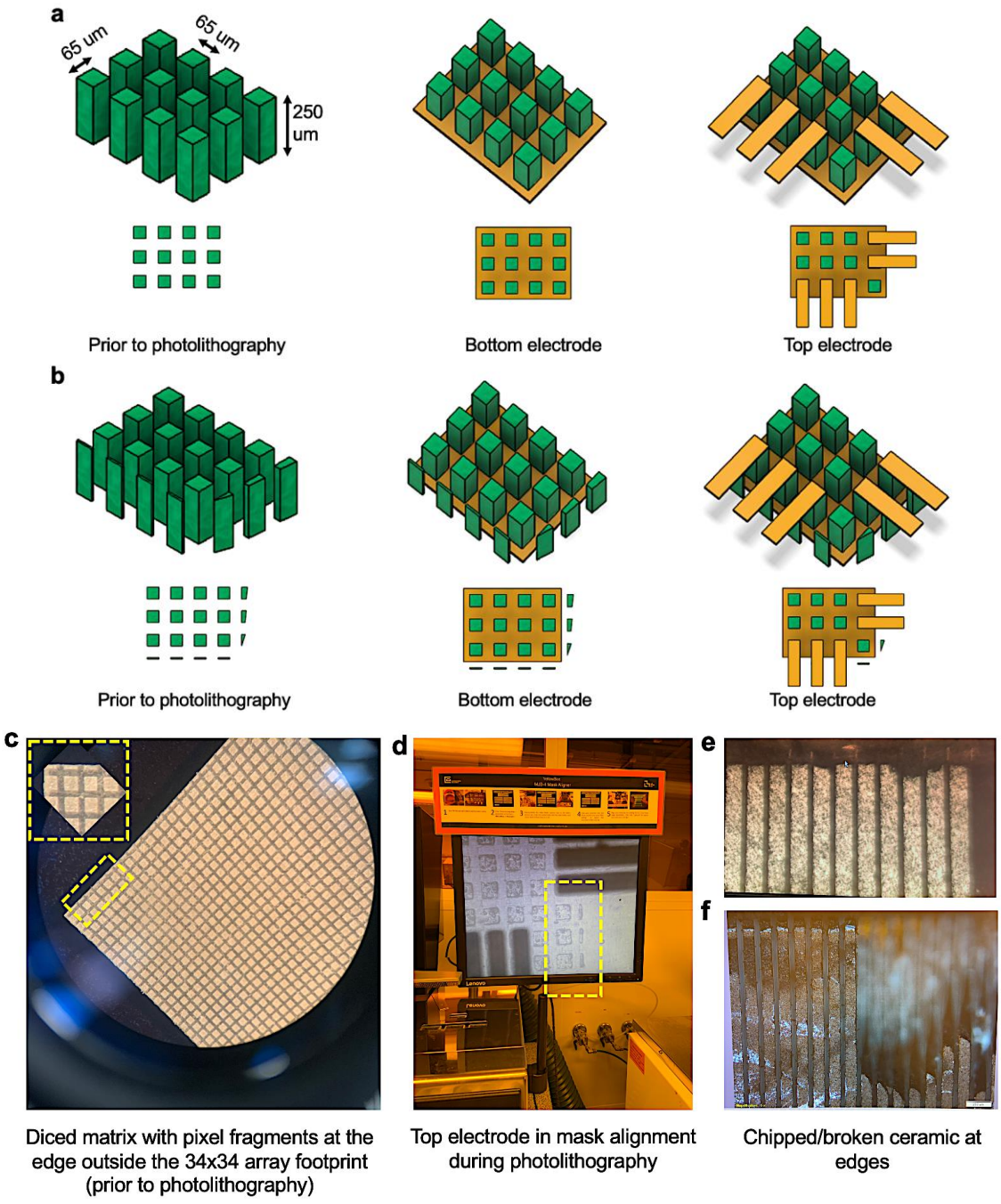

Figure 3.7: Schematic and digital photos of micromachined PZT-5H wafer into micro pixels: **(a)** ideal scenario of a diced 34x34 matrix, **(b-d)** practical real-life scenario of a 34x34 matrix with fragments of pixels (marked inside yellow box in c and d) lying outside required area, and **(e)** different scenario where pixels are broken during dicing.

3.4.3. Photolithography with the transparent photomask

Using the Denton EE-4 E-beam evaporator (Denton Vacuum, NJ, USA), chromium (Cr, 15 nm) and gold (Au, 300 nm) were deposited on the top surface of the array (**Figure 3.8)**. Then, a thin film of photoresist (PR) (AZ 5214-E IR, MicroChem Corp.) was spin-coated on the array. The spin coating was conducted at a speed of 3,000 rpm for 60 seconds and then baked at 65 degrees Celsius for 10 minutes. Afterwards, the array was cooled to room temperature, dosed with UV rays for 10 seconds underneath a Mask Aligner (MJB4, SÜSS MICROTEC SE, Germany), developed in a developer (MIF AZ 726, MicroChem Corp.) for 60 seconds, rinsed with deionized (DI) water, and dried in nitorgen (N_2) gas. Subsequently, the array was wet etched by an Au-etchant first for 120 seconds and then with a Cr-etchant solution for 30 seconds, respectively. The array was then cleaned by the developer solution again for 60 seconds. Following PR-stripping with acetone, IPA, and (DI) water, the final electrode pattern is tested with a multimeter to check continuity on the top surface, which contains 128 traces of electrodes and four-square traces on strips of E-Solder 3022 at the four corners of the array. Finally, the bottom surface was similarly patterned and subjected to a continuity test.

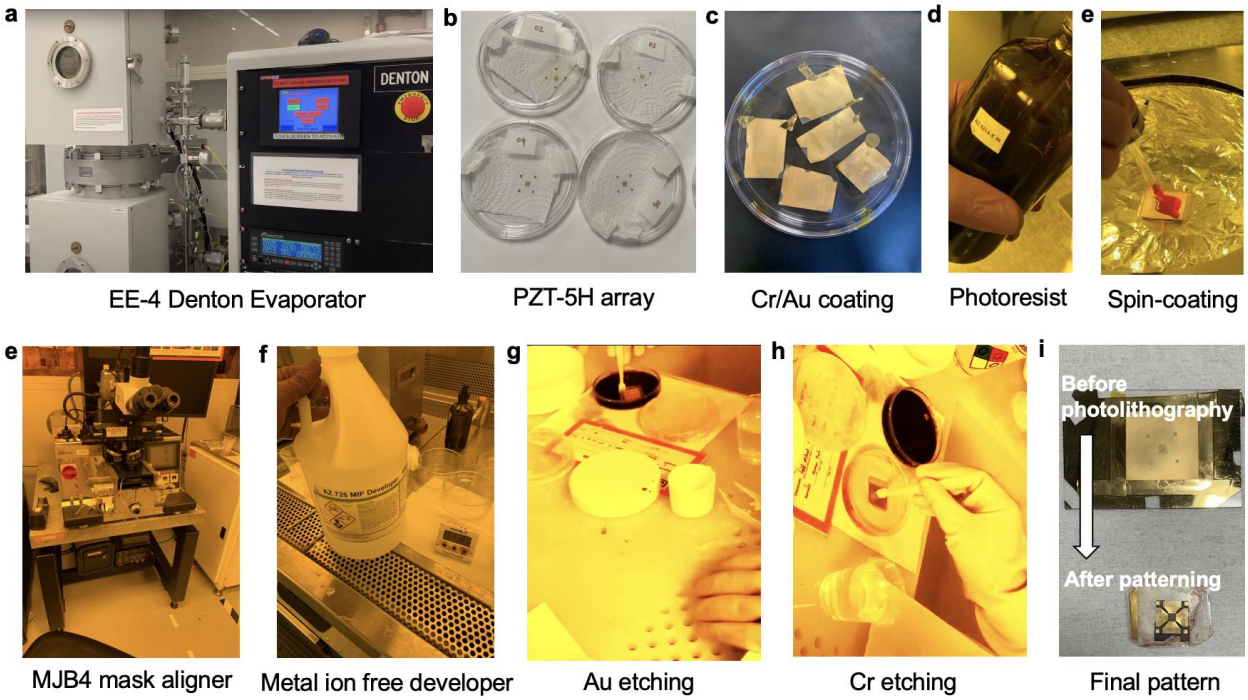

Figure 3.8: An overview of the photolithography process from thin-film coating to wet etching.

The photolithography process for patterning gold traces on the top surface of the array has been illustrated using the representative schematic diagrams as shown in **Figure 3.9.**

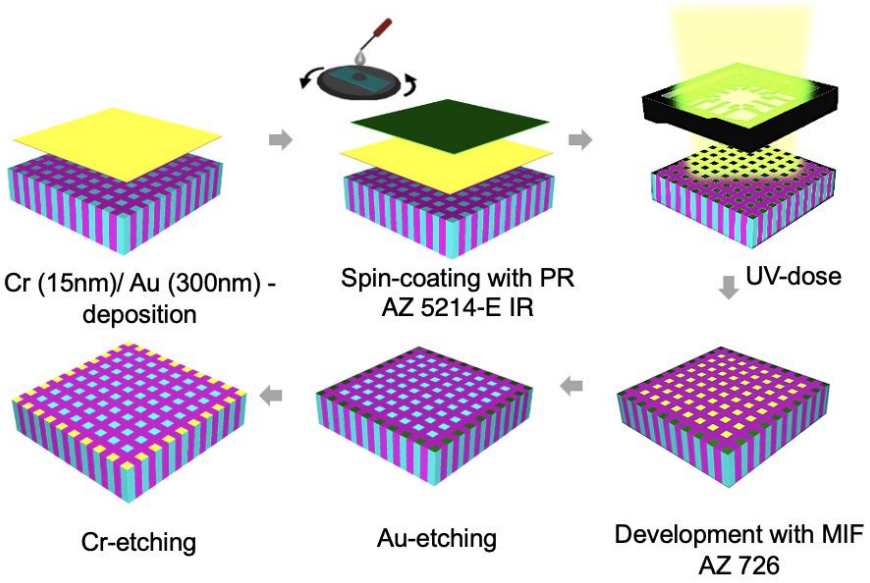

Figure 3.9: Photolithography steps to pattern on the PZT-5H elements at the four edges.

It is essential to ensure that the electrode is only patterned on the edges of the array, so that only 128 square pixels (32 pixels from each side) are used to transmit and receive the spherical waves required for three-dimensional beam profile. Due to the additional rectangular pixels (pixels that are 195 μm long) outside the perimeter of the 34x34 matrix, this is not feasible. Consequently, the thin film Au trace will coat the rectangular pixel in addition to the square pixel during top electrode patterning (as shown in **Figure 3.10a**). As a result, the rectangular pixels will also vibrate while the square pixels are electrically stimulated as they are connected together, resulting in the transmission of waves that are in between a spherical wave and a cylindrical wave. In general, the longer an element is, the more focused the acoustic waves become, concentrating more and more into a single plane. Therefore, the array will behave more like a 1D than a 2D array. To avoid this phenomenon, the footprint of the bottom electrode was restricted to the area inhabited by the 34x34 matrix (as depicted in **Figure 3.10b-c**). Since each pixel is independent and separated by kerfs filled with epoxy resin, only the square pixels at the edge of the 34x34 matrix will be stimulated during transmission, as they are the only ones electroded with Au thin film on both the top and bottom, as opposed to the rectangular pixels, which lack a bottom electrode.

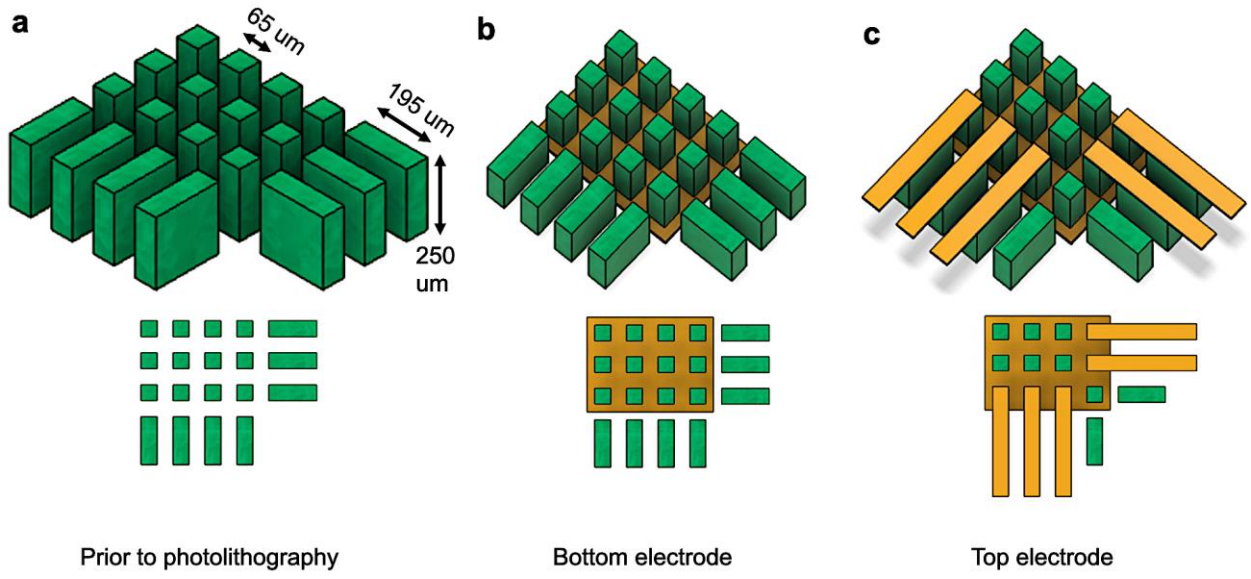

Figure 3.10: Schematic of the micromachined PZT-5H wafer employed in this work, where the bottom electrode only covers the square pixels as opposed to the rectangular pixels, which lack a bottom electrode to ensure spherical waves are transmitted from the stimulated square pixels.

3.4.4. Fabrication of the acoustic matching (ML) and backing layer (BL)

The acoustic matching and backing layers were mixed using a centrifuge (Eppendorf 5810, USA) at 1:4 ratio **(Table 5).** The thickness of the matching layers was maintained at a quarter wavelength, whereas the thickness of the backing layer was around seven times the wavelength.

Table 5: Parameters of acoustic materials used for the 7.5 MHz ultrasound phased array.

Layer	Materials	Sound velocity (c, m/s)[#]	Density (ρ, kg/m^3)[#]	Acoustic impedance (ρc, MRayls)[#]	Wave length (μm)	Layer thickness (μm)
ML	Epoxy 301/ZrO2 (1:4)	2790	3160	8.82	372	93
BL	Epoxy 301/Tungsten (1:4)	1590	4650	7.40	212	1500

[#] **(Zhang et al. 2022)**

The fabrication steps are synopsized in **Figure 3.11**. Once the materials for matching and backing materials were mixed using the centrifuge, they were cured for 2 hr at 65°C.

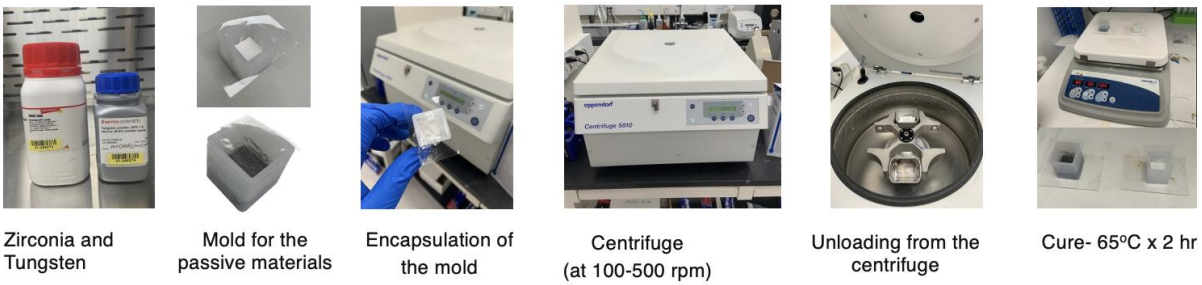

Figure 3.11: Fabrication steps of the acoustic matching and backing layer using a centrifuge.

Figure 3.12 illustrates the schematic of the 2D phased array with and exploded view of a single pixel, demonstrating how the active and passive layers are stacked. As shown in illustration, the array was sandwiched/clamped between the top matching and bottom backing layer. The application of a thin layer of EPO-TEK 301 was performed on the array in order to facilitate the bonding process between the matching and backing layers. In order to administer the thin coating

of polymer, a biocompatible silicone rubber (Ecoflex 00-30, Smooth-On) was employed. Four pieces of E-Solder 3022 were used in four corners to connect the ground electrodes from the top surface or face side of the array.

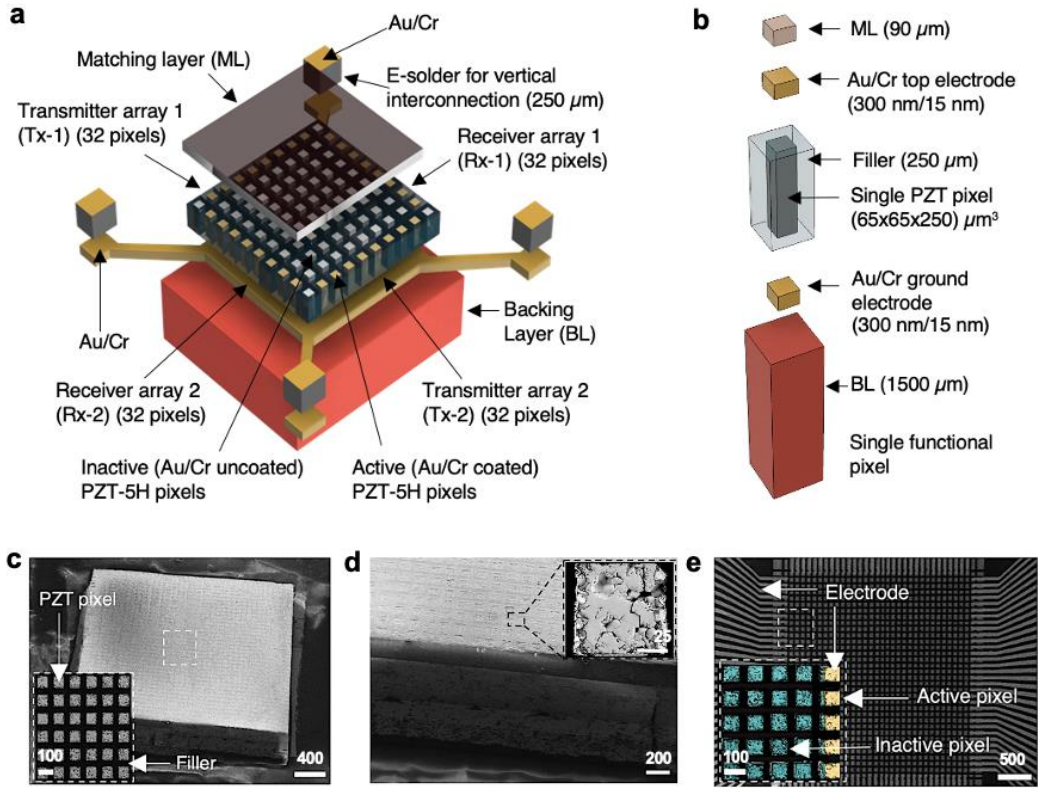

Figure 3.12: Schematic diagram exhibiting the exploded view of the (a) 2D array and a (b) single pixel with corresponding SEM images of the (c) 2D array, (d) single pixel (inset), and (e) electrode pattern on the 2D array prior to the integration of acoustic matching layer (scale bae unit: μm).

3.4.5. Connecting the clamped transducer with flex PCB cable

For the clamped transducer, a flex PCB (printed circuit board) cable with a pitch of 250 μm (trace: μm; kerf: 100 μm) was employed to connect the transducer array with a PCB. Due to the mismatch of constituent materials, strong adhesion between the PCB cable and the PZT array is always a challenge. The addition of conductive resin may cause a short circuit between adjacent pixels. Hence, an anisotropic Z-axis conductive tape, 3M 9703 was used as per the user manual to bond the array with the PCB cable under a microscope for proper alignment.

3.5.Characterization of the transducer array

3.5.1. Surface morphology and topography of the array: Porosity (%) and roughness

The aim of the surface characterization study was to examine the surface profile of piezo pixels following the lapping process. Piezoresponse force microscopy (PFM) can be employed to assess piezoelectric coefficients, provided that the surface is uniform and relatively smooth. During the fabrication of bulk ceramic-based transducers, surface roughness and unwanted porosity could be caused the by friction between the large abrasive particles on the lapping pads and the surface of the fragile PZT ceramics. These abrasive particles are forced at the point of contact as the lapping pads are moved across the PZT surface. Because of the hard lapping grits or aggressive lapping pressure, the result can often cause mechanical damage or cracks to the PZT pixels. As lapping uses harsh abrasives to create a rough surface, subsequent polishing was employed to provide a smooth, mirror-like finish, which was accompanied with relatively finer abrasive grits. Such a finish also ensures ease of mask alignment during the photolithography process. Hence, the surface of the PZT-pixels was analyzed by studying the surface porosity and surface roughness.

According to existing literature, ceramics are analyzed for porosity using their scanning electron microscopy (SEM) images **(Scheithauer et al. 2017)** and there is a strong correlation between porosity and mechanical strength; for example, the mechanical strength and hardness of zirconia ceramics decreases from 342.8 to 43.1 MPa and from 1130 to 303 Hv, respectively, for porosities ranging from 8 to 40.1% **(Fregeac et al. 2019)**. However, the primary objective to study surface porosity introduced in this study is to gain insights into the surface profile before PFM could be conducted. This image analysis process involves converting the SEM images into binary images using ImageJ, an open-source Java-based image processing program software developed by the National Institutes of Health (NIH), USA. In this process, all pores are represented as black or colored pixels, while ceramic particles are represented as white pixels. In the present investigation, this software was also utilized to perform a comparable quantitative analysis by comparing the quantities of black and white pixels. Hence, the first step to analyze the surface porosity involved collecting images of the array surface using a scanning electron microscope (SEM) (Zeiss Ultra Plus, Germany) (**Figure 3.13a)**. Subsequently, ImageJ was utilized to analyze the SEM pictures

in order to discover the difference in surface porosity of the piezo-pixels throughout the transducer array. As seen in **Figure 3.13b**, the porous regions colored in red was identified through image thresholding in order to approximately calculate the porosity (%).

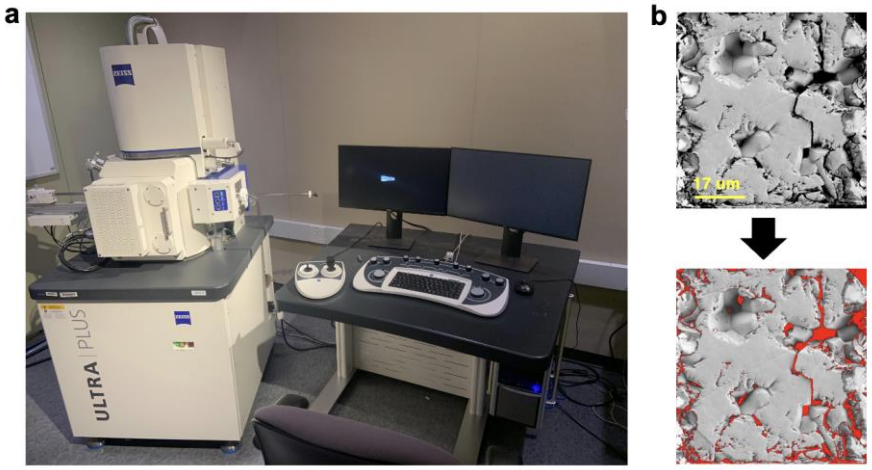

Figure 3.13: Studying the sscanning electron micrographs of PZT pixels using **(a)** Zeiss Ultra Plus and surface porosity from the SEM images using **(b)** the ImageJ.

Atomic force microscope (AFM) has the capacity to quantitatively assess surface roughness and topography due to its capability to scan the X, Y, and Z directions with nanoscale resolution. In the current work, a Jupiter AFM (Asylum Research, CA, USA) **(Figure 3.14 (a-b)),** was used to measure the surface roughness of the finely polished PZT pixels using non-conducting AFM probes **(Figure 3.14c)**. The probes operated at the non-contact mode.

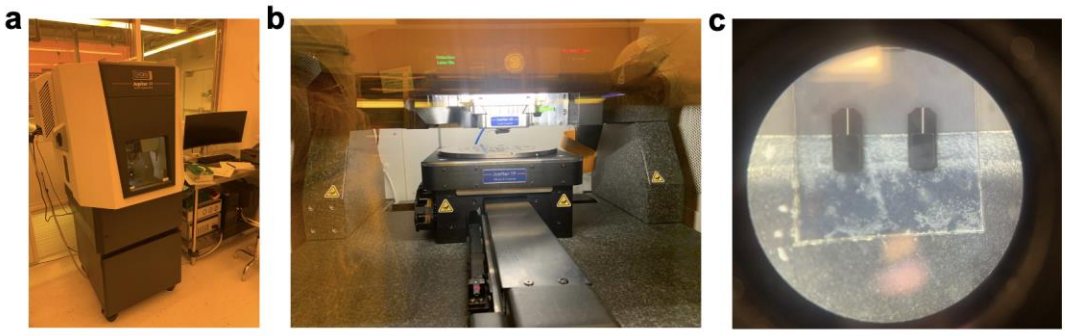

Figure 3.14: Studying the surface roughness and topography of PZT pixels using atomic force microscope: **(a)** Jupiter AFM, **(b)** sample loading area, and **(c)** AFM non-conducting cantilever probes.

3.5.2. Electrical characterization

3.5.2.1.Electrical impedance and k-factor calculation

A KEYSIGHT E4990A impedance analyzer (**Figure 3.15a)** was used to measure the phase-impedance of the transducer arrays. Since the KEYSIGHT Kelvin/Alligator unis were not capable of measuring impedance of transducer beyond 4 MHz, a custom-made probe (**Figure 3.15b-c)** was made by the research team of our lab that was capable of measuring impedance for transducers with an operating frequency up to 20 MHz.

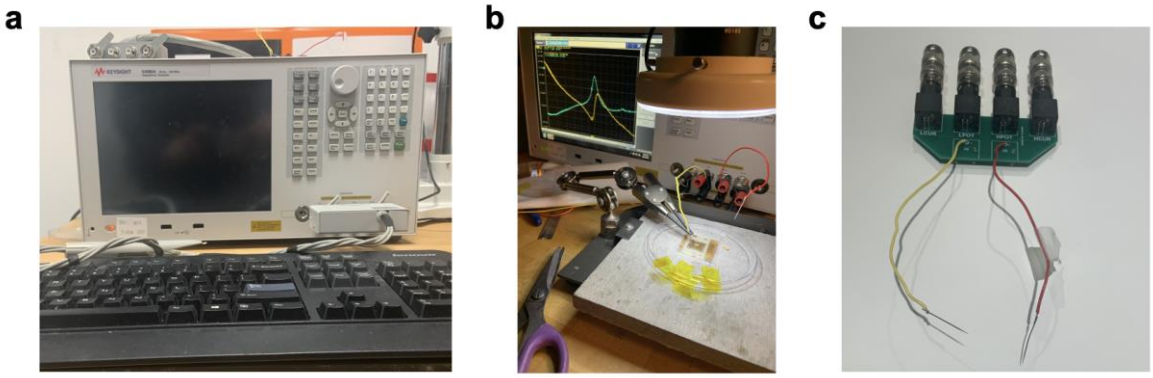

Figure 3.15: A **(a)** KEYSIGHT E4990A impedance analyzer and custom-made probes **(b-c)** for measuring impedance-phase spectrum of high frequency transducer.

From the obtained phase-impedance spectrum, resonance and anti-resonance frequency of the transducers were measured, which was used to calculate the longitudinal mode coupling coefficient or factor (k_{33}-factor) using the following equation **Eqn. 32):**

$$k_{33} = \sqrt{\frac{\pi}{2} \cdot \frac{f_r}{f_a} \cdot \tan\left(\frac{\pi}{2} \cdot \frac{f_a - f_r}{f_a}\right)} \quad (\mathbf{Eqn.\,32})$$

3.5.2.2.Cross-talk characterization

When two ultrasound sensors in close proximity receive one other's signal, this phenomenon is known as cross talk. In this work, the inter-element cross-talk of the transducer array was evaluated and the test set-up is shown in **Figure 3.16b**. During transmission, a stimulating oscilloscope probe (Pico Technology, UK) that was coupled to a KEITHLEY 3390 50 MHz function generator (Tektronix Inc., OR, USA) was used to excite just a single transducer of the transmitter array at a voltage of 1 Vpp. Simultaneously, in reception, the nearest neighbouring transducers from the receiver array were enabled to receive signals **Figure 3.16**. The receiver transducer was wired up to a separate recording oscilloscope probe connected to a Picoscope (5000 series, Pico Technology, UK) so that the received signal could be recorded during the transmission phase.

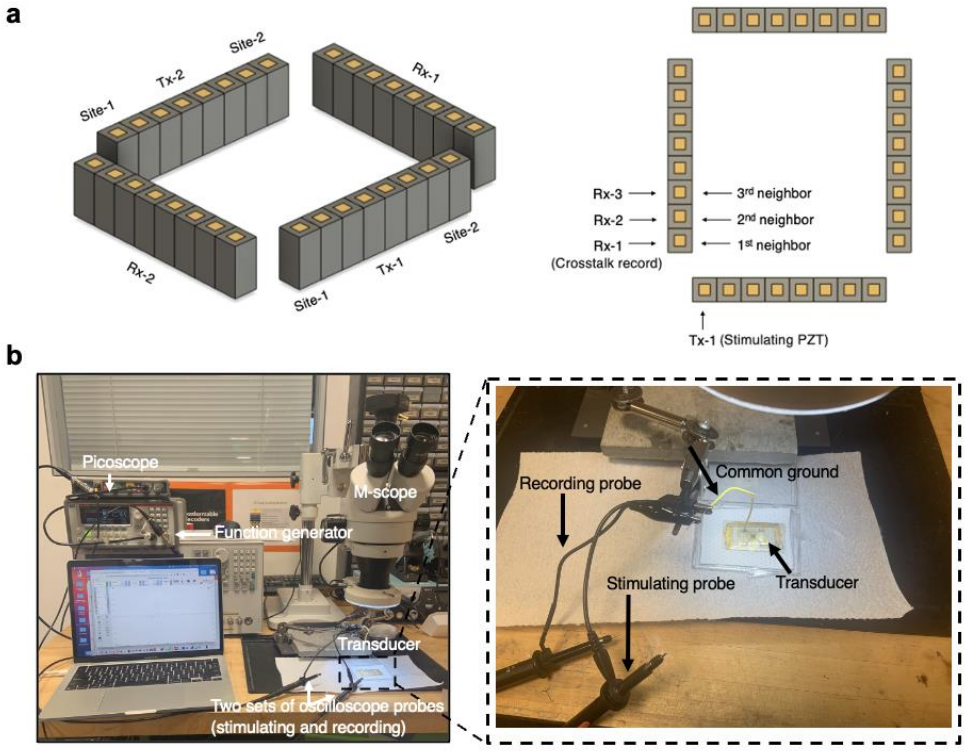

Figure 3.16: Test to characterize the cross-talk of the transducer array: (a) schematic diagram outlining a representative diagram of transmitter and receiver channels of the transducer array, (b) test set-up to stimulate/record the cross-talk using function generator, probe, and Picoscope.

3.5.3. Acoustic characterization

3.5.3.1.Acoustic bandwidth (BW%) measurement

An ONDA HNC-0400 needle hydrophone (ONDA corporation, CA, USA) was used to characterize a single acoustic pulse or a series of identical pulses generated by the transducer array) (**Figure 3.17)**. The transducer array was set up on an acoustic damper and put in a DI water container with the matching layer facing the hydrophone. The amplifier-connected hydrophone was situated 1 cm from the transducer. By using the function generator, the transducer array was excited at 10 Vpp, and the resultant acoustic pressure waveform response was recorded by the needle hydrophone connected to the Picoscope. The exciting waveform produced by the generator is a tone burst of a 4-cycle sine wave at a center frequency of 7.5 MHz with a 1 ms burst period. The frequency spectrum of this pressure waveform was derived using the OriginLab-integrated fast Fourier transform (FFT) algorithm. Using the observed frequency spectrum, the center frequency (fc) and 6 dB bandwidth (BW) of the ultrasonic transducer were calculated using the following equations **(Eqns. 33-35).**

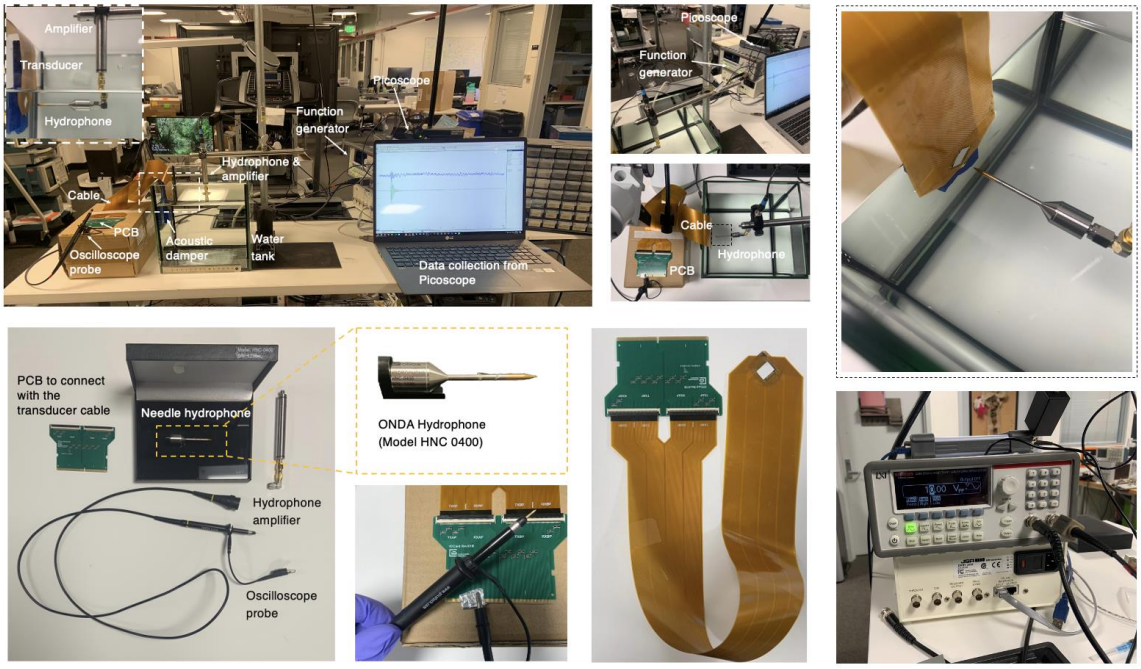

Figure 3.17: Experimental set-up with the ONDA needle hydrophone for acoustic characterization of the high-frequency 7.5 MHz transducer array.

$$f_c = {(f_1 + f_2)}/{2} \quad (\mathbf{Eqn.\,33})$$

$$\text{Band width (BW)} = f_2 - f_1 \quad (\mathbf{Eqn.\,34})$$

$$\text{BW (\%)} = {(f_2 - f_1)}/{f_c} \quad (\mathbf{Eqn.\,35})$$

3.5.3.2.Quality factor (Q-factor) measurement

Low-Q ultrasonic transducers are also referred to as "broadband transducers, which is required in imaging transducers **(C.-M. Chen and Choubey 2018)**. Q-factor or the “quality factor” specifies the frequency range that causes ceramic element ringing when power is transmitted through the transducer. Hence, the Q-factor of a transducer describes its sensitivity to variations in driving frequency. The Q-factor is simply measured from the ratio of center frequency and bandwidth **(Eqn. 36)**. As the Q value is decreased, the bandwidth expands, but the pulse length shortens. For sharp resolution in ultrasonic imaging, the transducer must transmit a very short pulse. As a result, a low Q is required for the transducer array to ensure a broad band width. It is possible to alter the Q factor of piezoelectric materials by introducing mechanical dampening using a backing layer, which serves to lessen the oscillation. A system with a high Q is one that is used for resonant; a crystal watch for instance, or in high intensity focused ultrasound (HIFU) to send burst of multiple cycles of waves to create mechanical/thermal effects like moving/destroying kidney stone **(C.-M. Chen and Choubey 2018).**

$$Q_{\text{factor}} = {f_c}/{BW} \quad (\mathbf{Eqn.\,36})$$

3.5.3.3.Acoustic pressure measurement using ONDA needle hydrophone

Once power is applied to the transducer from the external function generator, the transducer under test exerts a force proportionate to its emitted sonic energy. The needle hydrophone measures this force in an electronic or voltage scale (V). Using the data sheet of the ONDA hydrophone, the

following formula **(Eqn. 37)** was used to convert the voltage (V) received by the hydrophone into equivalent acoustic pressure (Pa) at 7.5 MHz:

$$\text{Acoustic pressure (Pa)} = \frac{\text{Recorded voltage by hydrophone (mV)}}{7.3 \text{ x } 10^{-5} \text{ (mV)}} \quad (\mathbf{Eqn.37})$$

3.5.4. Long-term thermal stability test

Two sources contribute to the thermal effects of ultrasound: (i) the heating of tissue through ultrasonic absorption, and the (ii) self-heating of transducer's due to inefficient energy transmission **(Killingback et al. 2008)**. The self-heating of transducers has recently been proven to be a major factor in the localized increase in tissue temperature and the largest heating occur at the interface between tissue and the transducer when the transducers are operated for a long period of time at high power **(Calvert et al. 2007; Saunders, Clift, and Duck 2004)**. A recent review work discussed the thermal effects and safety concerns of medical ultrasound transducer in depth **(Nowicki 2020).** Hence, developing a transducer ensuring thermal stability for long-term use is significant to avoid tissue injury.

The records of skin temperature under clothing have shown the regional variation of the human skin temperature and the accepted skin temperature ranges between 32ºC and 35ºC **(Benedict, Miles, and Johnson 1919)**. Nevertheless, prolonged exposure to 45°C can lead to 2nd and 3rd degree burns, whereas the burning pain threshold is at 43°C **(Shuvo et al. 2021)**. Hence, ensuring the surface temperature of the transducer withing the safety threshold is significant. To observe the long-term thermal stability test of the transducer array in air, the array was subjected to power (driving frequency= 7.5 MHz, voltage= 10Vpp, burst period= 10 ms (100 Hz), sin cycle= 01) generated by a 50MHz waveform generator (KEITHLEY 3390, USA). The resultant temperature profile was recorded using a FLIR compact thermal camera (C3-X, Teledyne FLIR LLC, US) (**Figure 3.18)**. The test was conducted for both the unclamped (i.e., without the matching and backing layer) and clamped (i.e., with matching and backing layer) state. An oscilloscope probe was employed to transmit the power from the waveform generator. For unclamped transducer, the probe ends were directly placed on top of the ground electrode connecting the E-solder and the

electrode connecting a single PZT pixel. Since the probe head is larger than the size of a PZT pixel and placing the probe on top of the pixel may damage the PZT, the probe was connected to the electrodes instead. For the clamped transducer, a flex PCB cable was employed to connect the array with a PCB. Next, the oscilloscope probe was connected to the PCB to transmit the power to a single pixel and the thermal camera was used to record the temperature profile.

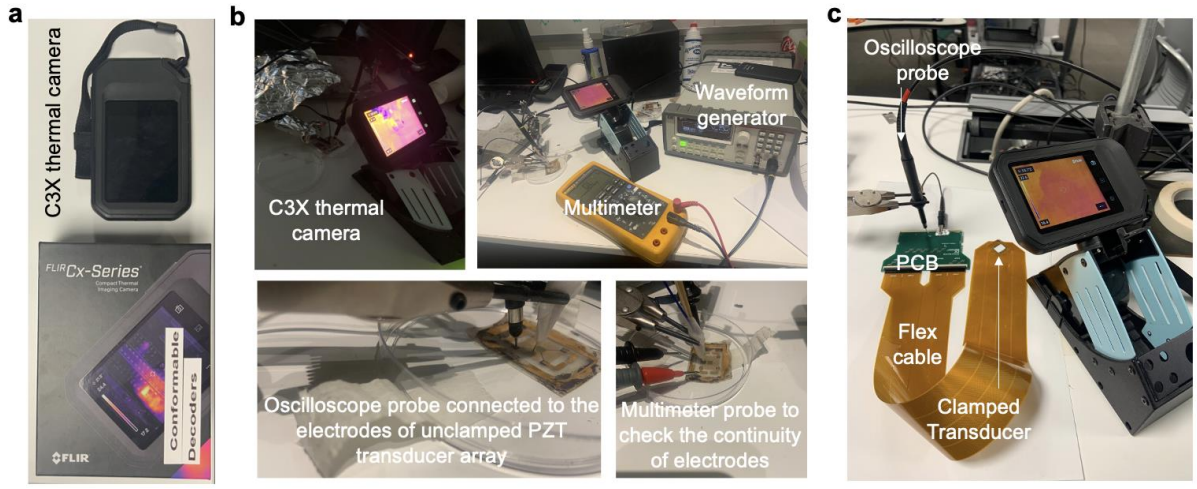

Figure 3.18: FLIR C3-X compact thermal camera (a) used with KEITHLEY 3390 50MHz (b) for thermal stability test of the unclamped and clamped (c) PZT transducer array.

3.6.Transducer modelling

3.6.1. Impedance and bandwidth simulation using 1D KLM model

PiezoCAD (Sonic Concepts™, USA) was used to employ KLM model to simulate and optimize the transducer design. The specification of the PZT-5H used in building the physical transducer was used as input parameters in PiezoCAD along with its built-in feature. Also, the material properties recorded in **Table 4** for the matching and backing layers were used in the PiezoCAD beside the ones listed in its built-in library. **Figure 3.19 (a-b)** displays the simulated impedance-phase frequency spectrum of the unclamped array and bandwidth (-6 dB) of the finished transducer device along with its central frequency. The utilization of the software is relatively uncomplicated. The software was unable to produce any schematic or visual representation of the array geometry utilized in constructing this model. Instead, it relied solely on manual input of design parameters derived from the data table and built-in library. However, all the features of PiezoCAD were not available in the Windows (operating system) version used in the current work. Hence, to assess the axial acoustic pressure, finite element models were built that discussed in the next section. It is important to acknowledge that researchers commonly employ pulse-echo testing with an X-cut quartz as the signal reflecting target when calculating bandwidth through experimental methods in a water tank. Consequently, the "Pulse-Echo (Two-way) Impulse Response" option could be selected in the PiezoCAD software for such experimental set-ups. However, in the present investigation, the compact area of a piezo-pixel and the absence of amplifier circuitry resulted in insufficient strength of the output signal generated by a single pixel to facilitate the collection of an echo. Consequently, a needle hydrophone was employed in this study to capture the output signal produced by individual pixels. Therefore, it is necessary to select the "Receive Impulse Response" option in PiezoCAD in order to obtain accurate simulation results.

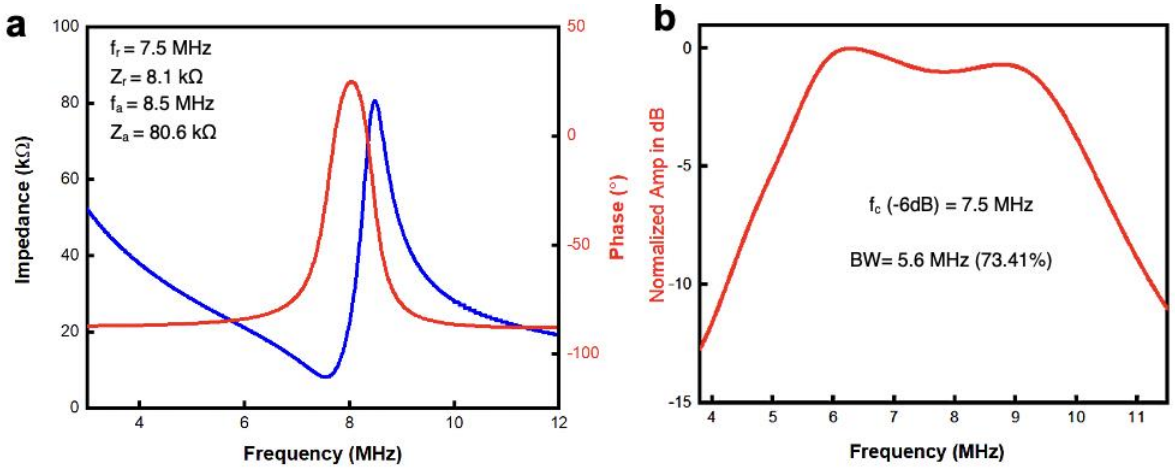

Figure 3.19: KLM modelling to simulate the **(a)** impedance-spectrum of the PZT array at 7.5 MHz and **(b)** resultant bandwidth when tested with the passive layers.

3.6.2. Finite element analysis (FEA) for modelling acoustic pressure

COMSOL Multiphysics® 6.0 (COMSOL Inc., Sweden) simulator could be used for finite element analysis (FEA) or modelling the transducer to predict their acoustic pressure. Here, FEA method was applied at the resonance frequency of the transducer, which was 7.5 MHz. The material property recorded in **Table 4** was used as the input parameters in COMSOL 6.0 beside the ones listed in its built-in library. The resultant 3D symmetric model exhibits the sound pressure level (SPL) (dB) **(Figure 3.20)** and acoustic pressure (Pa) **(Figure 3.21).** Also, the resultant acoustic pressure distribution radiating from the transducer surface could be seen with the help of the surface and height plot **(Figure 3.22a)**. The height of the of surface indicates the pressure magnitude. The corresponding point graphs **(Figure 22b-c)** illustrate the SPL and acoustic pressure at different axial distance. **Appendix-I** presents a detailed visual guide that outlines the step-by-step process of constructing a Finite Element Method (FEM) model using the COMSOL 6.0 software platform. The initial stage entails the establishment of the transducer's geometry, as well as the specification of the hemisphere (either for water or air). Next, the pressure acoustics domain was defined as well as the phenomenon of spherical wave radiation. Subsequently, the piezoelectric domain was chosen to represent the solid mechanics characteristic. This was followed by the selection of electrostatics, involving the definition of the applied electrical potential and ground electrode. Finally, the mesh generation was performed prior to populating the study.

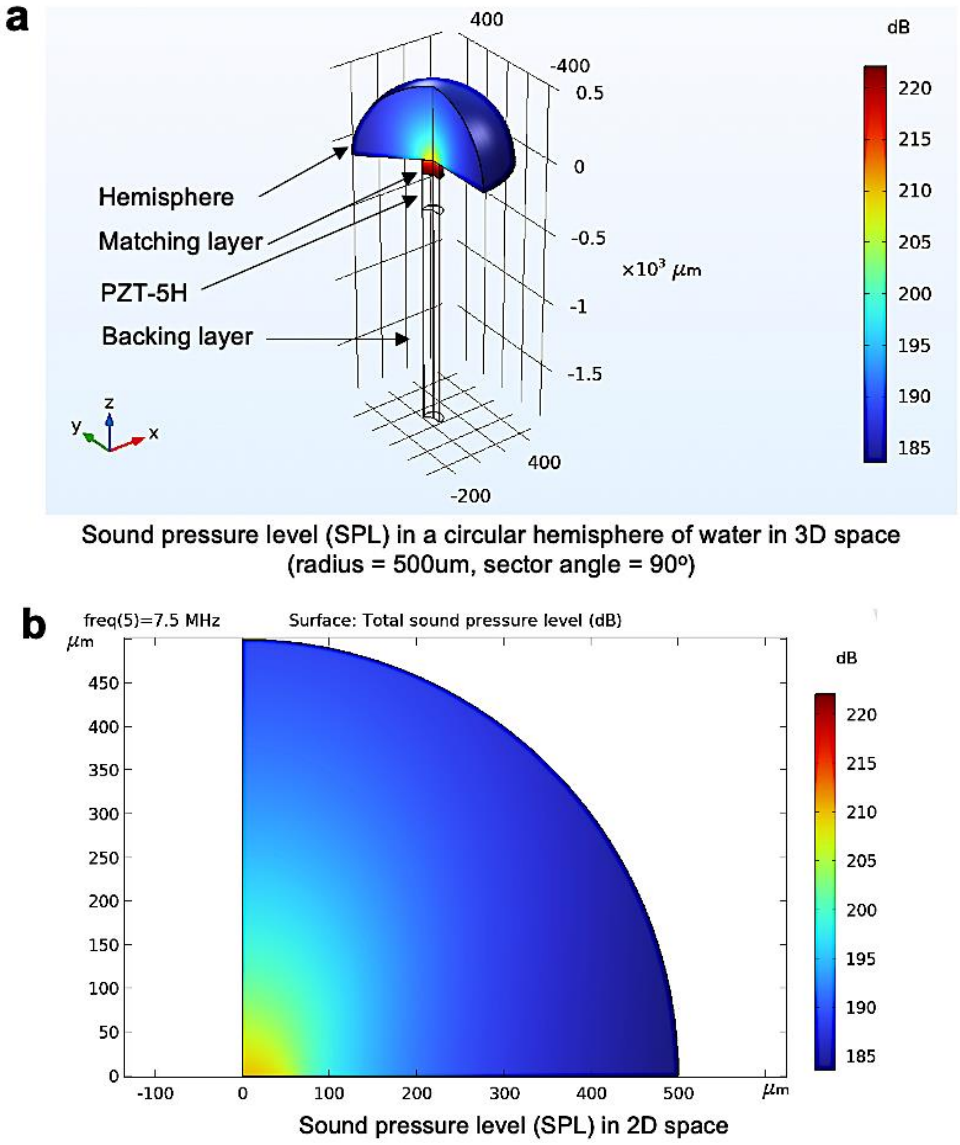

Figure 3.20: FE (finite element) modelling of the sound pressure level (SPL) of the transducer at 7.5 MHz and 10V electric potential using COMSOL Multiphysics® 6.0 within a circular hemisphere of water (radius: 500 μm; sector angle: 90º).

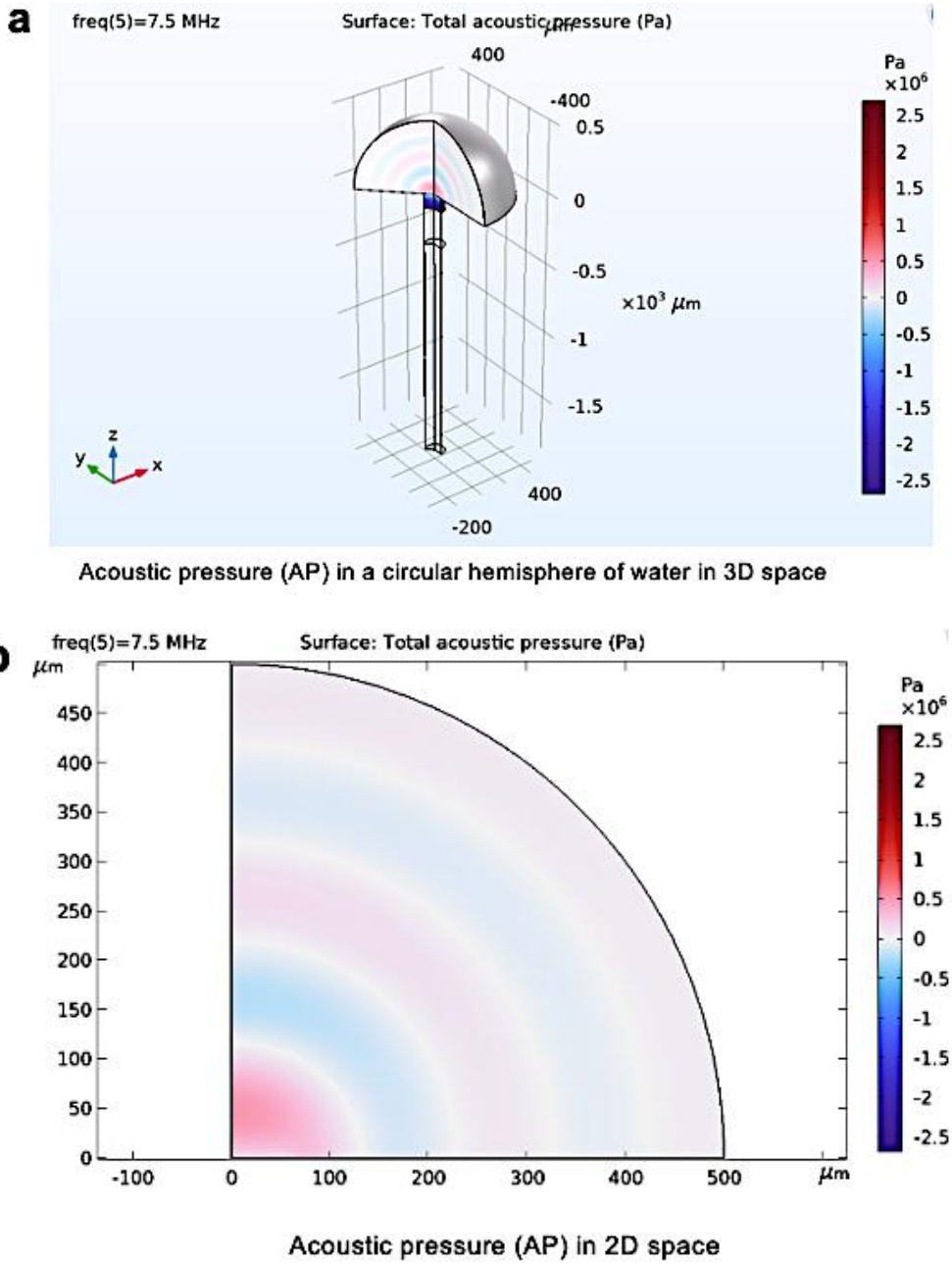

Figure 3.21: FE (finite element) modelling of the acoustic pressure of the transducer at 7.5 MHz and 10V electric potential using COMSOL Multiphysics® 6.0 within a circular hemisphere of water (radius: 500 μm; sector angle: 90°).

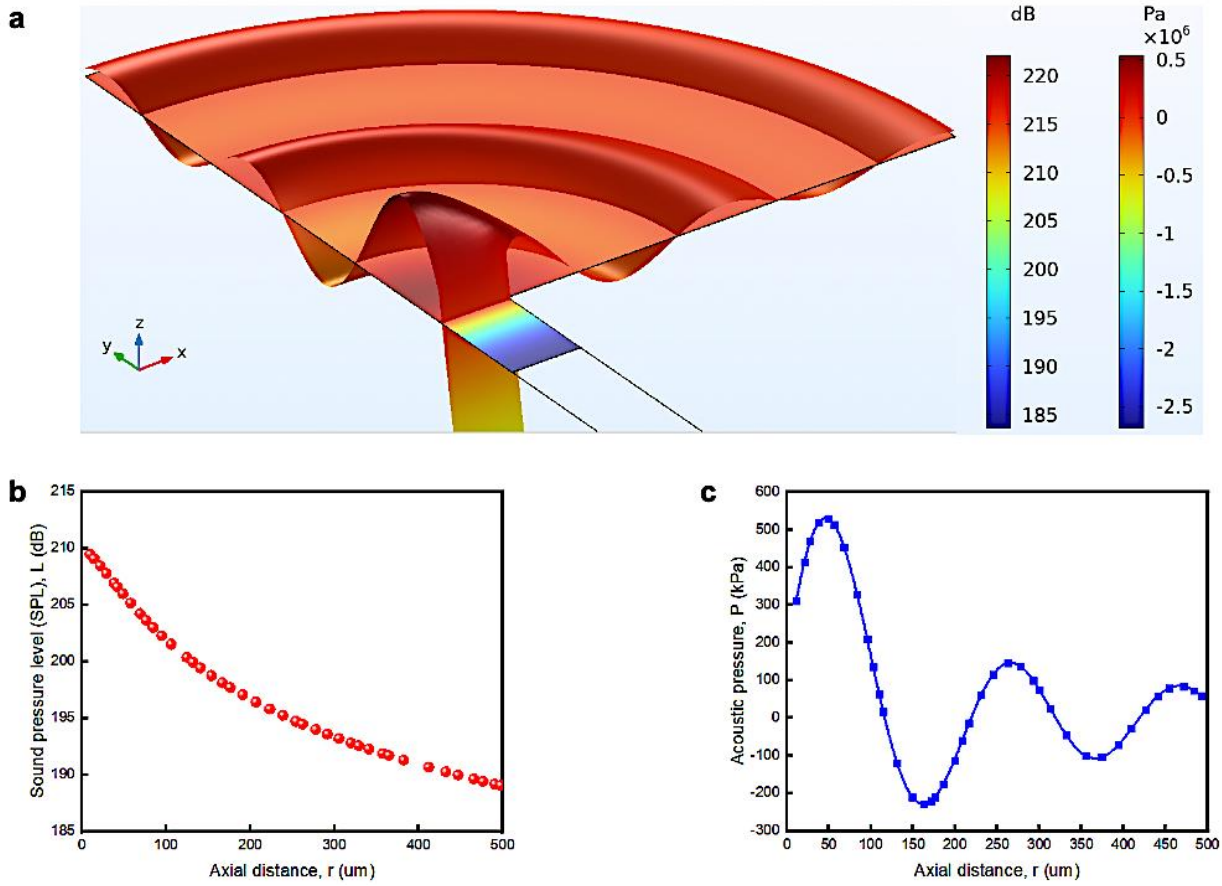

Figure 3.22: FE (finite element) modelling of the 7.5 MHz transducer to represent the pressure distribution: **(a)** surface and height plot to visualize the pressure distribution in 3D space and the corresponding axial **(b)** sound pressure level (SPL) and axial **(c)** acoustic pressure.

Figure 3.22b exhibits the simulated model for the axial SPL. Using simulation results and the following equation (**Eqn. 38)** and a reference pressure value of 1 μPa (or 10^{-6} Pa) for water medium in COMSOL **(COMSOL 2017)** that corresponds to 0 dB, the resultant sound pressure level (SPL) (dB) 1 cm (=10000 μm) away from the transducer was estimated to be 182.6 dB by the distance law below **(Sprague and Luczkovich 2004; Švec and Granqvist 2018).**

$$L_2 = L_1 - \left|20.\log\left({}^{r_1}/_{r_2}\right)\right| \quad (\mathbf{Eqn.\,38})$$

$$\therefore L_2 = L_1 - \left|20.\log\left({}^{r_1}/_{r_2}\right)\right|$$

$$= 209.47\ \text{dB} - \left|20.\log\left({}^{9.56\ \mu\text{m}}/_{10000\ \mu\text{m}}\right)\right|$$

$$= 182.6\ \text{dB}$$

Figure 3.22c exhibits the simulated model for the axial acoustic pressure. Since, the hydrophone is set at 1cm away from the transducer in the acoustic characterization test set-up, the simulation results were used to simulate the predicted acoustic pressure (Pa) at 1cm (=10000 μm) away from the transducer. The theoretical values was estimated to be 2.62 kPa by using the inverse distance law (**Eqn. 39)** for sound pressure **(Hazelwood and Robinson 2007; Sprague and Luczkovich 2004):**

$$P \propto {}^{1}/_{r} \quad (\mathbf{Eqn.39})$$

$$\therefore P_1.r_1 = P_2.r_2$$

$$\Rightarrow P_2 = {}^{(P_1.r_1)}/_{r_1}$$

$$= {}^{(529\ \text{kPa}).(49.24\ \mu\text{m})}/_{(10000\ \mu\text{m})}$$

$$= 2.62\ \text{kPa}$$

Chapter 4

4. Results and discussion

In this chapter, the surface morphology, electric, acoustic, and long-term thermal performance of the transducer will be discussed.

4.1.Surface porosity and roughness for consistency of volumetric geometry

When working with a single pixel of 65x65x250 μm^3 for a single transducer channel, as in the current study, it is not easy to make sure the volumetric geometry is the same. This is done with precise lapping to keep the structure intact and make sure the surface is flat. Since TX/RX (transmitter-receiver) pixels are close to the edge, they are more likely to be affected by overlapping, aggressive lapping, or mechanical pressure. Variations in lapping duration, pressure, and relative acceleration between the lapping surface and the workpiece would have an impact on the rate of material removal and the quality of the grind. As demonstrated in **Figure 4.1(a-b)**, the pixels might be fully pulled out of the array in the worst-case scenario. This work is thus heavily focused on the challenge of regulating the rate at which material is removed from the array by abrasive lapping, which was ensured by visually inspecting the array surface under a microscope and its thickness after every 30 seconds to preclude excessive grinding to ensure the required geometry is maintained during the lapping. SEM images were used to study the surface morphology of the array elements at a microscopic level. This was done because it is important for the quality of the ultrasound imaging to have a consistent array performance, which is done by making sure the geometry of the array elements is the same everywhere and ensure successful electrode patterning on top of all the 128 pixels **(Figure 4.1c)**. There was some variation across the array as shown in the SEM images (**Figure 4.2)** and the surface porosity of the piezo pixels were in between 6% and 10%, but on average the surface porosity of the piezo pixels was about 7% (**Figure 4.3)**. However, the lapping technique assured the structural integrity of the 2D array without any missing pixels, yielding 100%, i.e., all the 128 transducer channels in their entirety.

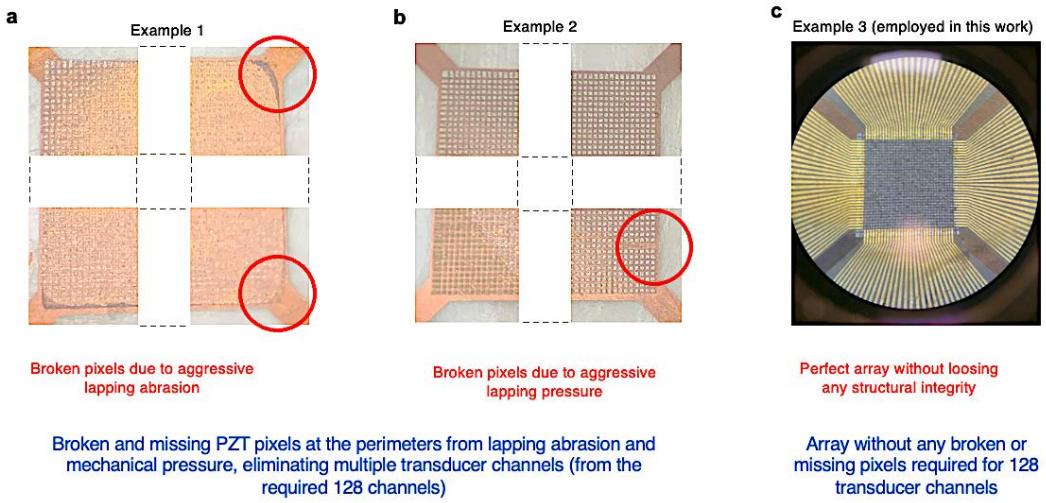

Figure 4.1: Impact of abrasive lapping and controlling it on fabricating transducer array.

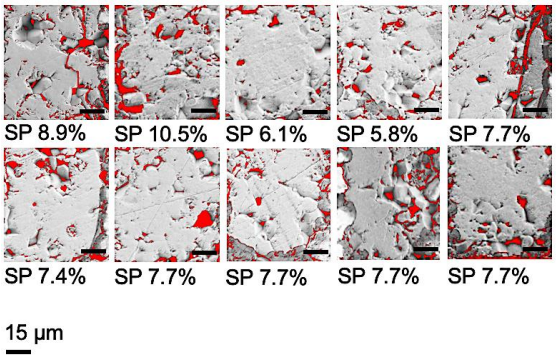

Figure 4.2: SEM images displaying the surface porosity of randomly selected PZT pixels.

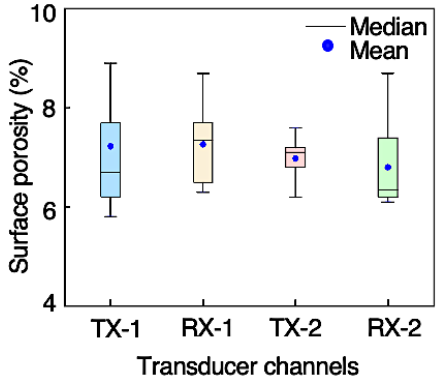

Figure 4.3: Statistical comparison of surface porosity among the transducer channels.

AFM phase imaging was employed to obtain the contrast imaging based on material properties. The cantilever oscillating with a phase at a fixed frequency exhibited a phase shift or difference when the nature of its interaction with the polycrystalline PZT ceramic array changed abruptly,

predominantly due to changes in material and mechanical properties of the sample surface, such as regions of different hardness, viscoelasticity, friction, adhesion, and so on. Changes in the phase change resulting from the cantilever deflection are used to measure the PZT topography by the feedback loop of the AFM control system (**Figure 4.4a)**.

The surface porosity analyzed the characteristic of the device surface. Using AFM, a quantitative measurement of the surface roughness (i.e., measurement of surface finish) and topography was analyzed to develop an understanding of the surface flatness, which may affect the pixel volume. The root mean square (RMS) roughness was about 450.8 nm, 513 nm, and 527.1 nm over a scan area of 5µm x 5µm, 15µm x 15µm (**Figure 4.4b)**, and 25µm x 25µm, respectively.

The objective of surface characterization was to investigate the surface profile of piezo pixels after lapping. If the surface is uniform and relatively smooth, piezoresponse force microscopy (PFM) can be used to evaluate piezoelectric coefficients and observe ferroelectric domains at the micro and nano scales. The principle of piezoelectric force microscopy (PFM) is based on the reverse piezoelectric effect, whereby applying a voltage to a sample through a cantilever probe causes the sample to expand. Using PFM, the mechanical extension of the sample is then quantified. Due to the fact that the contact resonance of the is extremely dependent on the stability of the probe tip-sample contact, a surface with a low roughness is required for the accurate evaluation of the piezo coefficient. It is important to note that the roughness observed in the present study is considerably higher than the roughness (6-9 nm) observed in regular PZT thin film, which can be attributed to the abrasive surface treatment. **(Jeng, Tsai, and Fang 2003)**. As a result, PFM could not be further conducted.

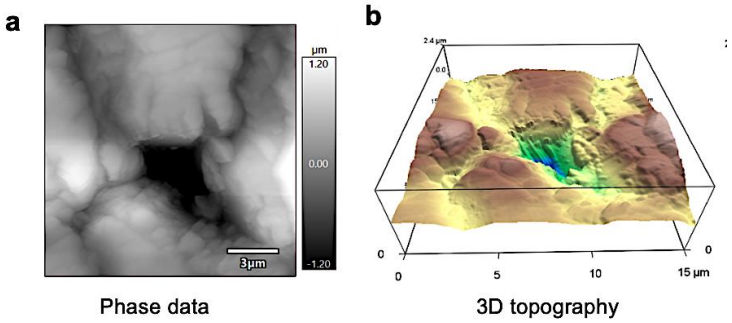

Figure 4.4: AFM images presenting the topography of and array pixel: **(a)** phase data and **(b)** 3D topography.

4.2.Impedance-phase angle, resonance-antiresonance, and k-factor of the array

The impedance-phase spectrum of the 2D PZT-5H array is depicted in **Figure 4.5a**. As depicted in the diagram, the experimental resonance frequency and associated impedance are 7.6 MHz and 10.14 kΩ, which are comparable to the KLM simulation results (7.5 MHz and 8.1 kΩ) shown in Chapter 3. As mentioned earlier, it must be noted that KLM being a 1D model have some limitations. For instance, 1D models disregard the acoustical attenuation coefficient of backing material **(Assaad et al. 1996)**. The 1D models presume that there is no reflection of acoustic impulses transmitted to the backing stratum. In practice, however, supporting layers with a low attenuation factor will reflect waves, potentially interfering with the front-side reverberation. In addition, most 1D models can only model vibration/oscillation in one-dimension **(Chaudhary 2007)**. This limitation of the 1D KLM model may have contributed to the variation between the experimental and simulated anti-resonance frequency and associated impedance. However, overall values of the experimental and simulated results have the same order of magnitude. This result ensures the efficacy of the designed photomask that was used to secure the bottom electrode by covering only the 34x34 square pixels, as described previously. Otherwise, the pixels would have exhibited reduced impedance (2.86 kΩ) (**Figure 4.5b**) at a similar resonance frequency of 7.6 MHz due to the fact that the bottom electrode bridged the square (65 μm x 65 μm) and rectangular (65 μm x195 μm) pixels into a single large rectangular pixel (65 μm x 260 μm) **Figure 4.5b**. We know that resistance (R) is inversely proportional to surface area (A) of a conductor. Applying this formula **(Eqn. 40)** to the square ($A_1.Z_1$) and rectangular ($A_2.Z_2$) pixel, we found that the product of $A_1.Z_1$ (= 65 x 65 x 10.14= 4.28 x 10^4 kΩ-μm^2) and rectangular $A_2.Z_2$ (= 65 x 260 x 2.86= 4.83 x 10^4 kΩ-μm^2) are close and their values have the same order of magnitude. Such a variation was avoided by the custom-made photomask designed in this research work.

$$R \propto {}^{1}/_{A} \quad (\mathbf{Eqn.40})$$

$$\therefore {}^{R_1}/_{R_2} = {}^{A_2}/_{A_1}$$

$$\Rightarrow R_1.A_1 = R_2.A_2$$

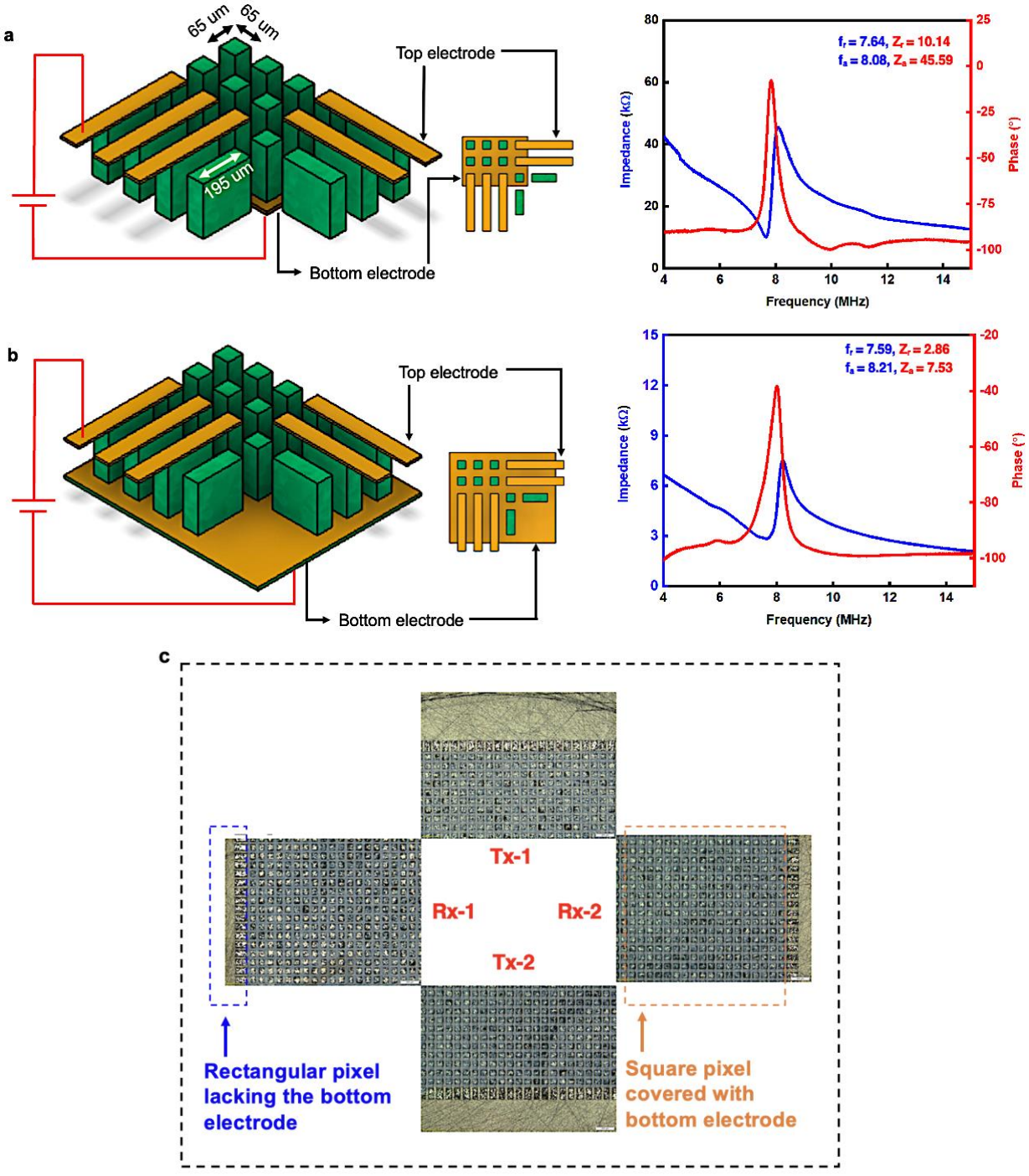

Figure 4.5: Impedance-phase angle spectrum of the transducer: **(a)** functional square pixel (area, A_1= 65 x 65 μm^2), **(b)** functional rectangular pixel (area, A_2= 65 x 260 μm^2), and **(c)** photo of the functional area comprising only square pixels isolated from the rectangular pixels.

Figure 4.6 (a-d) illustrates the resultant resonance (f_r) and anti-resonance (f_a) frequency of all the 128 transducer channels of the 2D phased sparse array, i.e., each of the 32 channels for the transmitter -1 (T_X-1), transmitter -2 (T_X-2), receiver-1 (R_X-1), and receiver-2 (R_X-2) arrays. Although there was a slight variation among the channels, the f_r and f_a were roughly around 7.5 and 8 MHz for the transmitter and receiver arrays. The highest and lowest f_r were 8 MHz and 7 MHz, respectively. For f_r, the maximum and minimum values were 8.7 MHz and 7.7 MHz, respectively. The volumetric variation of the pixel geometry that resulted from the abrasive lapping could have accounted for some of these minor variations observed.

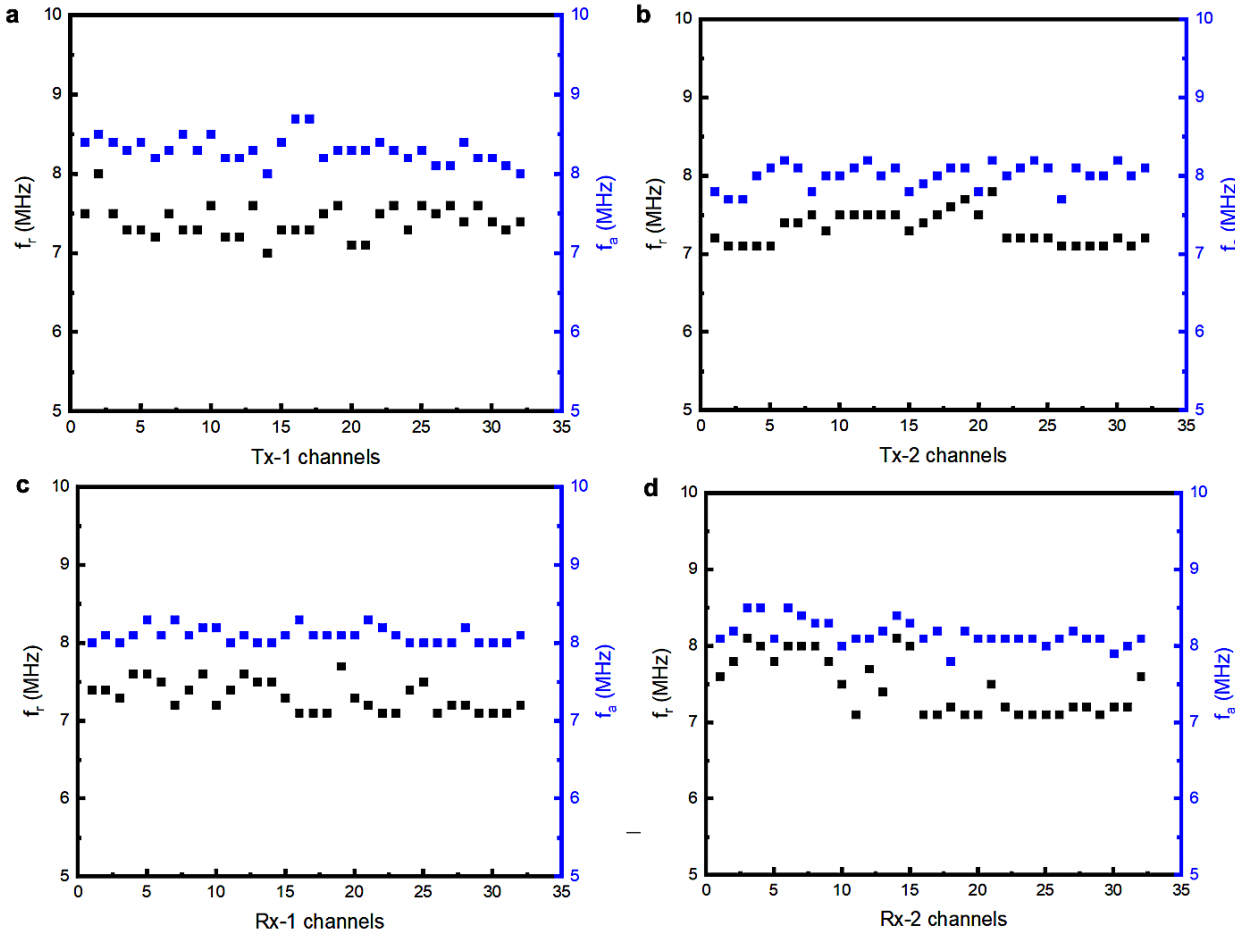

Figure 4.6: Resonance-antiresonance behaviour of the transducer array: **(a)** transmitter -1 (T_X-1), **(b)** transmitter -2 (T_X-2), **(c)** receiver-1 (R_X-1), **(d)** receiver-2 (R_X-2),

As shown in **Figure 4.7**, majority of the transducer channels demonstrated a longitudinal k_{33}-factor around 0.45-0.5, with slight fluctuation, probably due to the variations in the volumetric geometries of the pixels arising from the variation in surface porosity or roughness across the array.

The mean resonance, anti-resonance, and the longitudinal mode k_{33}-factor were 7.4 (± 0.26) MHz, 8.1 (± 0.18) MHz, and 0.45 (± 0.07), respectively.

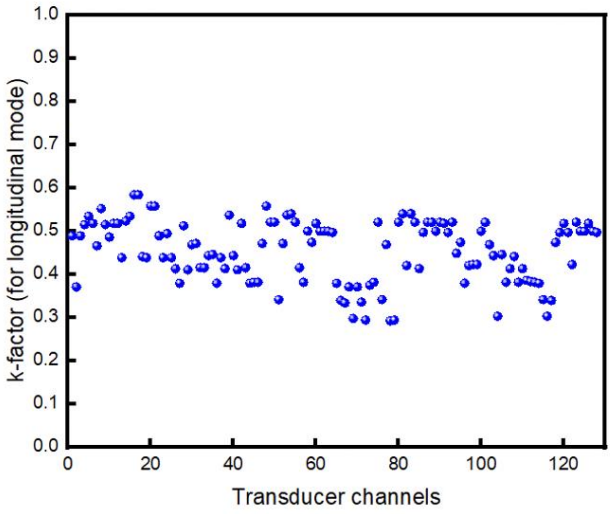

Figure 4.7: Longitudinal mode k-factor of all the 128 transducer channels.

4.3.Bandwidth, central frequency, and Q-factor

As shown in **Figure 4.8 (a-d)**, the experimental bandwidth (BW= 6.25-6.4 MHz, BW%= 79.1-84.21%) and central frequency (f_c= 7.6-7.9 MHz) is similar to the ones obtained from simulated results (f_c= 7.5 MHz, BW= 5.6 MHz, BW%= 73.41%) produced by the 1D KLM model. However, the experimental values acquired demonstrate that the fabricated transducer has superior bandwidth performance compared to the simulated transducer design optimized for medical imaging.

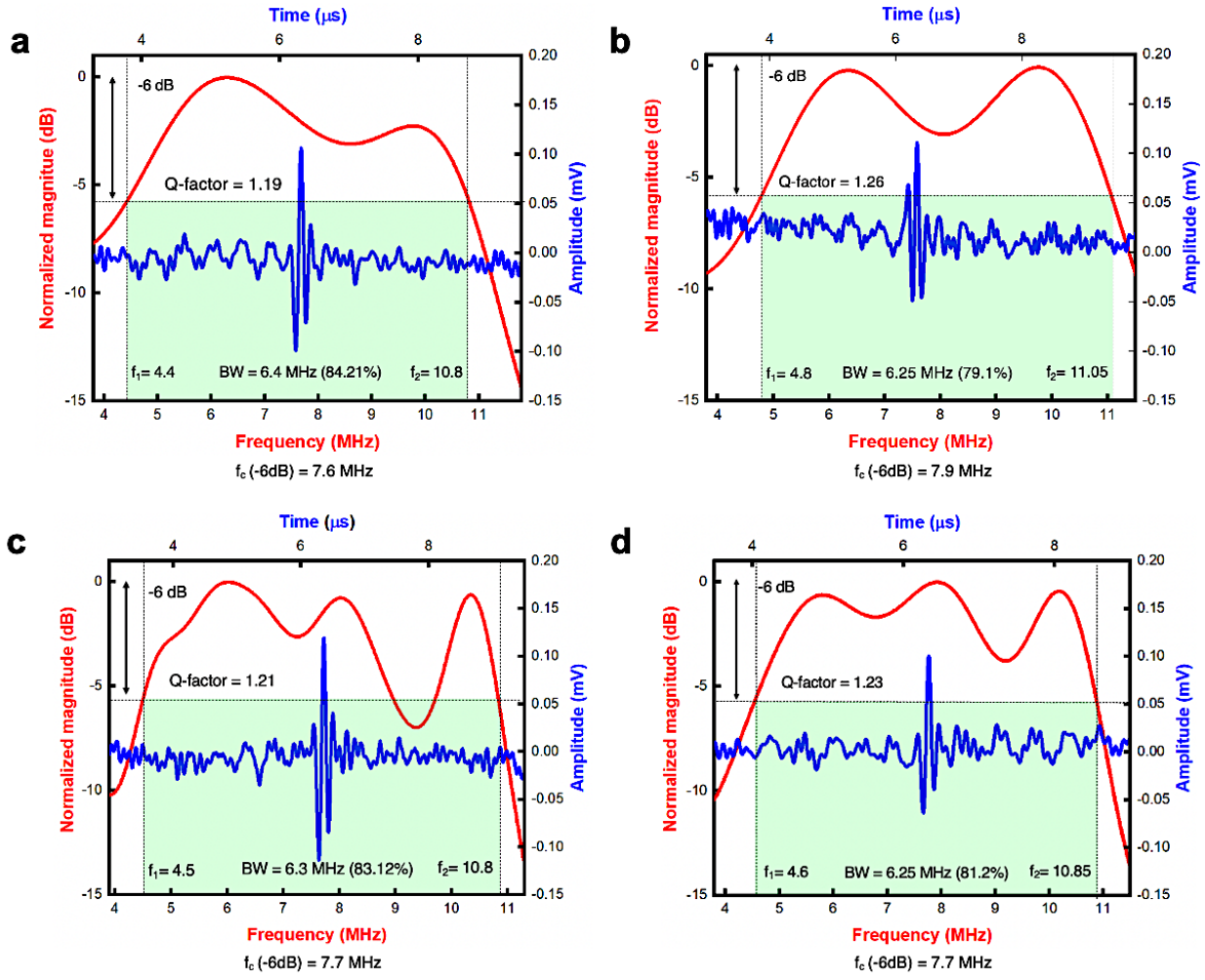

Figure 4.8: Experimental measurement of acoustic bandwidth, central frequency, and quality factor (Q-factor) of the transducer array.

Due to the fact that the majority of the energy is dissipated within the first few vibrations of the ultrasound transducer, a medical sonography utilizes low-Q transducers that create short pulses as the axial resolution is increased when the pulse length is shortened and better resolution provides increased diagnostic information **(Rizzatto 1998)**. Because ultrasonic waves with higher frequencies are absorbed at a faster rate, it is necessary to utilize a transducer with a low-Q. Contrarily, a pulse made up of many cycles will be generated by ultrasound transducers that have a high-Q factor (also known as a narrower frequency response as a result of a narrow bandwidth). Because of this, a transducer with a low Q factor will generate a shorter pulse in the time domain, which will ultimately result in an image with a better resolution. For imaging transducers, a low Q-factor (preferably between 1 and 2) is preferred **(Shung and Zippuro 1996**). As can be seen from **Figure 4.8,** the Q-factor of the transducer channels were marked to be between 1.19 and 1.26, making them suitable for diagnostic imaging applications.

4.4.Acoustic pressure and sound pressure level (SPL)

The theoretical FE models were created using COMSOL 6.0 to mimic the acoustic pressure, and micro fabrication techniques were employed to regulate the aperture of an array of micro square piezo-pixels with a working surface area of 70x70 μm^2 per pixel.

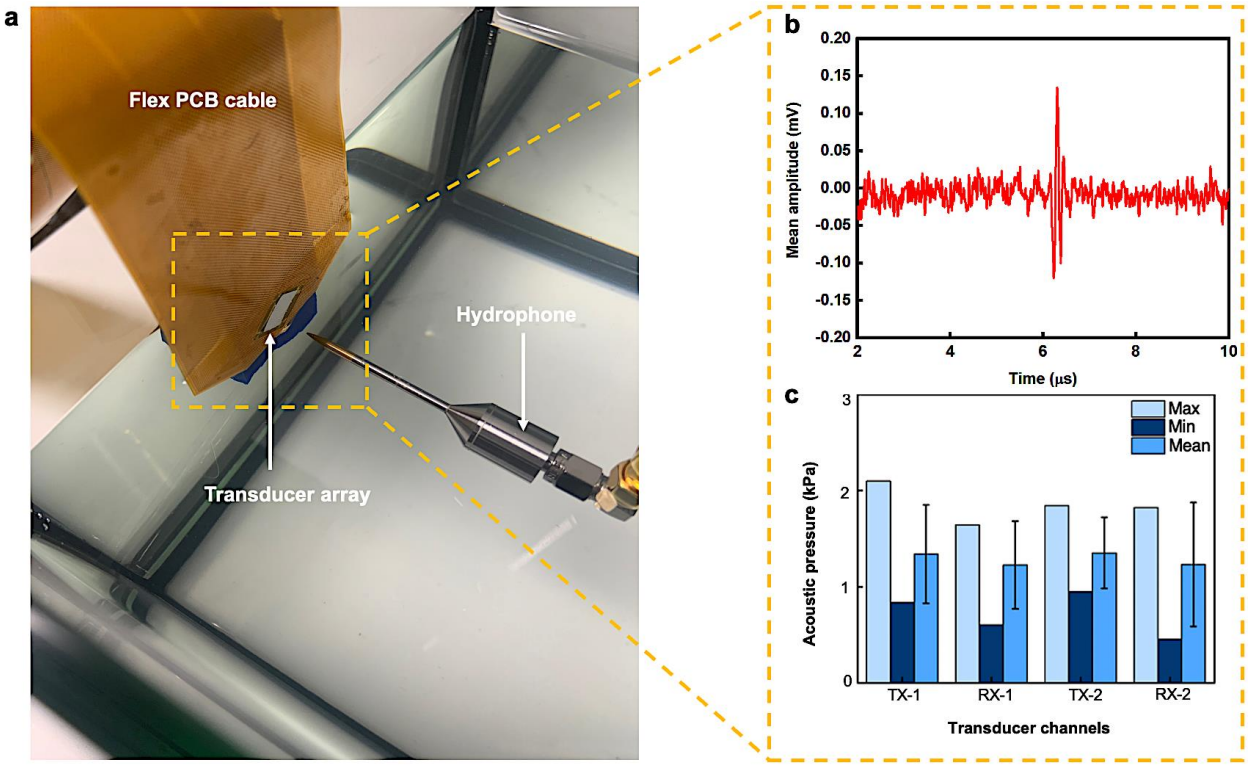

Figure 4.9: Generated acoustic pressure of the transducer channels recorded by the hydrophone: **(a)** needle hydrophone to record acoustic pressure 1 cm away from the stimulated transducer channels; **(b)** recorded mean amplitude (mV) generated by a single pixel and **(c)** corresponding acoustic pressure (kPa) for the pixels from transmitters and receivers.

Results from a COMSOL finite element simulation indicate that, despite their small size, piezo-pixels are capable of generating enough volumetric velocity (the product of frequency and displacement) to create acoustic pressure **(Akhbari et al. 2014).** It was discovered that a single pixel could generate enough displacement in response to the 10V stimulation to roughly generate 0.15 mV, which could be picked up by the needle hydrophone as depicted in **Figures 4.9 (a-b).** The simulation result showed that a single pixel under 10V could generate a maximum 2.62 kPa.

The experimental result also demonstrated similar results under 10V, which was recorded by the hydrophone: T_X-1, R_X-2, T_X-2, and R_X-2 exhibited a maximum of 2.1, 1.64, 1.84, and 1.82 kPa acoustic pressure, respectively (**Figure 4.9c)**. The corresponding sound pressure level (SPL), which is roughly around 180 dB (**Figure 4.10)** is also in agreement to the simulation result that produced 182.16 dB. It must be noted that the theoretical reference pressure value of 1 μPa (or 10^{-6} Pa) for water medium that corresponds to 0 dB was also utilized to determine the SPL for the experimental values. Therefore, it is clear that the micro PZT pixels, while having smaller element size and higher impedance, may deliver output pressure that is comparable with high-frequency standard 2-D ceramic PZT transducer array (382 Pa/V) and piezoelectric micromachined ultrasonic transducers (pMUTs) (116 Pa/V) for medical imaging **(Dausch et al. 2008**).

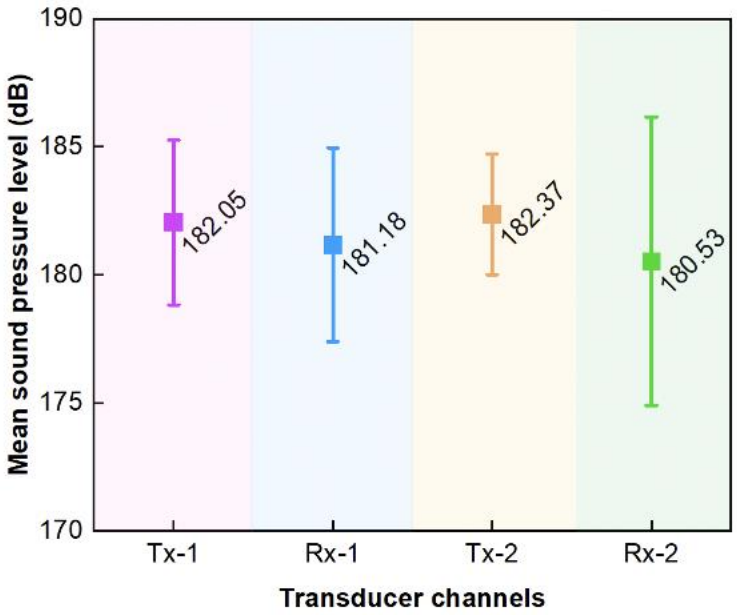

Figure 4.10: Generated sound pressure level (SPL) of the transducer channels recorded by the hydrophone.

4.5.Cross-talk performance

In a transducer array, different vibration modes cause the waves to propagate forward through the matching layers and backward through the backing material. Also, transverse mode vibration allow the wave to propagate in the kerf-filler, resulting in coupled resonance between adjacent or neighboring piezo-parts **(Ramalli et al. 2019).** Interestingly, this inter-element cross-talk may be responsible for considerable distortion of the radiated field of a transducer array. It has been demonstrated that this phenomenon causes unanticipated decrease in transmitted pressure and sensitivity of the receiver. For high-quality medical imaging applications, transducers with a cross-talk <-40 dB is sufficient (C Wang et al. 2022) and the recorded cross-talk (**Figure 4.11)** in the current work is <-50 dB (**Figure 4.12)**, making it suitable for medical imaging

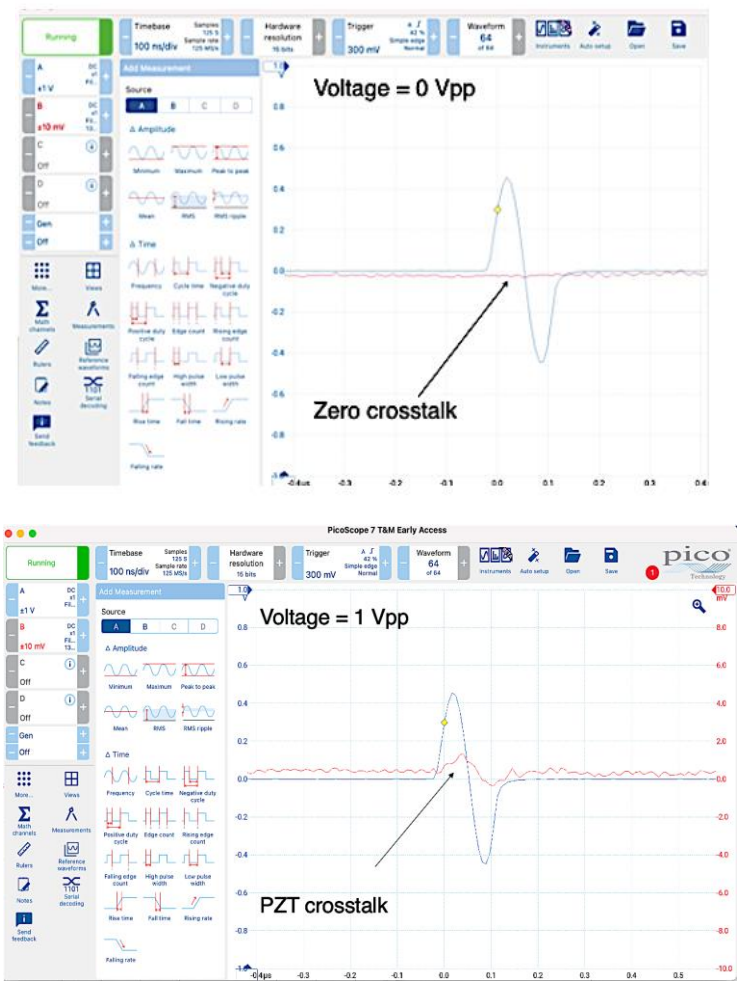

Figure 4.11: Cross-talk characterization and recording by a Picoscope.

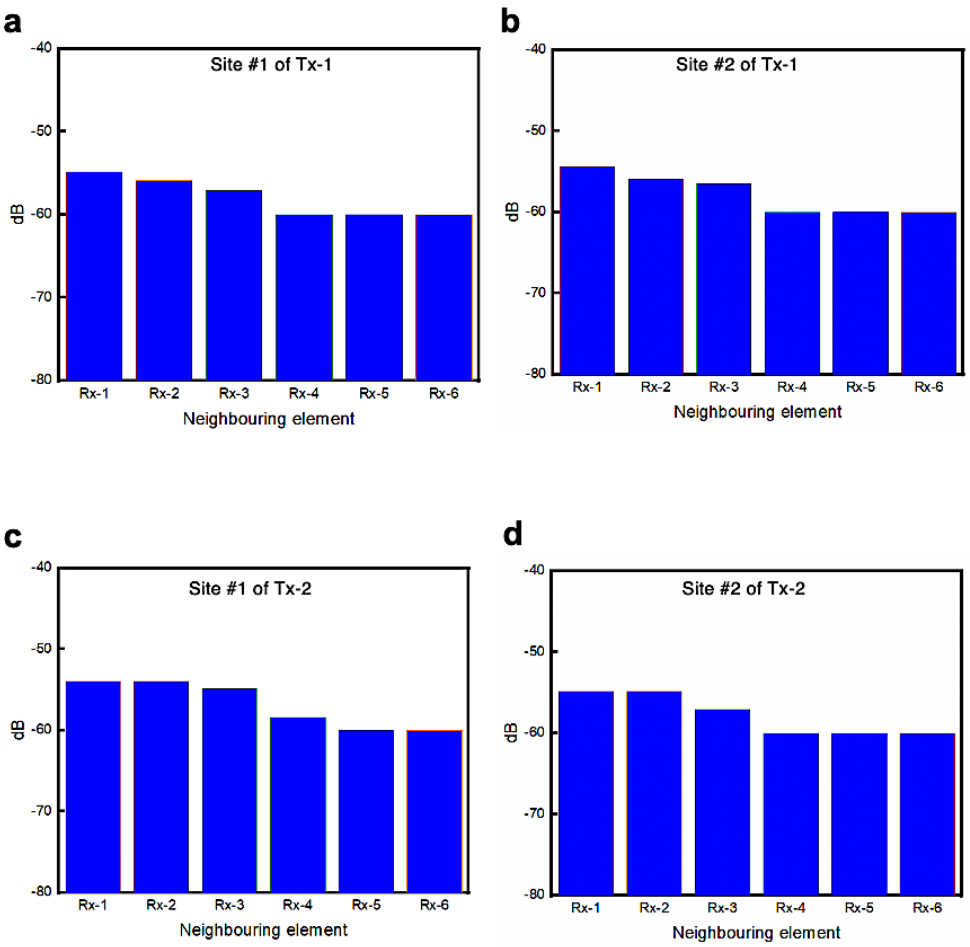

Figure 4.12: Electrical cross-talk recorded by transducer channels.

4.6.Long-term thermal stability for clinical studies on the soft tissue

Using the function generator and a working voltage of 10 Vpp, the temperature of a single pixel was monitored with a thermal camera for 10 minutes to examine its thermal stability. The low operational power of the device resulted in little surface temperature change, proving the thermal stability of the device. **Figure 4.13** depicts the time-temperature profile curve that was measured during the experiment with the unclamped (without the matching and backing layer). The thermal images are exhibited in **Figure 4.14**. It can be seen that the temperature of the PZT pixel did not fluctuate more than approximately 0.8^{o}C although the temperature of E-solder hiked by around 2.5^{o}C. However, the temperature range of the piezo pixel and E-solder were around 30, which is below the accepted skin temperature range (32^{o}C and 35^{o}C) **(Benedict, Miles, and Johnson 1919)**. Furthermore, when the clamped transducer (with matching and backing layer) is investigated, it was found that the device also did not produce any significant temperature rise and remained below 22C ^{o}C when subjected to 10Vpp for a continuous 10-minute period, making this device appropriate for clinical studies on the soft tissue **(Figure 4.15).**

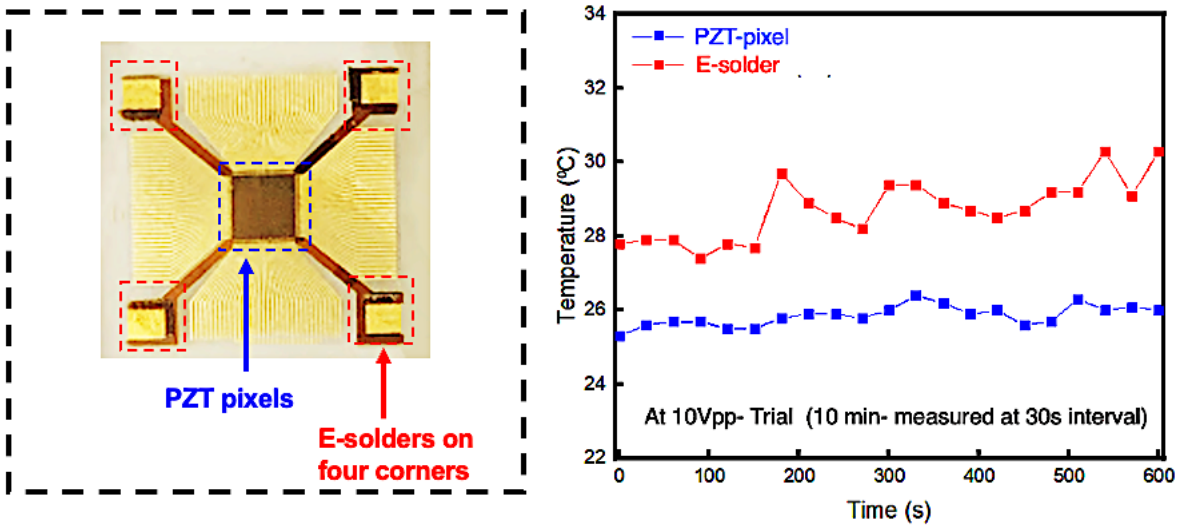

Figure 4.13: Measured time-temperature profile curve of the unclamped transducer array (without matching and backing layer) over a 10-minute period.

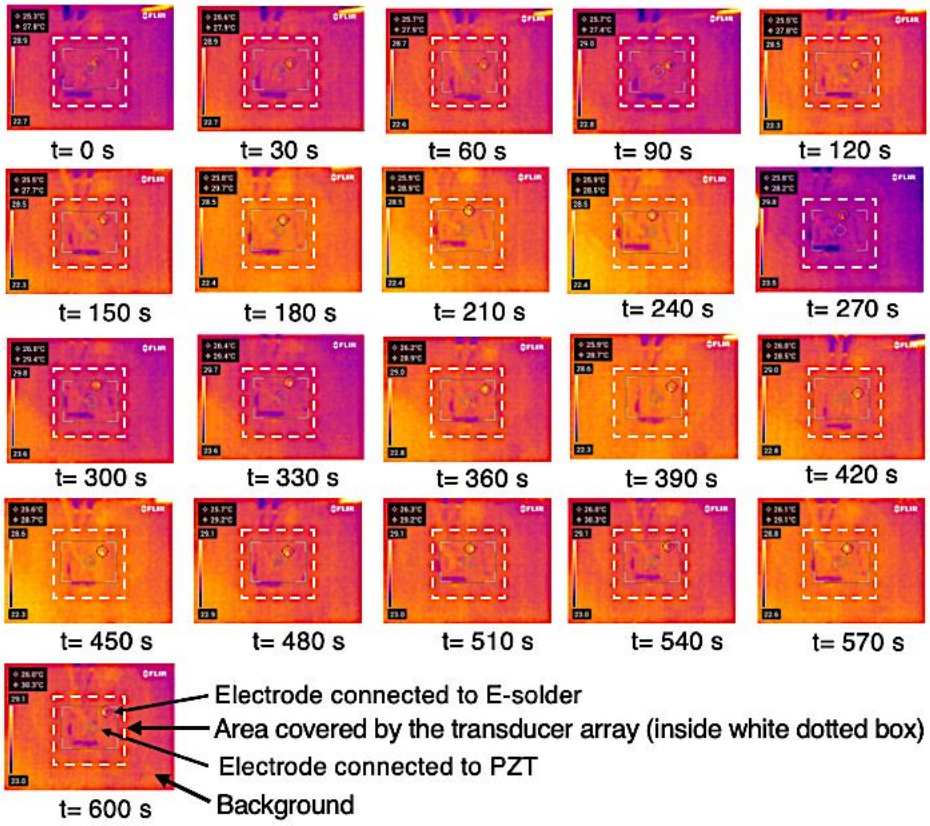

Figure 4.14: Thermal images acquired by the FLIR compact thermal camera at selected time intervals over a 10-minute period (dotted box area represents the area covered by the array).

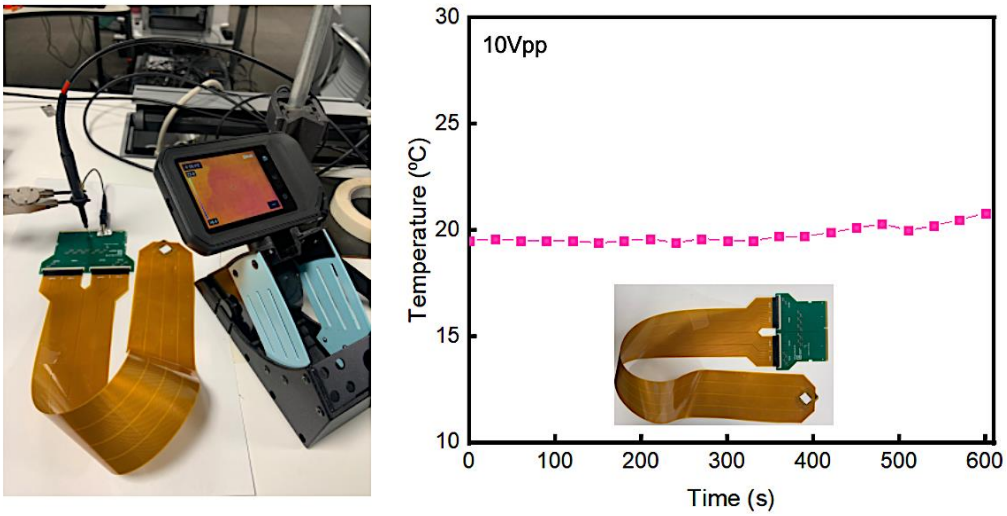

Figure 4.15: Time-temperature profile curve of the transducer and thermal images acquired by the FLIR compact thermal camera at selected time intervals over a 10-minute period.

4.7.Summary

Minimizing the size of transducers is consistently desirable in order to decrease their bulkiness, and this characteristic is particularly advantageous for wearable technology. For the box-shaped 2D array configuration, a microscopic 7.5 MHz phased ultrasound piezoelectric imaging transducer measuring 70x70 μm^2 pixels – based on single crystal or polycrystalline platform – could not be located after an exhaustive search of relevant literature as the fabrication of such transducers presents significant challenges due to the brittleness of the ceramic material, resulting aspect ratio, and the potential for depolarization. The present investigation has effectively illustrated the concept of producing miniaturized imaging transducers and enclosing them in a 2D array configuration. Furthermore, the utilization of a box-shaped design attribute resulted in a reduction of the aperture size to 3.3 x 3.3 mm^2. The overall dimensions of the device, encompassing the ground electrodes positioned at each of its four corners, measure 13.8 x 13.8 mm^2. Furthermore, the congruence between the simulated and experimental outcomes of the piezoelectric and ultrasound capabilities of the transducer is noteworthy. The sparse array configuration of the transducer serves the dual purpose of minimizing cross-talk by a magnitude of less than -50 dB and reducing its overall footprint. Furthermore, it exhibits a longitudinal k_{33}-factor within the range of 0.45-0.5, a low Q-factor of 1.19, an acoustic pressure up to 2.1 kPa at 1 cm, a sound pressure level of 180 dB, exceptional thermal stability with fluctuations of less than 1^oC, and a wide bandwidth of 5.6 MHz (73.41%) that exhibits a higher level of bandwidth performance in comparison to the transducers reported for imaging breast tissue. In summary, the present study introduced a new design for a high-frequency transducer, which was successfully simulated and fabricated that demonstrated promising performance. This innovation has the potential to introduce a new type of ultrasound transducer for biomedical applications.

Chapter 5

5. Conclusion

For the advancement of wearable technology, the incorporation of substantially miniaturized electronic processors and sensors, which facilitate interaction with the human body and are contained within compact organic structures, is essential. Consequently, the reduction in device size plays a crucial role in the development of wearable or conformable ultrasound technology, a topic that has been investigated in this thesis.

The present thesis commences with a comprehensive overview of the fundamental characteristics of piezoelectric materials that are employed in the development of ultrasonic transducers. Furthermore, the article provides a comprehensive summary of various array configurations, their constituent components, and modeling methodologies. Subsequently, the investigation introduced the notion of employing a high-frequency 2D sparse array transducer (7.5 MHz) for biomedical applications. The investigation additionally delineated the complete micromachining procedure involved in the production of the 2D array. Following the design of a precise photolithography photomask, a microfabrication recipe was employed to print the electric circuit pattern onto the piezo pixels, utilizing the aforementioned photomask. Promising outcomes were observed in the piezoelectric characterization and ultrasound performance. Because of its low aperture and excellent piezoelectric and acoustic characteristics maintained at such a compact footprint, the results are encouraging and point to the possible use of this narrow aperture box-shape 2D transducer array for wearable applications in biomedical contexts. Due to its phased array nature, mechanical steering becomes unnecessary, thereby enabling the possibility of integrating multiple arrays within a flexible patch to conform and fix to the curvilinear surface of the human body. Hence, prospective investigations may concentrate on various significant advancements.

Bibliography

Abas, Amry Amin et al. 2010. “Effect of Backing Layer Composition on Ultrasonic Probe Bandwidth.” In *INSTRUMENTATION RELATED TO NUCLEAR SCIENCE AND TECHNOLOGY (S46)*, https://inis.iaea.org/search/search.aspx?orig_q=RN:43056468.

Akhbari, Sina et al. 2014. “Highly Responsive Curved Aluminum Nitride PMUT.” In *2014 IEEE 27th International Conference on Micro Electro Mechanical Systems (MEMS)*, IEEE, 124–27. http://ieeexplore.ieee.org/document/6765589/.

Apple Inc. 2023. “Compare AirPods Models.” https://www.apple.com/airpods/compare/.

Assaad, Jamal et al. 1996. “Influence of the Thickness and the Attenuation Coefficient of a Backing on the Response of Transducers.” *Ultrasonics* 34(2–5): 103–6. https://linkinghub.elsevier.com/retrieve/pii/0041624X96000091.

Benedict, F. G., W. R. Miles, and Alice Johnson. 1919. “The Temperature of the Human Skin.” *Proceedings of the National Academy of Sciences* 5(6): 218–22. https://pnas.org/doi/full/10.1073/pnas.5.6.218.

Cain, Markys, Maria Lodeiro, Mark Stewart, and Matthew Theobalds. 2002. *6MPI0301: Losses in Piezoelectric Materials*. https://eprintspublications.npl.co.uk/2481/1/MATC126.pdf.

Calvert, J., F. Duck, S. Clift, and H. Azaime. 2007. “Surface Heating by Transvaginal Transducers.” *Ultrasound in Obstetrics and Gynecology* 29(4): 427–32. https://onlinelibrary.wiley.com/doi/10.1002/uog.3973.

Camacho, Jorge, Linas Svilainis, and Tomás Gómez Álvarez-Arenas. 2022. “Ultrasonic Imaging and Sensors.” *Sensors* 22(20): 7911. https://www.mdpi.com/1424-8220/22/20/7911.

Cannata, J.M. et al. 2003. “Design of Efficient, Broadband Single-Element (20-80 MHz) Ultrasonic Transducers for Medical Imaging Applications.” *IEEE Transactions on Ultrasonics, Ferroelectrics and Frequency Control* 50(11): 1548–57. http://ieeexplore.ieee.org/document/1251138/.

CHAUDHARY, BIKASH KUMAR. 2007. “Dual Frequency Ultrasound Transducer Array.” University College of Southeast Norway.

Chen, Ching-Mei, and Bhaskar Choubey. 2018. “Ultrasound Transducer Quality Factor Control Using Coupled External Electrical Resonator.” In *2018 IEEE SENSORS*, IEEE, 1–4. https://ieeexplore.ieee.org/document/8589657/.

Chen, Jianzhong, Wei Liu, Dianbao Gu, and Dawei Wu. 2022. “Laser Scanning Guided Localization Imaging with a Laser-Machined Two-Dimensional Flexible Ultrasonic Array.” *Micromachines* 13(5): 754. https://www.mdpi.com/2072-666X/13/5/754.

Chen, Jianzhong, Wei Liu, Dawei Wu, and Hu Ye. 2022. “Laser Micromachined Flexible Ultrasound Line Array and Subplanar Multimodal Imaging Applications.” *IEEE Open Journal of Ultrasonics, Ferroelectrics, and Frequency Control* 2: 131–39. https://ieeexplore.ieee.org/document/9819962/.

Chen, Ruimin et al. 2019. “Eco-Friendly Highly Sensitive Transducers Based on a New KNN–NTK–FM Lead-Free Piezoelectric Ceramic for High-Frequency Biomedical Ultrasonic Imaging Applications.” *IEEE Transactions on Biomedical Engineering* 66(6): 1580–87. https://ieeexplore.ieee.org/document/8540434/.

COMSOL. 2017. *Acoustics Module User’s Guide*. https://doc.comsol.com/5.3/doc/com.comsol.help.aco/AcousticsModuleUsersGuide.pdf.

Cowan, F. 2005. “Does Cranial Ultrasound Imaging Identify Arterial Cerebral Infarction in Term Neonates?” *Archives of Disease in Childhood - Fetal and Neonatal Edition* 90(3): F252-f256. https://fn.bmj.com/lookup/doi/10.1136/adc.2004.055558.

Dausch, David E., John B. Castellucci, Derrick R. Chou, and Olaf T. von Ramm. 2008. “Theory and Operation of 2-D Array Piezoelectric Micromachined Ultrasound Transducers.” *IEEE Transactions on Ultrasonics, Ferroelectrics, and Frequency Control* 55(11): 2484–92. https://ieeexplore.ieee.org/document/4686880/.

Denina, Marco et al. 2020. “Lung Ultrasound in Children With COVID-19.” *Pediatrics* 146(1). https://publications.aap.org/pediatrics/article/146/1/e20201157/37014/Lung-Ultrasound-in-Children-With-COVID-19.

Drinkwater, Bruce W., and Paul D. Wilcox. 2006. “Ultrasonic Arrays for Non-Destructive Evaluation: A Review.” *NDT & E International* 39(7): 525–41. https://linkinghub.elsevier.com/retrieve/pii/S0963869506000272.

Elloian, Jeffrey et al. 2022. “Flexible Ultrasound Transceiver Array for Non-Invasive Surface-Conformable Imaging Enabled by Geometric Phase Correction.” *Scientific Reports* 12(1): 16184. https://www.nature.com/articles/s41598-022-20721-7.

Fregeac, Arnaud, Florence Ansart, Serge Selezneff, and Claude Estournès. 2019. “Relationship between Mechanical Properties and Microstructure of Yttria Stabilized Zirconia Ceramics

Densified by Spark Plasma Sintering." *Ceramics International* 45(17): 23740–49. https://linkinghub.elsevier.com/retrieve/pii/S0272884219322874.

Google. 2023. "Pixel Buds Pro." *Google Store*.

GOUWY, ISABELLE. 2018. "HL2029 Medical Engineering Advanced Course (KTH Royal Institute of Technology)." *KTH Royal Institute of Technology*. file:///Users/IKRASAMHA/Downloads/on-the-investigation-of-transd.pdf (October 31, 2022).

Grewe, M.G., T.R. Gururaja, T.R. Shrout, and R.E. Newnham. 1990. "Acoustic Properties of Particle/Polymer Composites for Ultrasonic Transducer Backing Applications." *IEEE Transactions on Ultrasonics, Ferroelectrics and Frequency Control* 37(6): 506–14. http://ieeexplore.ieee.org/document/63106/.

Gupta, Nishant et al. 2017. "Neonatal Cranial Sonography: Ultrasound Findings in Neonatal Meningitis—a Pictorial Review." *Quantitative Imaging in Medicine and Surgery* 7(1): 123–31. http://qims.amegroups.com/article/view/13718/14095.

Gururaja, T.R. 1992. "Piezoelectric Transducers for Medical Ultrasonic Imaging." In *ISAF '92: Proceedings of the Eighth IEEE International Symposium on Applications of Ferroelectrics*, IEEE, 259–65. http://ieeexplore.ieee.org/document/300680/.

Haber, Hans P. 2007. "Cystic Fibrosis in Children and Young Adults: Findings on Routine Abdominal Sonography." *American Journal of Roentgenology* 189(1): 89–99. https://www.ajronline.org/doi/10.2214/AJR.06.1046.

Hamelmann, Paul et al. 2019. "Fetal Heart Rate Monitoring Implemented by Dynamic Adaptation of Transmission Power of a Flexible Ultrasound Transducer Array." *Sensors* 19(5): 1195. https://www.mdpi.com/1424-8220/19/5/1195.

Hazelwood, Richard A., and Stephen P Robinson. 2007. "Underwater Acoustic Power Measurements in Reverberant Fields." In *OCEANS 2007 - Europe*, IEEE, 1–6. http://ieeexplore.ieee.org/document/4302295/.

Hohl, C. et al. 2007. "Ultrasonography of the Pancreas. 2. Harmonic Imaging." *Abdominal Imaging* 32(2): 150–60. https://link.springer.com/10.1007/s00261-006-9017-z.

Hossain, Md Murad, Niloufar Saharkhiz, and Elisa E. Konofagou. 2020. "In Vivo Demonstration of Single Transducer Harmonic Motion Imaging (ST-HMI) in a Breast Cancer Mouse Model and Breast Cancer Patients." In *2020 IEEE International Ultrasonics Symposium*

(IUS), IEEE, 1–4. https://ieeexplore.ieee.org/document/9251522/.

Hu, Hongjie et al. 2018. "Stretchable Ultrasonic Transducer Arrays for Three-Dimensional Imaging on Complex Surfaces." *Science Advances* 4(3). https://www.science.org/doi/10.1126/sciadv.aar3979.

Hübner, U. et al. 2000. "Ultrasound in the Diagnosis of Fractures in Children." *The Journal of Bone and Joint Surgery. British volume* 82-B(8): 1170–73. https://online.boneandjoint.org.uk/doi/10.1302/0301-620X.82B8.0821170.

Hunt, John W., Marcel Arditi, and F. Stuart Foster. 1983. "Ultrasound Transducers for Pulse-Echo Medical Imaging." *IEEE Transactions on Biomedical Engineering* BME-30(8): 453–81. http://ieeexplore.ieee.org/document/4121677/.

Jackson, V P et al. 1986. "Automated Breast Sonography Using a 7.5-MHz PVDF Transducer: Preliminary Clinical Evaluation. Work in Progress." *Radiology* 159(3): 679–84. http://pubs.rsna.org/doi/10.1148/radiology.159.3.3517952.

Jaeyoung Son et al. 2014. "A New Automated Breast Ultrasound System with Dual Wide Field-of-View Imaging." In *2014 IEEE International Ultrasonics Symposium*, IEEE, 1615–18. http://ieeexplore.ieee.org/document/6931887/.

Jeng, Yeau-Ren, Ping-Chi Tsai, and Te-Hua Fang. 2003. "Nanomeasurement and Fractal Analysis of PZT Ferroelectric Thin Films by Atomic Force Microscopy." *Microelectronic Engineering* 65(4): 406–15. https://linkinghub.elsevier.com/retrieve/pii/S0167931703000522.

Jiang, Laiming et al. 2022. "Flexible Ultrasound-Induced Retinal Stimulating Piezo-Arrays for Biomimetic Visual Prostheses." *Nature Communications* 13(1): 3853. https://www.nature.com/articles/s41467-022-31599-4.

Killingback, Alban L.T., Valentine R. Newey, Mohamed A. El-Brawany, and Dariush K. Nassiri. 2008. "Development of a Thermal Test Object for the Measurement of Ultrasound Intracavity Transducer Self-Heating." *Ultrasound in Medicine & Biology* 34(12): 2035–42. https://linkinghub.elsevier.com/retrieve/pii/S0301562908002664.

Kim, Taeyang et al. 2020. "Flexible 1–3 Composite Ultrasound Transducers With Silver-Nanowire-Based Stretchable Electrodes." *IEEE Transactions on Industrial Electronics* 67(8): 6955–62. https://ieeexplore.ieee.org/document/8818629/.

Krimholtz, R., D.A. Leedom, and G.L. Matthaei. 1970. "New Equivalent Circuits for Elementary

Piezoelectric Transducers." *Electronics Letters* 6(13): 398. https://digital-library.theiet.org/content/journals/10.1049/el_19700280.

Kuttruff, Heinrich. 2007. *Acoustics: An Introduction*. Taylor & Francis.

Li, Jiapu et al. 2022. "Recent Advancements in Ultrasound Transducer: From Material Strategies to Biomedical Applications." *BME Frontiers* 2022. https://spj.science.org/doi/10.34133/2022/9764501.

Li, Jing-Feng. 2021. "Fundamentals of Piezoelectricity." In *Lead-Free Piezoelectric Materials*, Wiley, 1–18. https://onlinelibrary.wiley.com/doi/10.1002/9783527817047.ch1.

Li, Sibo. 2017. "Micromachined Piezoelectric Material and Dual-Layer Transducers for Ultrasound Imaging." North Carolina State University.

Lim, S.K., M.F. Zamri, and A.R. Yusoff. 2022. "Structure Integrity Analysis on Nickel–Diamond Blade in Dicing of Hard-Brittle Ceramic Die." *Procedia CIRP* 108: 465–69. https://linkinghub.elsevier.com/retrieve/pii/S2212827122005455.

Liu, W et al. 2008. "Acoustic Backscatter and Effective Scatterer Size Estimates Using a 2D CMUT Transducer." *Physics in Medicine and Biology* 53(15): 4169–83. https://iopscience.iop.org/article/10.1088/0031-9155/53/15/011.

Liu, Ya-Han et al. 2022. "Transparent Flexible Piezoelectric Ultrasound Transducer for Photoacoustic Imaging System." *IEEE Sensors Journal* 22(3): 2070–77. https://ieeexplore.ieee.org/document/9652558/.

Lucas, Valentina S., Ruth S. Burk, Sue Creehan, and Mary Jo Grap. 2014. "Utility of High-Frequency Ultrasound." *Plastic Surgical Nursing* 34(1): 34–38. https://journals.lww.com/00006527-201401000-00012.

Martínez, O. 2003. "A Small 2D Ultrasonic Array for NDT Applications." *NDT & E International* 36(1): 57–63. https://linkinghub.elsevier.com/retrieve/pii/S0963869502000725.

McFarlin, Barbara L. et al. 2005. "Ultrasound Insertion Loss of the Rat Cervix." *American Journal of Obstetrics and Gynecology* 193(6): S154. https://linkinghub.elsevier.com/retrieve/pii/S0002937805021575.

Medina, Jimmy E San Miguel. 2005. "NUMERICAL MODELING OF A CIRCULAR PIEZOELECTRIC ULTRASONIC TRANSDUCER RADIATING IN WATER INSTRUCTIONS." https://www.abcm.org.br/anais/cobem/2005/PDF/COBEM2005-

1814.pdf.

Morel, A., G. Pillonnet, Y. Wanderoild, and A. Badel. 2018. “Dielectric Losses Considerations for Piezoelectric Energy Harvesting.” *Journal of Low Power Electronics* 14(2): 244–54. http://www.ingentaconnect.com/content/10.1166/jolpe.2018.1562.

Munk, B. et al. 2000. “Ultrasound for Diagnosis of Scaphoid Fractures.” *Journal of Hand Surgery* 25(4): 369–71. http://journals.sagepub.com/doi/10.1054/jhsb.2000.0432.

Murphy, Andrew, and Mirjan Nadrljanski. 2010. “Ultrasound Frequencies.” In *Radiopaedia.Org*, Radiopaedia.org. http://radiopaedia.org/articles/8664.

Nagata, Naruhiko et al. 2003. “Sonographic Evaluation of the Anterior Liver Surface in Chronic Liver Diseases Using a 7.5-MHz Annular-Array Transducer: Correlation with Laparoscopic and Histopathologic Findings.” *Journal of Clinical Ultrasound* 31(8): 393–400. https://onlinelibrary.wiley.com/doi/10.1002/jcu.10195.

Nowicki, Andrzej. 2020. “Safety of Ultrasonic Examinations; Thermal and Mechanical Indices.” *Medical Ultrasonography* 22(2): 203. https://www.medultrason.ro/medultrason/index.php/medultrason/article/view/2372.

Otto, Catherine M. 2019. *TEXTBOOK of CLINICAL ECHOCARDIOGRAPHY*. 6th ed. Elsevier.

Ou-Yang, Jun et al. 2015. “New KNN-Based Lead-Free Piezoelectric Ceramic for High-Frequency Ultrasound Transducer Applications.” *Applied Physics A* 118(4): 1177–81. http://link.springer.com/10.1007/s00339-015-9004-8.

Paul, Y et al. 1997. “SIDE LOBES AND GRATING LOBES ARTIFACTS IN ULTRASOUND IMAGING.” *Veterinary Radiology <html_ent glyph="@amp;" ascii="&"/> Ultrasound* 38(5): 387–93. https://onlinelibrary.wiley.com/doi/10.1111/j.1740-8261.1997.tb02104.x.

Peng, Chang et al. 2021. “Noninvasive and Nonocclusive Blood Pressure Monitoring via a Flexible Piezo-Composite Ultrasonic Sensor.” *IEEE Sensors Journal* 21(3): 2642–50. https://ieeexplore.ieee.org/document/9186675/.

Persson, H.W., and C.H. Hertz. 1985. “Acoustic Impedance Matching of Medical Ultrasound Transducers.” *Ultrasonics* 23(2): 83–89. https://linkinghub.elsevier.com/retrieve/pii/0041624X8590037X.

Qiu, Yongqiang et al. 2015. “Piezoelectric Micromachined Ultrasound Transducer (PMUT) Arrays for Integrated Sensing, Actuation and Imaging.” *Sensors* 15(4): 8020–41.

http://www.mdpi.com/1424-8220/15/4/8020.

Qu, Mengjiao et al. 2022. “Imaging of Simulated Muscle Based on Single Chip of AlN Piezoelectric Micromachined Ultrasonic Transducer.” *Journal of Micromechanics and Microengineering* 32(7): 075003. https://iopscience.iop.org/article/10.1088/1361-6439/ac70a6.

Ramadas, S.N., R.L. O’Leary, and A. Gachagan. 2009. “Ultrasonic Sensor Design for NDE Application: Design Challenges & Considerations.” In *Proceedings of the National Seminar & Exhibition on Non-Destructive Evaluation*, , 88–91. https://www.ndt.net/?id=9819.

Ramalli, Alessandro, Jan D’hooge, Lasse Lovstakken, and Piero Tortoli. 2019. “A Direct Measurement of Inter-Element Cross-Talk in Ultrasound Arrays.” In *2019 IEEE International Ultrasonics Symposium (IUS)*, IEEE, 1301–3. https://ieeexplore.ieee.org/document/8926249/.

Reali, Francesca et al. 2014. “Can Lung Ultrasound Replace Chest Radiography for the Diagnosis of Pneumonia in Hospitalized Children?” *Respiration* 88(2): 112–15. https://www.karger.com/Article/FullText/362692.

Ritter, T. et al. 1999. “Performance of a High Dielectric Constant Piezoelectric Ceramic for Ultrasound Transducers.” In *1999 IEEE Ultrasonics Symposium. Proceedings. International Symposium (Cat. No.99CH37027)*, IEEE, 1295–98. http://ieeexplore.ieee.org/document/849234/.

Rizzatto, Giorgio. 1998. “Ultrasound Transducers.” *European Journal of Radiology* 27: S188–95. https://linkinghub.elsevier.com/retrieve/pii/S0720048X98000618.

Rödel, Jürgen, and Jing-Feng Li. 2018. “Lead-Free Piezoceramics: Status and Perspectives.” *MRS Bulletin* 43(8): 576–80. http://link.springer.com/10.1557/mrs.2018.181.

Rouyer, Julien et al. 2012. “Conformal Ultrasound Imaging System for Anatomical Breast Inspection.” *IEEE Transactions on Ultrasonics, Ferroelectrics and Frequency Control* 59(7): 1457–69. http://ieeexplore.ieee.org/document/6242802/.

S, Atheeth, Kajoli Krishnan, and Manish Arora. 2023. “Review of PMUTs for Medical Imaging: Towards High Frequency Arrays.” *Biomedical Physics & Engineering Express* 9(2): 022001. https://iopscience.iop.org/article/10.1088/2057-1976/acaab2.

Sadeghpour, Sina et al. 2021. “A 128×1 Phased Array Piezoelectric Micromachined Ultrasound Transducer (PMUT) for Medical Imaging.” In *2021 21st International*

Conference on Solid-State Sensors, Actuators and Microsystems (Transducers), IEEE, 34–37. https://ieeexplore.ieee.org/document/9495521/.

Salomon, Georg et al. 2008. "Evaluation of Prostate Cancer Detection with Ultrasound Real-Time Elastography: A Comparison with Step Section Pathological Analysis after Radical Prostatectomy." *European Urology* 54(6): 1354–62. https://linkinghub.elsevier.com/retrieve/pii/S0302283808002686.

Saunders, O, S Clift, and F Duck. 2004. "Ultrasound Transducer Self Heating: Development of 3-D Finite-Element Models." *Journal of Physics: Conference Series* 1: 72–77. https://iopscience.iop.org/article/10.1088/1742-6596/1/1/017.

Sayers, C.M., and C.E. Tait. 1984. "Ultrasonic Properties of Transducer Backings." *Ultrasonics* 22(2): 57–60. https://linkinghub.elsevier.com/retrieve/pii/0041624X84900222.

Scheithauer, Uwe et al. 2017. "Ceramic-Based 4D Components: Additive Manufacturing (AM) of Ceramic-Based Functionally Graded Materials (FGM) by Thermoplastic 3D Printing (T3DP)." *Materials* 10(12): 1368. http://www.mdpi.com/1996-1944/10/12/1368.

Shankar, Hariharan, Paul S. Pagel, and David S. Warner. 2011. "Potential Adverse Ultrasound-Related Biological Effects." *Anesthesiology* 115(5): 1109–24. https://pubs.asahq.org/anesthesiology/article/115/5/1109/12838/Potential-Adverse-Ultrasoundrelated-Biological.

Shekhani, Husain N. 2016. "Characterization of the High Power Properties of Piezoelectric Ceramics Using the Burst Method: Methodology, Analysis, and Experimental Approach." The Pennsylvania State University. https://etda.libraries.psu.edu/files/final_submissions/11952.

Shung, K.K., and M. Zippuro. 1996. "Ultrasonic Transducers and Arrays." *IEEE Engineering in Medicine and Biology Magazine* 15(6): 20–30. http://ieeexplore.ieee.org/document/544509/.

Shung, K. 2002. "The Principle of Multidimensional Arrays." *European Journal of Echocardiography* 3(2): 149–53. https://academic.oup.com/ehjcimaging/article-lookup/doi/10.1053/euje.2001.0139.

Shuvo, Ikra Iftekhar, Justine Decaens, Dominic Lachapelle, and Patricia Dolez. 2021. "Smart Textiles Testing: A Roadmap to Standardized Test Methods for Safety and Quality-Control." In *Textiles for Functional Applications [Working Title]*, IntechOpen. https://www.intechopen.com/online-first/smart-textiles-testing-a-roadmap-to-standardized-

test-methods-for-safety-and-quality-control.

Smith, W.A., and B.A. Auld. 1991. “Modeling 1-3 Composite Piezoelectrics: Thickness-Mode Oscillations.” *IEEE Transactions on Ultrasonics, Ferroelectrics and Frequency Control* 38(1): 40–47. http://ieeexplore.ieee.org/document/67833/.

Smyth, K. M., C. G. Sodini, and S.-G. Kim. 2017. “High Electromechanical Coupling Piezoelectric Micro-Machined Ultrasonic Transducer (PMUT) Elements for Medical Imaging.” In *2017 19th International Conference on Solid-State Sensors, Actuators and Microsystems (TRANSDUCERS)*, IEEE, 966–69. http://ieeexplore.ieee.org/document/7994211/.

Smyth, Katherine Marie. 2012. “Design and Modeling of a PZT Thin Film Based Piezoelectric Micromachined Ultrasonic Transducer (PMUT).” http://hdl.handle.net/1721.1/74942.

Soldati, Gino, Roberto Copetti, and Sara Sher. 2009. “Sonographic Interstitial Syndrome.” *Journal of Ultrasound in Medicine* 28(2): 163–74. http://doi.wiley.com/10.7863/jum.2009.28.2.163.

Sprague, Mark W., and Joseph J. Luczkovich. 2004. “Measurement of an Individual Silver Perch Bairdiella Chrysoura Sound Pressure Level in a Field Recording.” *The Journal of the Acoustical Society of America* 116(5): 3186–91. http://asa.scitation.org/doi/10.1121/1.1802651.

Stauffer, P.R., and M.M. Paulides. 2014. “Hyperthermia Therapy for Cancer.” In *Comprehensive Biomedical Physics*, Elsevier, 115–51. https://linkinghub.elsevier.com/retrieve/pii/B9780444536327010091.

Stengel, Dirk et al. 2001. “Discriminatory Power of 3.5 MHz Convex and 7.5 MHz Linear Ultrasound Probes for the Imaging of Traumatic Splenic Lesions: A Feasibility Study.” *The Journal of Trauma: Injury, Infection and Critical Care* 51(1).

Sun, Ping et al. 2010. “High Frequency PMN-PT 1-3 Composite Transducer for Ultrasonic Imaging Application.” *Ferroelectrics* 408(1): 120–28. http://www.tandfonline.com/doi/abs/10.1080/00150193.2010.485546.

Švec, Jan G., and Svante Granqvist. 2018. “Tutorial and Guidelines on Measurement of Sound Pressure Level in Voice and Speech.” *Journal of Speech, Language, and Hearing Research* 61(3): 441–61. http://pubs.asha.org/doi/10.1044/2017_JSLHR-S-17-0095.

Szabo, Thomas L. 2014. *Diagnostic Ultrasound Imaging: Inside Out*. Elsevier.

https://linkinghub.elsevier.com/retrieve/pii/C20110072617.

Szabo, Thomas L., and Peter A. Lewin. 2007. “Piezoelectric Materials for Imaging.” *Journal of Ultrasound in Medicine* 26(3): 283–88. http://doi.wiley.com/10.7863/jum.2007.26.3.283.

———. 2013. “Ultrasound Transducer Selection in Clinical Imaging Practice.” *Journal of Ultrasound in Medicine* 32(4): 573–82. http://doi.wiley.com/10.7863/jum.2013.32.4.573.

Targhetta, RéMi et al. 1993. “Ultrasonic Signs of Pneumothorax: Preliminary Work.” *Journal of Clinical Ultrasound* 21(4): 245–50. https://onlinelibrary.wiley.com/doi/10.1002/jcu.1870210406.

Turner, Brendan L. et al. 2021. “Ultrasound-Powered Implants: A Critical Review of Piezoelectric Material Selection and Applications.” *Advanced Healthcare Materials* 10(17): 2100986. https://onlinelibrary.wiley.com/doi/10.1002/adhm.202100986.

Ueberschlag, Leila. 2020. “A Smart Bra for Detecting Early-Stage Breast Cancer.” *EPFL News*. https://actu.epfl.ch/news/a-smart-bra-for-detecting-early-stage-breast-cance/.

Ueda, Daisuke. 1990. “Normal Volume of the Thyroid Gland in Children.” *Journal of Clinical Ultrasound* 18(6): 455–62. https://onlinelibrary.wiley.com/doi/10.1002/jcu.1870180602.

URICK, R.J. 1979. *SOUND PROPAGATION IN THE SEA*. https://apps.dtic.mil/sti/pdfs/ADA319320.pdf.

Wang, C et al. 2022. “Bioadhesive Ultrasound for Long-Term Continuous Imaging of Diverse Organs.” *Science* 377(6605): 517–23. https://www.science.org/doi/10.1126/science.abo2542.

Wang, Chonghe et al. 2018. “Monitoring of the Central Blood Pressure Waveform via a Conformal Ultrasonic Device.” *Nature Biomedical Engineering* 2(9): 687–95. https://www.nature.com/articles/s41551-018-0287-x.

———. 2021. “Continuous Monitoring of Deep-Tissue Haemodynamics with Stretchable Ultrasonic Phased Arrays.” *Nature Biomedical Engineering* 5(7): 749–58. https://www.nature.com/articles/s41551-021-00763-4.

Wang, Xiaoyu et al. 2020. “Low Insertion Loss Air-Coupled Ultrasonic Transducer with Parallel Laminated Piezoelectric Structure.” *AIP Advances* 10(10): 105331. http://aip.scitation.org/doi/10.1063/5.0022598.

Wei, Luxi et al. 2022. “Sparse 2-D PZT-on-PCB Arrays With Density Tapering.” *IEEE Transactions on Ultrasonics, Ferroelectrics, and Frequency Control* 69(10): 2798–2809.

https://ieeexplore.ieee.org/document/9878093/.

Wells, P N T. 2006. “Ultrasound Imaging.” *Physics in Medicine and Biology* 51(13): R83–98. https://iopscience.iop.org/article/10.1088/0031-9155/51/13/R06.

Wu, Yang et al. 2022. “Research on the Multi-Element Synthetic Aperture Focusing Technique in Breast Ultrasound Imaging, Based on the Ring Array.” *Micromachines* 13(10): 1753. https://www.mdpi.com/2072-666X/13/10/1753.

Xue, Xiangming et al. 2023. “Development of a Wearable Ultrasound Transducer for Sensing Muscle Activities in Assistive Robotics Applications.” *Biosensors* 13(1): 134. https://www.mdpi.com/2079-6374/13/1/134.

Yao, Junlong et al. 2009. “Enhancement of Dielectric Constant and Piezoelectric Coefficient of Ceramic–Polymer Composites by Interface Chelation.” *Journal of Materials Chemistry* 19(18): 2817. http://xlink.rsc.org/?DOI=b819910h.

Zhang, Lin et al. 2022. “Conformable Phased Array Ultrasound Patch for Bladder Volume Monitoring.” *Nature Electronics*.

Zhang, Zhang et al. 2018. “Design and Comparison of PMN-PT Single Crystals and PZT Ceramics Based Medical Phased Array Ultrasonic Transducer.” *Sensors and Actuators A: Physical* 283: 273–81. https://linkinghub.elsevier.com/retrieve/pii/S0924424718312895.

Zhang, Zhiqiang et al. 2018. “High-Performance Ultrasound Needle Transducer Based on Modified PMN-PT Ceramic With Ultrahigh Clamped Dielectric Permittivity.” *IEEE Transactions on Ultrasonics, Ferroelectrics, and Frequency Control* 65(2): 223–30. https://ieeexplore.ieee.org/document/8128507/.

Zhou, Qifa et al. 2014. “Piezoelectric Single Crystal Ultrasonic Transducers for Biomedical Applications.” *Progress in Materials Science* 66: 87–111. https://linkinghub.elsevier.com/retrieve/pii/S0079642514000541.

Zipparo, M.J., K.K. Shung, and T.R. Shrout. 1997. “Piezoceramics for High-Frequency (20 to 100 MHz) Single-Element Imaging Transducers.” *IEEE Transactions on Ultrasonics, Ferroelectrics and Frequency Control* 44(5): 1038–48. http://ieeexplore.ieee.org/document/655629/.

Appendix- I

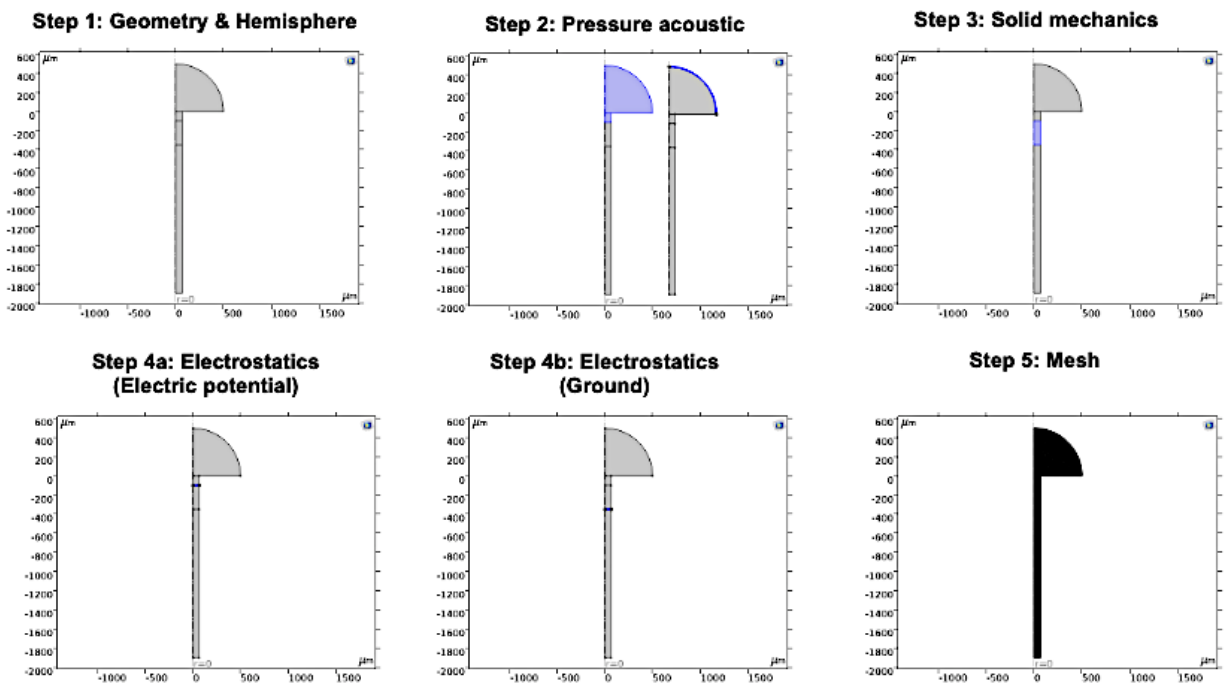

Figure: Illustration showing a step by step guide outlining the sequential procedure for constructing the Finite Element Method (FEM) model within the COMSOL 6.0 software platform.